

**Reconstruction of surface morphology from  
coherent scattering of “white” synchrotron radiation  
in hard x-ray regime**

**Dissertation**

zur Erlangung des Grades eines Doktors  
der Naturwissenschaften

vorgelegt von

M.Sc.

**Tushar Sant**

geb. am 30.05.1976 in Pune (India)

eingereicht beim Fachbereich-7, Physik  
der Universität Siegen

**Siegen, 2009**



## Abstract

The present third generation synchrotron sources provide intense x-ray radiation in hard x-ray regime. The sufficient coherent flux provided by these sources makes it possible to perform coherent x-ray scattering experiments. In 90's several attempts have been made in performing speckle experiments with x-ray radiation at various surfaces which can provide sub-nm spatial resolution. However, the method is not well established as a routine characterization technique. Several details of the experimental technique and data analysis are not solved.

The speckle experiments performed earlier used monochromatic coherent x-ray radiation. It has been shown that the results of such kind of measurements sensitively depend on various parameters of the experiment. Energy Dispersive Reflectometry (EDR) beamline at BESSY II provides "white" x-rays in the useful energy range of  $5 < E < 20 \text{ keV}$ . The availability of the measured speckle data at different energies provides redundant information and is expected to be useful in making the reconstruction of surface profile simpler.

In this work I measured the coherent reflectivity data at EDR bending magnet beamline at BESSY II from various surfaces. Technologically smooth wafers of semiconducting materials of Si and GaAs are used as "trivial" samples to determine the so called apparatus function. In addition I measured coherent reflectivity maps from thin film of highly scattering material of Pt with high atom number,  $Z = 78$  and patterned semiconducting surface like a GaAs surface grating which provides a certain periodicity in the measured scattering intensity. Finally I measured the surface speckles from a spatially confined Si wafer under the constraint that the size of the sample is smaller than the footprint of the incoming beam at the sample position.

To reconstruct surface morphology from coherent reflectivity data is a typical inverse problem. Conventional phase retrieval algorithms like Gerchberg-Saxton (GS) algorithm, error reduction (ER) algorithm, hybrid input-output (HIO) algorithm are used in earlier work by other authors. However, these algorithms are suitable for reconstruction from a data measured in the far-field of the sample. Due to the specific experimental conditions at EDR beamline the data is always measured in the near-field of the sample. Also the spatial confinement of the incoming beam by an entrance pinhole produces Fresnel diffraction pattern (illumination function) at the sample position. I modified the conventional GS

algorithm and ER algorithm which takes into account the additional Fresnel propagator term and also the illumination function at the sample position.

I tested the modified algorithm successfully for a model surface in the form of a surface grating. I used the modified algorithm to reconstruct surface morphology from various static speckle measurements I performed at EDR beamline. The surface profiles reconstructed for different samples from the data at different energies (below the critical energy for the material at a particular incident angle) show almost the same roughness behavior for surface height with mean roughness of  $\sim 1 \text{ nm}$ . With the static speckle data I measured I could retrieve a one-dimensional picture of the sample surface with spatial resolution of  $\sim 15 \mu\text{m}$ . The reconstruction of the surface profile from the static speckle data at different energies for a spatially confined Si wafer gives a two-dimensional picture of the sample surface, spatially resolved as well as depth resolved. Due to different penetration depth of x-rays at different energies the reconstructed profile corresponds to different depths inside the sample. For higher energies the reconstructed profiles look smoother in contrast to the profiles near the surface where the influence of surface roughness is dominant. Such a two-dimensional information of the sample is accessible only due to the measurement of speckle pattern at different energies simultaneously which is possible only due to the “white” x-rays at EDR bending magnet beamline at BESSY II.

Finally, I am successful in testing the real potential of using a “white” x-ray beam for surface profile reconstruction. I have pointed out the real advantages of this novel technique and its limitations compared to the earlier studies with monochromatic x-rays. The technique mentioned in this work can be useful for rapid investigation of sample surface profile. The study can be also useful in performing time resolved surface experiments with “white” x-ray radiation.

## Abstrakt

Die aktuelle dritte Generation von Synchrotronquellen liefert intensive Röntgenstrahlung im harten Röntgenbereich. Der durch diese Quellen bereitgestellte kohärente Fluss ermöglicht kohärente Röntgenstreuexperimente. In den 90-er Jahre wurden erstmals verschiedene Versuche zu kohärenten Beugungsexperimenten an unterschiedlichen Oberflächen durchgeführt, mit denen man eine Auflösung unterhalb der nm Skala erreichen kann. Allerdings haben sich diese Methoden bis heute nicht als Routine zur Charakterisierung von Oberflächen etablieren können. Die Gründe dafür sind unter Anderem verschiedene ungelöste Probleme dieser experimentellen Techniken und der Datenanalyse.

Die bis jetzt durchgeführten Speckle-Experimente verwenden ausschließlich kohärente monochromatische Röntgenstrahlung. Es hat sich gezeigt, dass die Ergebnisse dieser Art von Messungen sehr empfindlich auf verschiedenen Parameter des Experiments, z.B. Umgebungstemperatur, reagieren. Die Energie-dispersive Reflektometrie (EDR) Beamline bei BESSY II nutzt hingegen "weiße" Röntgenstrahlung in einem zugänglichen Energiebereich von  $5 < E < 20$  keV. Die bei verschiedenen Energien zusätzlich gemessenen Speckle-Daten stellen redundante Informationen bereit und man erwartet somit eine Vereinfachung bei der Rekonstruktion der gemessenen Oberflächenprofile.

In dieser Arbeit habe ich kohärente Reflektivitätsdaten verschiedener Oberflächen an der EDR Dipolmagnet Beamline bei BESSY II gemessen. Technologisch glatte Substrate der Halbleitermaterialien Si und GaAs wurden als "triviale" Proben verwendet, um die sogenannte Gerätfunktion zu bestimmen. Zusätzlich dazu habe ich kohärente Reflektivitäts-Karten von dünnen Schichten des stark streuenden Materials Pt ( $Z = 78$ ) und von strukturierten Halbleiteroberflächen wie zum Beispiel GaAs-Oberflächengitter, die eine bekannte Periodizität in der gestreuten Strahlung hervorrufen, gemessen. Schließlich habe ich die Oberflächenspeckle eines räumlich begrenzten Si-Substrats unter der Bedingung gemessen, dass die Projektion des Strahlquerschnittes auf die Probe größer als die Probe selbst war.

Die Rekonstruktion der Oberflächenmorphologie ist ein typisches Inversionsproblem. Konventionelle Phase-Retrieval-Algorithmen wie der Gerchberg-Saxton (GS)-Algorithmus, der Error-Reduction (ER)-Algorithmus sowie der Hybrid-Input-Output-(HIO)-Algorithmus wurden in früheren Arbeiten von anderen Autoren zur Lösung dieses Problems verwendet. Allerdings eignen sich diese Algorithmen nur für Datensätze, die im Fernfeld der Probe

gemessen wurden. Aufgrund der spezifischen experimentellen Bedingungen der EDR Beamline sind hier alle Daten im Nahfeld der Probe gemessen worden. Des Weiteren ruft die räumliche Begrenzung der eingehenden Strahlung durch eine Lochblende ein Fresnel Beugungsmuster (Beleuchtungsfunktion) auf der Probe hervor. In meiner Arbeit habe ich die konventionelle GS- und ER-Algorithmen so modifiziert, dass der Abstand zwischen Probe und Detektor (durch einen zusätzlichen Fresnelterm in den Gleichungen) und die Beleuchtungsfunktion auf der Probe berücksichtigt werden.

Ich habe diesen veränderten Algorithmus erfolgreich an dem Modell eines Oberflächengitters getestet. Nach diesem erfolgreichen Test habe ich den modifizierten Algorithmus zur Rekonstruktion der Oberflächemorphologien aus verschiedenen statischen Speckle-Messungen an der EDR Beamline verwendet. Die Oberflächenrauigkeiten der aus den Daten für verschiedene Energien (unterhalb der kritischen Energie des entsprechenden Einfallswinkels des Materials) rekonstruierten Oberflächenprofile zeigen fast gleiche Verteilungen mit einer durchschnittlichen Rauigkeit von ca. 1 nm. Mit den von mir gemessenen statischen Speckledaten war ich in der Lage ein eindimensionales Bild der Probenoberfläche mit der räumlichen Auflösung von  $\sim 15 \mu\text{m}$  zu erstellen. Die Rekonstruktion des Oberflächenprofils aus den statischen Speckledaten eines räumlich begrenzten Si Substrats für verschiedenen Energien ergibt ein zweidimensionales Bild der Probenoberfläche, welches orts- und tiefenaufgelöst ist. Aufgrund der unterschiedlichen Eindringtiefe der Röntgenstrahlen für verschiedene Energien entsprechen die rekonstruierten Profile verschiedenen Tiefen in der Probe. Die für höhere Energien rekonstruierten Profile sehen im Gegensatz zu den Profilen in der Nähe der Oberfläche, bei denen die Oberflächenrauigkeit eine dominante Rolle spielt, glatter aus. Eine solche zweidimensionale Information der Probe ist nur durch die gleichzeitige Messung der Specklemuster verschiedene Energien zugänglich, wie sie mit Hilfe der "weißen" Röntgenstrahlung an der EDR Dipolmagnet Beamline bei BESSY II möglich ist. Abschließend kann gesagt werden, dass ich das tatsächliche Potenzial der Verwendung von "weißer" Röntgenstrahlung für die Oberflächenrekonstruktion erfolgreich getestet habe. Ich habe in meiner Arbeit die wirklichen Vorteile und Grenzen dieser neuen Technik im Vergleich zu den früheren Untersuchungen mit monochromatischer Röntgenstrahlung gezeigt. Die in dieser Arbeit vorgestellte Technik hat das Potential um erfolgreich für schnelle Rekonstruktionen von Oberflächenprofilen und für zeitaufgelöste Oberflächenuntersuchung mit „weißer“ Röntgenstrahlung eingesetzt zu werden.

# Table of Contents

<b>Abstract</b> .....	<b>iii</b>
<b>Abstrakt</b> .....	<b>v</b>
<b>Chapter 1: Introduction</b> .....	<b>1</b>
1.1 References.....	3
<b>Chapter 2: Theoretical background</b> .....	<b>5</b>
2.1 Interaction of x-rays with matter.....	5
2.1.1 Refractive index.....	6
2.2 X-ray coherence .....	10
2.2.1 Transverse coherence length .....	10
2.2.1 Longitudinal coherence length .....	11
2.3 The interference of partially coherent waves, mutual coherence function and complex degree of coherence.....	13
2.4 Coherent scattering versus incoherent scattering.....	16
2.4.1 Static speckles .....	17
2.5 Phase retrieval.....	19
2.4 References.....	26
<b>Chapter 3: Experimental details</b> .....	<b>27</b>
3.1 Energy dispersive reflectometry (EDR) beamline.....	27
3.1.1 Energy dispersive detector .....	30
3.1.2 Bending magnet emission at EDR.....	31
3.2 Experimental scans .....	33
3.3 Diffraction from entrance pinhole .....	36
3.3.1 Lommel formalism for Fresnel diffraction through circular aperture.....	38
3.4 Demonstration of energy dispersive techniques: EDSAXS.....	41
3.4 References.....	44

<b>Chapter 4: Static speckle measurements from various test surfaces .....</b>	<b>45</b>
4.1 Typical measurement .....	45
4.2 Flat surface as a reflecting mirror .....	48
4.3 Lateral periodic surface.....	51
4.4 Pt thin layer on glass .....	54
4.5 Spatially confined Si wafer .....	56
4.6 Spatially confined GaAs grating.....	58
4.7 References.....	61
<b>Chapter 5: Surface profile reconstruction from coherent x-ray reflectivity .....</b>	<b>62</b>
5.1 Reflected image of illumination function from a flat surface.....	63
5.2 Single surface with random steps of different widths and different heights.....	64
5.3 Scattering amplitude in the near field based on Fresnel electron density.....	68
5.3.1 Formalism based on Fresnel electron density .....	69
5.3.2 Calculations based on Fresnel electron density formalism .....	73
5.4 Reconstruction of object electron density using phase retrieval.....	78
5.4.1 Reconstruction from near field diffraction .....	79
5.4.2 Reconstruction from near field diffraction in reflection geometry .....	86
5.5 Reconstruction of surface height profile from near field diffraction.....	91
5.6 References.....	98
<b>Chapter 6: Surface profile reconstruction from the measured speckle data .....</b>	<b>100</b>
6.1 Reconstruction of surface profile from selected measurements .....	100
6.1.1 GaAs plain wafer at $\alpha_i = 0.2^\circ$ .....	101
6.1.2 GaAs grating at $\alpha_i = 0.1^\circ$ .....	106
6.1.3 GaAs grating at $\alpha_i = 0.25^\circ$ .....	111
6.1.4 Triangular shaped Si wafer with sample width 0.8 mm .....	116
6.1.5 Triangular shaped Si wafer with sample width 2.3 mm.....	121
6.1.6 Triangular shaped Si wafer with sample width > footprint.....	125
6.1.7 Spatially confined GaAs wafer with sample width 1.6 mm .....	130
6.2 References .....	135



<b>Chapter 7: Summary and outlook</b> .....	<b>136</b>
7.1 Summary.....	136
7.2 Outlook.....	138
7.3 References.....	139
<b>Appendix A: Expansion of the diffracted amplitude for reflection geometry</b> .....	<b>141</b>
<b>Acknowledgements</b> .....	<b>145</b>
<b>Eidesstattliche erklärung</b> .....	<b>147</b>



# Chapter 1

## Introduction

The present third generation synchrotron sources and the next generation sources like X-ray free-electron lasers (XFEL) [1.1-1.3] provide intense x-ray radiation in hard x-ray regime with high degree of transverse coherence [1.4]. This facilitates in performing novel experiments like coherent x-ray diffraction imaging (CXDI) and x-ray photon correlation spectroscopy (XPCS).

CXDI is widely studied after the first successful demonstration by Miao *et al.* [1.5]. It has been successfully applied to reconstruct 3D structure of nanostructures [1.6-1.8] and more recently in imaging of protein single crystals [1.9]. Coherent x-rays are also used to study the dynamics of physical processes of liquid or at soft matter surfaces [1.14-1.15], for example, surface relief grating formation on polymer surfaces [1.16-1.18].

The possibility of investigating detailed surface morphology at sub-nanometer resolution is been tested through various experiments using intense coherent x-rays at synchrotron sources [1.10-1.13]. However, the experimental method is not well established and cannot be used for routine investigation of surface morphology.

The coherent reflectivity experiments performed earlier [1.10-1.13] use monochromatic x-ray radiation at synchrotron. Energy Dispersive Reflectometry (EDR) beamline at BESSY II provides intense “white” x-rays in the useful energy range between  $5 < E < 20$  keV with sufficient degree of transverse coherence. The main advantage of using “white” x-ray beam is the scattering can be measured over a wide  $q$  range simultaneously. The surface speckle experiments performed using such polychromatic x-rays can provide redundant data at various energies. The reconstruction of surface morphology is expected to become easier with such abundant x-ray speckles data.

The aim of this work is to test the potential of the approach of combining the unique advantages of using coherent x-ray radiation along with the advantages of using “white” x-ray radiation at BESSY II. The scope of the work consists of finding not only the advantages of

this approach but also the limitations compared to the previously performed surface speckle experiments with monochromatic x-ray radiation [1.10-1.13]. The work is dedicated to the study of static speckle data using “white” x-rays from various patterned and non-patterned surfaces.

The thesis is arranged in the following way.

Chapter 2 begins with some basic theoretical background of x-ray scattering. Coherence properties of x-rays and static speckles are discussed further. Commonly used phase retrieval algorithms and their features are discussed at the end of the chapter.

Unique features of the experimental set up conditions at EDR beamline at BESSY II are discussed in Chapter 3. The profile of the incoming x-ray beam incident at the sample position after spatial confinement at the entrance pinhole is discussed. Energy dispersive x-ray scattering is demonstrated through an experiment of Energy Dispersive Small Angle X-ray Scattering (EDSAXS).

The coherent reflectivity measurements from various semiconducting and metallic surfaces are presented in Chapter 4. The sample surfaces are patterned as well as non-patterned. Experiments performed on spatially confined samples are also discussed.

In Chapter 5 there is a discussion on the calculations for explaining the observed surface speckle amplitude using different approaches used so far and discussion on the reconstruction of surface morphology. Commonly used phase retrieval algorithm is modified to include the illumination function on the sample and the quadratic propagator phase term. The improved phase retrieval algorithm is further successfully tested on a model surface.

Chapter 6 discusses the details of surface profiles reconstruction with the help of the modified algorithm from various surface speckle measurements. The statistical behavior of the reconstruction of surface profile using speckle data measured at various energies is discussed. Two dimensional picture of the sample, depth resolved and laterally resolved, from the reconstruction of the speckle data at various energies is presented for a spatially confined semiconducting sample.

## 1.1 References

- [1.1] J. Arthur *et al.*, *LCLS Conceptual Design Report*, LCLS, USA (<http://www-ssrl.slac.stanford.edu/lcls/cdr/>) (2002)
- [1.2] T. Tanaka & T. Shintake, *SCSS X-FEL Conceptual Design Report*, RIKEN Harima Institute/SPring-8, Japan, (<http://www-xfel.spring8.or.jp/SCSSCDR.pdf>) (2005)
- [1.3] Altarelli, M. *et al.*, *Report DESY 2006–097*, DESY, Hamburg, Germany, ([http://xfel.desy.de/tdr/index\\_eng.html](http://xfel.desy.de/tdr/index_eng.html)) (2006)
- [1.4] Shen Q. *et al.*, *Diffraction imaging of nonperiodic materials with future coherent x-ray sources*, *J. Sync. Rad.* 11, 432-438, (2004)
- [1.5] Miao, J. *et al.*, *Extending the methodology of X-ray crystallography to allow imaging of micrometre-sized non-crystalline specimens*, *Nature (London)*, 400, 342–344, (1999)
- [1.6] M. A. Pfeifer *et al.*, *Three-dimensional mapping of a deformation field inside a nanocrystal*, *Nature*, 442, 63- 66, (2006)
- [1.7] G. J. Williams *et al.*, *Internal structure in small Au crystals resolved by three-dimensional inversion of coherent x-ray diffraction*, *PRB*, 73, 094112-1-8, (2006)
- [1.8] Miao J. *et al.*, *Quantitative image reconstruction of GaN quantum dots from oversampled diffraction intensities alone*, *PRL*, 95, 085503-1-4, (2005)
- [1.9] Boutet S. & I. K. Robinson, *Coherent x-ray diffractive imaging of protein crystals*, *J. Synch. Rad.*, 15, 576-583, (2008)
- [1.10] J. L. Libbert *et al.*, *Speckle in coherent x-ray reflectivity from Si(111) wafers*, *PRB*, 56, 6454-6457, (1997)

- [1.11] I.A. Vatanyants *et al.*, *Reconstruction of surface morphology from coherent x-ray reflectivity*, PRB, 55, 13193-13202, (1997)
- [1.12] I. K. Robinson *et al.*, *Coherent x-ray diffraction imaging of silicon oxide growth*, PRB, 60, 9965-9972, (1999)
- [1.13] F. Pfeiffer *et al.*, *Coherent grazing exit x-ray scattering geometry for probing the structure of thin films*, APL, 84, 1847-1849, (2004)
- [1.14] C. Gutt *et al.*, *Partially Wetting Thin Liquid Films: Structure and Dynamics Studied with Coherent X Rays*, PRL, 99, 096104-1-4, (2007)
- [1.15] Z. Jiang *et al.*, *Evidence for Viscoelastic Effects in Surface Capillary Waves of Molten Polymer Films*, PRL, 98, 227801 (2007)
- [1.16] O. Henneberg *et al.*, *Simultaneous X-ray and visible light diffraction for the investigation of surface relief and density grating formation in azobenzene containing polymer films*, Molecular Crystals and Liquid Crystals, 446, 111-121, (2006)
- [1.17] O. Henneberg *et al.*, *X-ray and VIS light scattering from light-induced polymer gratings*, J. Phys. D: Appl. Phys., 36, A241-A244, (2003)
- [1.18] U. Pietsch, *X-ray and visible light scattering from light-induced polymer gratings*, PRB, 66, 155430-1-9, (2002)
- [1.19] U. Pietsch *et al.*, *The energy-dispersive reflectometer at BESSY II: a challenge for thin film analysis*, Nuclear Instruments and Methods in Physics Research A, 467-468, 1077-1080, (2001)
- [1.20] Y. Bodenthin *et al.*, *Temperature- and time-resolved X-ray scattering at thin organic films*, J. Synch. Rad., 9, 206-209, (2002)

## Chapter 2

### Theoretical Background

This chapter describes some basic properties of interaction of x-rays with matter. It starts with the discussion on the refractive index of the materials for x-rays. Various peculiar phenomena occur when x-rays strike the interface between air and matter due to the refractive index for x-rays being smaller than unity. These phenomena are discussed in detail further in the chapter. By tuning the energy and incident angle x-rays can be made sensitive only to the surface of the sample. This surface sensitivity property of x-rays is discussed further.

The next section of the chapter discusses the coherence properties of the x-rays. The scattering of coherent x-rays from a disordered medium gives rise to speckle like pattern, in contrast to continuous diffuse scattering in case of incoherent x-rays. This distinctive feature of coherent x-ray scattering is discussed further. The speckle pattern contains the information about the density distribution of the scattering medium. But the recorded speckle intensity pattern loses the information about the phase of the scattered amplitude. The last section of this chapter discusses the conventional phase retrieval algorithms used to reconstruct the density distribution from the recorded speckle intensities.

#### 2.1 Interaction of x-rays with matter

Electric field vector for a plane polarized electromagnetic wave can be written as

$$E(\mathbf{r}, t) = \hat{\epsilon} a_l e^{i(\mathbf{k}_l \cdot \mathbf{r} - \omega t)} \quad (2.1)$$

Where  $\hat{\epsilon}$  is a unit vector,  $a_l$  is the amplitude,  $k = 2\pi/\lambda$  is the modulus of wavevector  $\mathbf{k}_l$ ,  $\lambda$  is the wavelength and  $\omega$  is the frequency of the electromagnetic wave and  $\mathbf{r}$  indicates vector for point with spatial coordinates  $(x, y, z)$ .

Such an electromagnetic wave gets scattered when it is incident on a condensed matter. Elastic scattering of x-rays is the most exploited process in the investigations of structure of materials. In case of elastic scattering the wavelength of the scattered wave is the same as that of the incident wave.

Even though a process is elastic, momentum can be transferred as

$$\hbar\mathbf{q} = \hbar\mathbf{k}_f - \hbar\mathbf{k}_i \quad (2.2)$$

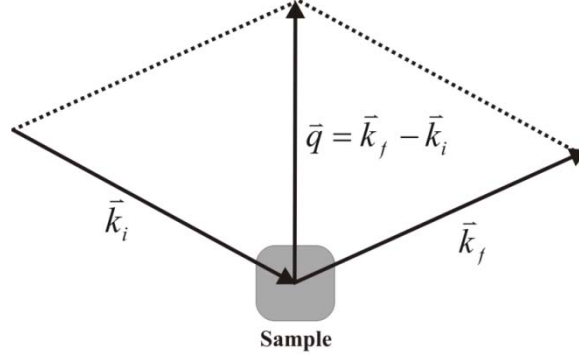


Figure 2.1 Basic scattering geometry with initial and final wave vectors

where  $\hbar\mathbf{k}_f$  and  $\hbar\mathbf{k}_i$  are the initial and final momenta of the photon respectively. The vector  $\mathbf{q} = \mathbf{k}_f - \mathbf{k}_i$  is known as the *wave vector transfer* or *scattering vector* as shown in Fig. 2.1 and it is a natural variable to describe elastic scattering process. The scattering vector has dimension of inverse of length i.e.  $L^{-1}$ .

### 2.1.1 Refractive Index

An x-ray wave represented by electric field vector as in equation (2.1) undergoes refraction inside a medium with refractive index  $n(\mathbf{r})$ . Its propagation is given by the Helmholtz equation

$$\Delta\mathbf{E}(\mathbf{r}) + k^2n^2\mathbf{E}(\mathbf{r}) = 0 \quad (2.3)$$

The medium is considered to be arrangement of  $N$  atoms per unit volume, which are harmonic oscillators with resonance frequencies  $\omega_j$ .

The index of refraction is given by [2.1]

$$n^2(\mathbf{r}) = 1 + N \frac{e^2}{\epsilon_0 m} \sum_{j=1}^N \frac{f_j}{\omega_j^2 - \omega^2 - 2i\omega\eta_j} \quad (2.4)$$

Where  $e$  and  $m$  are the charge and mass of electron, respectively,  $\eta_j$  are the damping factors and  $f_j$  are the strengths of forced oscillations of electrons.



In general  $f_j$  are complex and considering the dispersion and absorption corrections  $f_j'(E)$  and  $f_j''(E)$ ,  $f_j$  can be written as

$$f_j = f_j^0 + f_j'(E) + if_j''(E) \quad (2.5)$$

For x-rays  $f_j'(E)$  and the index of refraction can be expressed as

$$n(\mathbf{r}) = 1 - \delta(\mathbf{r}) + i\beta(\mathbf{r}) \quad (2.6)$$

with the dispersion and absorption terms as

$$\delta(\mathbf{r}) = \frac{\lambda^2}{2\pi} r_0 \rho(\mathbf{r}) \sum_{j=1}^N \frac{f_j^0 + f_j'(E)}{Z} \quad (2.7)$$

$$\beta(\mathbf{r}) = \frac{\lambda^2}{2\pi} r_0 \rho(\mathbf{r}) \sum_{j=1}^N \frac{f_j''(E)}{Z} = \frac{\lambda}{4\pi} \mu(\mathbf{r}) \quad (2.8)$$

Here  $r_0$  is the classical electron radius,  $r_0 = e^2/4\pi\epsilon_0 mc^2 = 2.814 \times 10^{-5} \text{ \AA}$  with  $c$  as speed of light in vacuum,  $\rho(\mathbf{r})$  is the density of electrons,  $Z = \sum_j Z_j$  is total number of electrons,  $Z_j$  denotes the number of electrons for each material and  $\mu$  is the linear absorption coefficient. In the region of glancing incidence and exit angles the wave vector transfer is small and  $f_j^0$  may be approximated by  $f_j^0 \approx Z_j$ .

For a homogeneous medium and far away from absorption edges the dispersion term can be written as

$$\delta = \frac{\lambda^2}{2\pi} r_0 \rho \left( 1 + \frac{f'}{Z} \right) \quad (2.9)$$

The typical value of  $\delta$  for materials is around  $10^{-6}$  and the value for  $\beta$  is still one or two orders of magnitude smaller. Due to this fact the refractive index of materials for x-rays is slightly smaller than unity. X-ray incident from air on an interface of air-material undergoes a phenomenon of total external reflection below certain angle of incidence. This is explained in more details below.

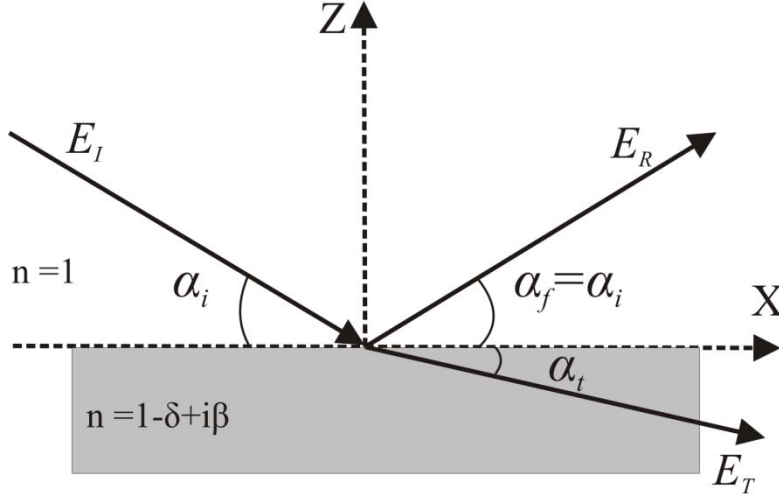


Figure 2.2 A plane electromagnetic wave getting partly reflected and partly transmitted

Consider a plane electromagnetic wave  $E_I(\mathbf{r}) = a_I e^{i\mathbf{k}_I \cdot \mathbf{r}}$  incident on a single vacuum-material interface at grazing incident angle of  $\alpha_i$ , as in Fig. 2.2. The reflected and transmitted waves are  $E_R(\mathbf{r}) = a_R e^{i\mathbf{k}_R \cdot \mathbf{r}}$  and  $E_T(\mathbf{r}) = a_T e^{i\mathbf{k}_T \cdot \mathbf{r}}$  respectively. At grazing angles by Snell's law of refraction

$$\cos \alpha_i = n \cos \alpha_f \quad (2.10)$$

Neglecting the absorption term  $\beta$ , this becomes

$$\cos \alpha_i = (1 - \delta) \cos \alpha_f \quad (2.11)$$

This implies that below a certain incident grazing angle called as critical angle  $\alpha_c$ , x-rays undergo total external reflection in air.

Thus for  $\alpha_i = \alpha_c$ ,  $\alpha_f = 0$  and after expansion of cosine term in equation (2.11) the critical angle  $\alpha_c$  is

$$\alpha_c \approx \sqrt{2\delta} \quad (2.12)$$

In case of diffraction and reflection phenomena, the wave vector transfer  $q$  is more useful quantity than angle.

$$q = |\mathbf{k}_R - \mathbf{k}_I| = 2k \sin \alpha_i \quad (2.13)$$

For small angles  $q \cong 2k\alpha_i$ . The wave vector transfer at critical angle is given by

$$q_c \equiv 2k\alpha_c = 2k\sqrt{2\delta} = 4\sqrt{\pi\rho r_0\left(1 + \frac{f'}{Z}\right)} \quad (2.14)$$

It can be seen that the wave vector  $q_c$  at critical angle is independent of wavelength of radiation and thus it is a very useful quantity.

The reflection coefficient  $r = a_R/a_I$  and transmission coefficient  $r = a_T/a_I$  can be determined from the well known Fresnel formulas. The intensity reflectivity  $R_F = |r|^2 = |a_T/a_I|^2$  of reflected x-ray in grazing incidence regime is given by [2.2]

$$R_F = \frac{(\alpha_i - p_+)^2 + p_-^2}{(\alpha_i + p_+)^2 + p_-^2} \quad (2.15)$$

where for small angles the real and imaginary part of the transmission angle  $\alpha_i = p_+ + ip_-$  can be approximated by,

$$p_{+,-}^2 \approx \frac{1}{2} \left\{ \sqrt{(\alpha_i^2 - \alpha_c^2)^2 + 4\beta^2} \pm (\alpha_i^2 - \alpha_c^2) \right\} \quad (2.16)$$

For complex transmission angle  $\alpha_i = p_+ + ip_-$  the modulus of electric field in the medium ( $z \leq 0$ ) can be written as

$$E_T = |a_T| e^{i(k_{i,x}x - k_z p_+)} e^{k_z p_-} \quad (2.17)$$

Thus below critical angle ( $\alpha_i \leq \alpha_c$ ),  $p_-$  is large and the transmitted wave propagates parallel to the interface. It is called as *evanescent wave* and its amplitude decays exponentially in the material. The intensity of transmitted falls off to 1/e at the *penetration depth* given by

$$\Lambda = \frac{1}{kp_-} = \frac{\lambda}{\sqrt{2\pi}} \left\{ \sqrt{(\alpha_i^2 - \alpha_c^2)^2 + 4\beta^2} - (\alpha_i^2 - \alpha_c^2) \right\}^{-1/2} \quad (2.18)$$

For grazing incidence angle i.e.  $\alpha_i \rightarrow 0$ , the penetration depth becomes  $\Lambda_0 = \frac{\lambda}{2\pi\alpha_c} = \frac{1}{\sqrt{4\pi r_0 \rho}}$  and is independent of wavelength  $\lambda$ .

For most of the materials the penetration depth of x-rays is around few nanometers. Thus by keeping shallow angle of incidence the x-rays can be made sensitive only to the surface or the

subsurface region of the sample. Keeping this in mind, only the sample surface is probed by keeping small incident angles in the special surface sensitive techniques such as GID (Grazing Incidence Diffraction) and GISAXS (Grazing Incidence Small Angle X-ray Scattering).

## 2.2 X-ray Coherence

The amplitudes and phases of light waves emitted from an extended source fluctuate in different parts of a beam. If the fluctuations are correlated the beam is said to be completely or partially coherent, depending on whether the correlation is complete or partial. Without such a correlation, the beam is said to be incoherent. In the visible range of electromagnetic spectrum lasers provide radiation with good degree of coherence. With the advent of high brilliant third generation synchrotron sources and free electron lasers coherent radiation is available also in x-ray regime. The coherence properties of a beam are described by two types of coherence, transverse (spatial) and longitudinal (temporal) and can be quantified in terms of transverse and longitudinal coherence length.

### 2.2.1 Transverse Coherence Length

Transverse coherence is a measure of the correlation in the phase across the wavefront in the direction perpendicular to the direction of propagation of beam. A Young's double slit experiment yields fringes only when the separation between the slits does not greatly exceed the transverse coherence length of the beam.

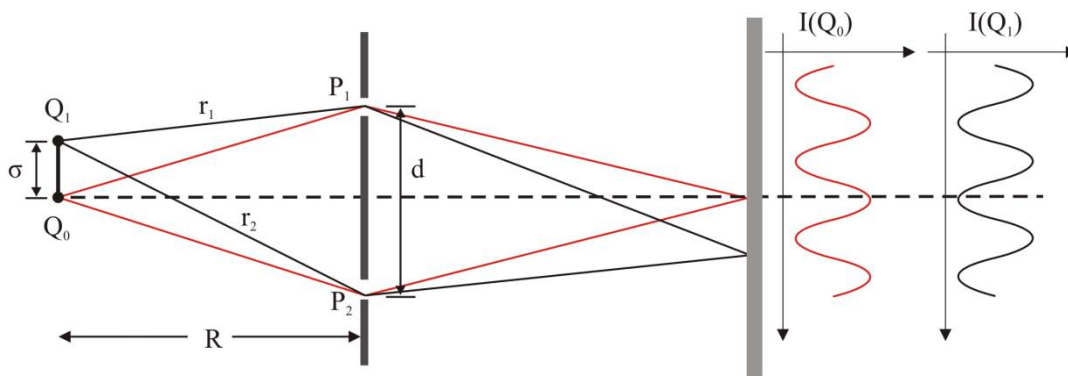


Figure 2.3 Young's double slit experiment

Let us consider a schematic set up as in Fig. 2.3 with an extended source of light with width  $\sigma$ . Light rays pass through two slits separated by distance  $d$  and at a distance  $L$  away from the source. A light ray emanating from any point on the extended source travels different path

lengths  $r_1$  and  $r_2$  to reach the slits  $P_1$  and  $P_2$ . The difference between the path lengths  $r_1$  and  $r_2$  is given by [2.3]

$$r_2 - r_1 = \sqrt{\left(\frac{d}{2} + \sigma\right)^2 + L^2} - \sqrt{\left(\frac{d}{2} - \sigma\right)^2 + L^2} \quad (2.19)$$

The condition for interference fringes to be visible is that the maximum of fringe pattern due to  $Q_1$  must not coincide with the minimum due to  $Q_2$ . This needs that the difference in path lengths,  $r_2 - r_1$ , be less than half the wavelength, i.e.

$$r_2 - r_1 < \frac{\lambda}{2} \quad (2.20)$$

Expanding and simplifying the terms in the square root in equation (2.19) and using it in equation (2.20)

$$r_2 - r_1 = \frac{d\sigma}{L} < \frac{\lambda}{2} \quad (2.21)$$

$$d < \frac{\lambda L}{2\sigma} = \xi_x \quad (2.22)$$

Thus the spatial coherence length depends on the source via its wavelength and spatial extension and on the geometrical arrangement via source-aperture distance  $L$ .

Third generation synchrotron radiation sources typically have a source size of  $\sigma_v = 10\text{-}50 \mu\text{m}$  and  $\sigma_h = 100\text{-}500 \mu\text{m}$ . At a wavelength of  $0.1 \text{ nm}$  and at a typical distance of  $40 \text{ m}$  from the source, the transverse coherence lengths are in the range  $\xi_v = 25\text{-}100 \mu\text{m}$  and  $\xi_h = 3\text{-}10 \mu\text{m}$  [2.2]. The object may have dimensions larger than the coherence length. In that case coherent part of the beam is selected by spatially filtering it with a pair of slits or pinhole of size less than transverse coherence length. Spatial filtering to produce coherent beam reduces the photon flux after filtering. The availability of high-brilliance synchrotron sources still provides sufficient flux after spatial filtering to perform coherent experiments with x-ray radiation.

### 2.2.2 Longitudinal Coherence Length

Longitudinal coherence is a measure of the ability of the beam to interfere along its direction of propagation. Let us consider two wavefronts emitted from the same point  $P$ , one at wavelength  $\lambda$  and other at a slightly different wavelength  $\lambda + \Delta\lambda$ . The two wavefronts are

exactly in phase at point P. As the distance from point P increases the phase difference increases. The two wavefronts become out of phase for the first time after certain distance  $\xi_l$ . This distance is the longitudinal coherence length  $\xi_l$  for the beam. Here the maximum for  $\lambda$  coincides with the minimum for  $\lambda + \Delta\lambda$ . If the first wave has made  $N$  oscillations to produce maximum over this distance, the second wave must have made  $N - \frac{1}{2}$  oscillations to produce minimum.

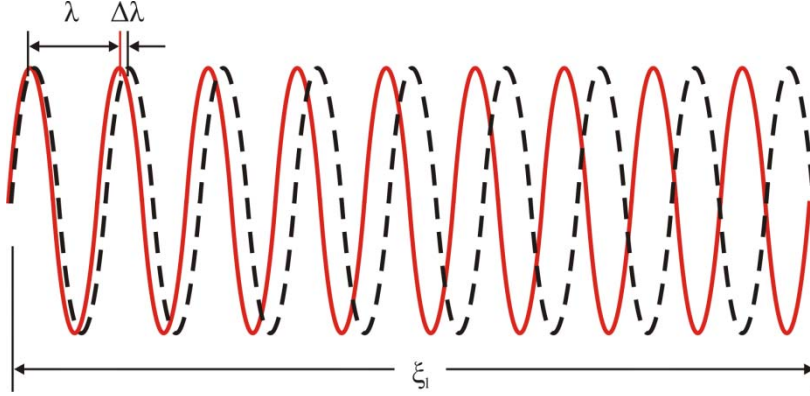


Figure 2.4 Propagation of two waves with wavelengths  $\lambda$  and  $\lambda + \Delta\lambda$

This means

$$\xi_l = N\lambda = \left(N - \frac{1}{2}\right)(\lambda + \Delta\lambda) \quad (2.23)$$

From the second equation

$$N\lambda = N\lambda - \frac{1}{2}\lambda + \left(N - \frac{1}{2}\right)\Delta\lambda$$

$$\left(N - \frac{1}{2}\right)\Delta\lambda = \frac{1}{2}\lambda$$

$$N\Delta\lambda \cong \frac{1}{2}\lambda$$

$$N \cong \frac{1}{2} \frac{\lambda}{\Delta\lambda} \quad (2.24)$$

Using this result the expression for longitudinal coherence length becomes

$$\xi_l = \frac{1}{2} \frac{\lambda^2}{\Delta\lambda} \quad (2.25)$$

The longitudinal coherence length is inversely proportional to the bandwidth  $\Delta\lambda$ . It is a measure of monochromaticity of x-ray beam. Energy resolution  $\Delta E/E$  for typical monochromators is around  $10^{-4}$ . For x-rays of wavelength 0.1 nm the longitudinal coherence length  $\zeta_l$  is about 0.5  $\mu\text{m}$ . This is much smaller than the transverse coherence length.

In case of energy dispersive set up at EDR beamline at BESSY II, the x-ray beam is not monochromatized. The x-rays emitted at the bending magnet are directly used for the scattering experiments. In this case, the x-rays with different wavelength or different energies do not interfere with each other and the term wavelength spread  $\Delta\lambda$  or energy spread  $\Delta E$  is no more valid. Thus the above mentioned definition for longitudinal coherence length in equation (2.25) is also not valid.

### **2.3 The interference of partially coherent waves, mutual coherence function and complex degree of coherence**

For the satisfactory explanation of physical event involving light coming from finite source, it is important to consider the correlation between the vibrations at two arbitrary points in the wave field [2.6].

Let us consider again the schematic set up as in Fig. 2.3. A wave field is produced by an extended polychromatic source of light of size  $\sigma$ . If the distance between the pinholes  $P_1$  and  $P_2$  is small as compared to the transverse coherence length, an interference pattern with high contrast is visible. As this separation increases the contrast in the interference pattern reduces due to the large transverse coherence length. The incoherent sum of the intensities from  $P_1$  and  $P_2$  is observed on the screen. According to Huygen's principle  $P_1$  and  $P_2$  become secondary sources of spherical waves of light. The complex amplitude at point Q on screen at time t is the sum of the contribution from each source

$$A(Q, t) = m_1 A(P_1, t - t_1) + m_2 A(P_2, t - t_2) \quad (2.26)$$

The constants  $m_1$  and  $m_2$  depend on the distances  $r_1$  and  $r_2$ , size of pinholes and the angles of incidence and diffraction at  $P_1$  and  $P_2$ . Since the secondary wavelets from  $P_1$  and  $P_2$  are out of phase with the primary wave by quarter of a period,  $m_1$  and  $m_2$  are purely imaginary.

$t_1, t_2$  are the times need for light to travel from  $P_1$  to  $Q$  and from  $P_2$  to  $Q$  respectively

$$t_1 = \frac{r_1}{c}, t_2 = \frac{r_2}{c} \quad (2.27)$$

where  $c$  is the speed of light in vacuum.

The time averaged intensity at point  $Q$  is given by

$$I(Q) = \langle A(Q, t)A^*(Q, t) \rangle \quad (2.28)$$

$$I(Q) = m_1 m_1^* \langle A_1(t - t_1)A_1^*(t - t_1) \rangle + m_2 m_2^* \langle A_2(t - t_2)A_2^*(t - t_2) \rangle \\ + m_1 m_2^* \langle A_1(t - t_1)A_2^*(t - t_2) \rangle + m_2 m_1^* \langle A_2(t - t_2)A_1^*(t - t_1) \rangle \quad (2.29)$$

where  $A_1(t)$  and  $A_2(t)$  are short notations for  $A_1(Q, t)$  and  $A_2(Q, t)$  respectively and the angle brackets indicate averaging over time. Let  $I_1 = \langle A_1(t)A_1^*(t) \rangle$  and  $I_2 = \langle A_2(t)A_2^*(t) \rangle$  denote intensity at pinholes  $P_1$  and  $P_2$  respectively. The mutual coherence function is defined as

$$\Gamma_{12}(\tau) = \langle A_1(t + \tau)A_2^*(t) \rangle \quad (2.30)$$

which is a combination of spatial and temporal coherence functions.

The expression for the intensity at  $Q$  is simplified as

$$I(Q) = |m_1|^2 I_1 + |m_2|^2 I_2 + 2|m_1 m_2| \Gamma_{12}^{(r)}(\tau) \quad (2.31)$$

Here  $\tau = t_2 - t_1$  and  $\Gamma_{12}^{(r)}$  indicates the real part of  $\Gamma_{12}$ . Self-coherence occurs when the two points coincide ( $P_1 = P_2$ ) with each other and we get

$$\Gamma_{11}(\tau) = \langle A_1(t + \tau)A_1^*(t) \rangle \quad (2.32)$$

It reduces to ordinary intensity when  $\tau=0$

$$\Gamma_{11}(0) = I_1, \Gamma_{22}(0) = I_2$$

The term  $|m_1|^2 I_1$  is the intensity at  $Q$  due to pinhole  $P_1$  only and  $|m_2|^2 I_2$  is the intensity due to pinhole  $P_2$  only. Let us denote them as  $I^{(1)}(Q)$  and  $I^{(2)}(Q)$  respectively. The normalized form of  $\Gamma_{12}$  can be written as

$$\gamma_{12}(\tau) = \frac{\Gamma_{12}(\tau)}{\sqrt{\Gamma_{11}(0)}\sqrt{\Gamma_{22}(0)}} = \frac{\Gamma_{12}(\tau)}{\sqrt{I_1}\sqrt{I_2}} \quad (2.33)$$



$\gamma_{12}(\tau)$  is called as complex degree of coherence. In terms of this the intensity at Q can be written as

$$I(Q) = I^{(1)}(Q) + I^{(2)}(Q) + 2\sqrt{I^{(1)}(Q)}\sqrt{I^{(2)}(Q)}\gamma_{12}^{(r)}(\tau) \quad (2.34)$$

where  $\gamma_{12}^{(r)}$  denotes the real part of  $\gamma_{12}(\tau)$ .

This expression is known as the general law of interference. It shows that the intensity due to the superposition of two wave fields depends on the intensity of each beam and the value of the real part  $\gamma_{12}^{(r)}$  of the complex coherence function.

The value of  $|\gamma_{12}(\tau)|$  decides the degree of coherence. The extreme value of unity for  $|\gamma_{12}(\tau)|$  indicates the full coherence between the two wave fields. The other extreme value of zero for  $|\gamma_{12}(\tau)|$  indicates complete lack of coherence, i.e. incoherent, and the beams do not give rise to any sort of interference effect. For the value of  $|\gamma_{12}(\tau)|$  between two extremes, i.e.  $0 < |\gamma_{12}(\tau)| < 1$ , the wave fields are partially coherent.

The intensity at point Q can further be written as

$$I(Q) = I^{(1)}(Q) + I^{(2)}(Q) + 2\sqrt{I^{(1)}(Q)}\sqrt{I^{(2)}(Q)}|\gamma_{12}(\tau)|\cos(\alpha_{12}(\tau) - \delta) \quad (2.35)$$

where

$$\alpha_{12}(\tau) = \delta + \arg \gamma_{12}(\tau) = 2\pi\bar{\omega}\tau + \arg \gamma_{12}(\tau) \quad (2.36)$$

with  $\bar{\omega}$  as the mean frequency of the radiation.

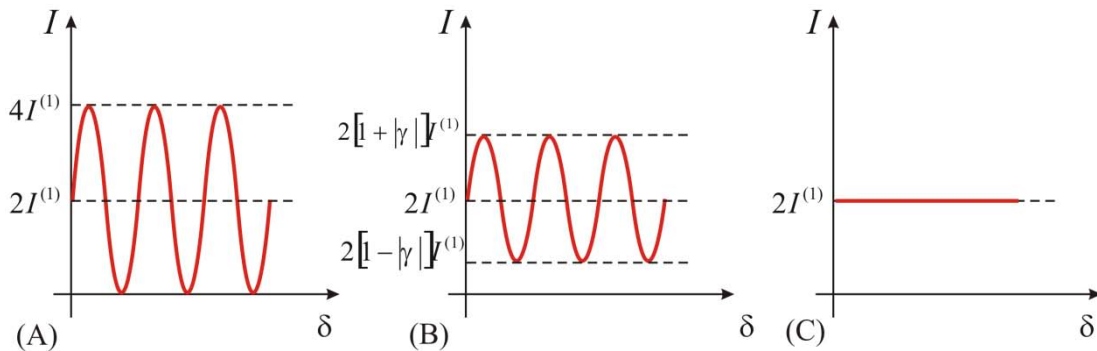


Figure 2.5 Intensity distribution of interference pattern: (A) coherent, (B) partially coherent, (C) incoherent case

The intensity distribution in the vicinity of  $Q$  consists of an almost uniform background  $I^{(1)}(Q) + I^{(2)}(Q)$  on which a sinusoidal intensity distribution is superimposed, with almost constant amplitude  $2\sqrt{I^{(1)}(Q)}\sqrt{I^{(2)}(Q)}|\gamma_{12}(\tau)|$ . The behavior of the total intensity distribution is shown in Fig. 2.5 for three typical cases. It can be observed that the contrast reduces from coherent to the incoherent case. For the complete incoherent case the resultant intensity is constant.

The intensity maxima and minima near  $Q$  to a good approximation is given by

$$I_{max} = I^{(1)}(Q) + I^{(2)}(Q) + 2\sqrt{I^{(1)}(Q)}\sqrt{I^{(2)}(Q)}|\gamma_{12}(\tau)| \quad (2.35)$$

$$I_{min} = I^{(1)}(Q) + I^{(2)}(Q) - 2\sqrt{I^{(1)}(Q)}\sqrt{I^{(2)}(Q)}|\gamma_{12}(\tau)| \quad (2.36)$$

The visibility of fringes at  $Q$  in terms of the intensities of two beams is given by

$$V(Q) = \frac{I_{max} - I_{min}}{I_{max} + I_{min}} = \frac{2\sqrt{I^{(1)}(Q)}\sqrt{I^{(2)}(Q)}}{I^{(1)}(Q) + I^{(2)}(Q)}|\gamma_{12}(\tau)| \quad (2.37)$$

If the intensities of the two beams are equal ( $I^{(1)} = I^{(2)}$ ), visibility is given by

$$V(Q) = |\gamma_{12}(\tau)| \quad (2.38)$$

Thus the visibility of fringes equals to the modulus of the complex degree of coherence.

## 2.4 Coherent Scattering versus Incoherent Scattering

Consider a system described by electron density function  $\rho(\mathbf{r})$  placed in a perfectly monochromatic and collimated x-ray beam. Let us consider that the system is non-ergodic i.e. it has built-in disorder.

According to the kinematical theory, the amplitude of the scattered radiation is given by

$$A(\mathbf{q}) = \int \rho(\mathbf{r})e^{-i\mathbf{q}\cdot\mathbf{r}} d\mathbf{r} \quad (2.39)$$

The intensity of the scattered radiation is given by

$$I(\mathbf{q}) = \iint \langle \rho(\mathbf{r})\rho(\mathbf{r}') \rangle_T e^{-i\mathbf{q}\cdot(\mathbf{r}-\mathbf{r}')} d\mathbf{r} \quad (2.40)$$

Here it is assumed that the measurement is performed over time  $T$ , which is long enough than the average correlation time of the system.

When the system is illuminated by a perfectly coherent x-ray beam, the statistical ensemble averaging cannot be taken. The intensity can be written as

$$I(\mathbf{q}) = |A(\mathbf{q})|^2 = \left| \int \rho(\mathbf{r})e^{-i\mathbf{q}\cdot\mathbf{r}} d\mathbf{r} \right|^2 \quad (2.41)$$

Due to the inherent disorder in the system the intensity pattern contains sharp and random fluctuations about some particular average function. This gives rise to a phenomenon of “speckles” in the diffuse scattering. It is discussed in detail in next section.

In case of the incoherent illumination, the intensity pattern is an ensemble average over all the finite coherence volumes. The expression for the intensity can now be written as

$$I(\mathbf{q}) = |A(\mathbf{q})|^2 = \int |\rho(\mathbf{r})e^{-i\mathbf{q}\cdot\mathbf{r}}|^2 d\mathbf{r} \quad (2.42)$$

Due to the ensemble averaging the speckle pattern smears out and smooth diffuse scattering is observed.

### 2.4.1 Static Speckles

As discussed in the earlier section, when a beam of coherent electromagnetic radiation passes through a region that introduces random phase changes across the wavefront the resulting intensity distribution is granular commonly referred as “speckles”. This can happen either by transmission of the beam through an inhomogeneous medium or its reflection from a rough surface. The speckle pattern contains detailed information about the structure of the scattering region. In principle, it is possible to reconstruct the structure of the object in unique way. In case of incoherent illumination it not possible to reconstruct the structure of the object from the diffracted intensity pattern as the diffuse scattering is smooth and featureless. It can give only average information and is unable to give any detailed spatially resolved information.

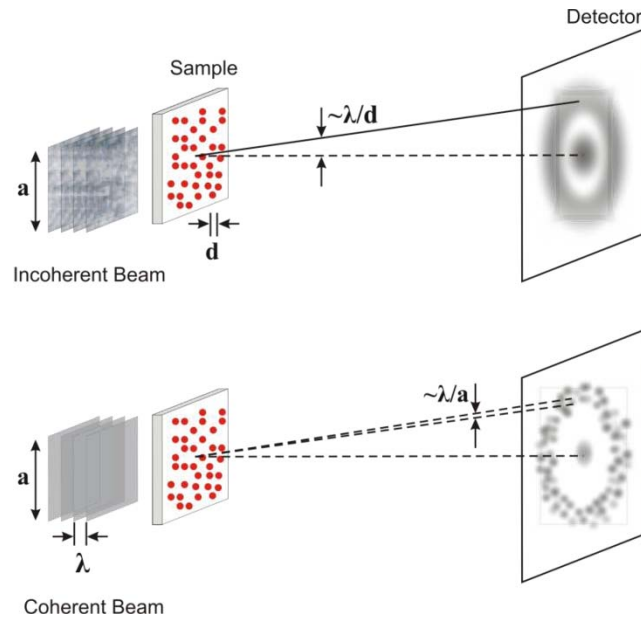


Figure 2.6 X-ray scattering through distorted medium with particle size  $d$  and size of illuminated area  $a$ . Upper figure shows the incoherent and lower figure shows the coherent scattering.

Consider x-ray beam with wavelength  $\lambda$  passes through a disordered medium illuminating the area of size  $a$ , as shown in Fig. 2.6. Let the average particle size be  $d$ . In case of incoherent illumination the maximum intensity is found at an angle of  $\sim \lambda/d$ . Interference effect is not observed and the total intensity is the sum of the individual intensities. If the medium is illuminated with coherent beam instead, the speckle pattern contains features of much smaller size  $\sim \lambda/a$ . The speckles arise from the interference between the wavefronts scattered from the different particles or between the wavefronts which travel different optical path. If the position of a single particle is changed all interferences are affected and the whole speckle pattern changes. The speckle size  $\lambda/a$  is the same for all the speckles and contains no information about the internal structure of the scattering region. The intensity and the distribution of speckles are important in reconstructing the detailed structure of the scattering object [2.4].

In case of reflection from a rough surface, each point of the surface scatters spherical waves whose phase varies statistically according to the differing heights across the rough surface (see Fig. 2.7). X ray reflectivity from ideal surface follows Fresnel law with specular and diffuse reflectivity that falls off with momentum transfer  $q$  as  $1/q^4$ . The reflectivity from a rough surface drops more quickly and show nonspecular part. The nonspecular component exhibits fine structure. This fine structure or a speckle pattern is related to the specific

morphology of the illuminated portion of the surface. It is a result of interference of waves scattered from different parts of the rough surface.

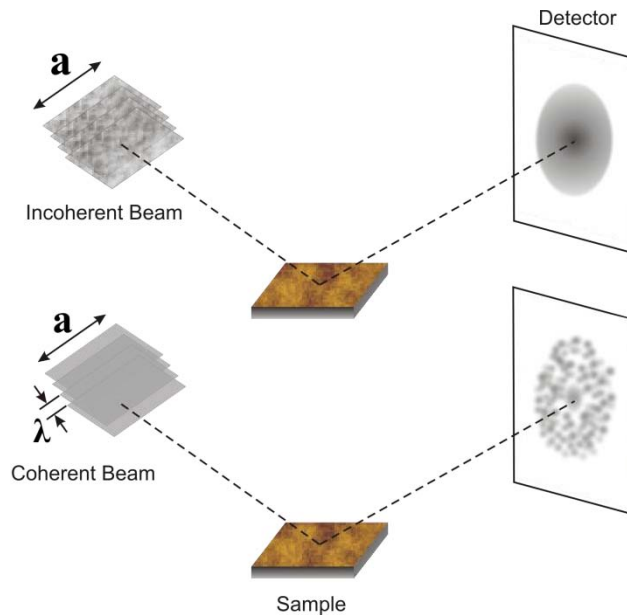


Figure 2.7 Reflection of x-rays from a rough surface with size of illuminated area  $a$ . Upper figure is for incoherent scattering and lower is for coherent scattering.

An incoherent beam reflected from rough surface cannot produce such a pattern. In this case the intensity distribution is a result of the sum of individual intensities of waves scattered from each point on the rough surface. The nonspecular component is diffuse and is related in an average way to the roughness of the surface.

## 2.5 Phase Retrieval

Since its first successful demonstration by Miao et al. [2.5] the phase retrieval techniques are widely used in reconstructing electron density from static speckle data in coherent x-ray diffraction imaging experiments. Following is the discussion of basic algorithm of phase retrieval and subsequent variations of the algorithm developed to improve the quality of the reconstruction.

Amplitude of x-rays scattered from an object with density distribution  $\rho(x, y)$  (see Fig. 2.8) can be written as

$$A(q_x, q_y) = \iint \rho(x, y) e^{-i(q_x x + q_y y)} dx dy \quad (2.43)$$

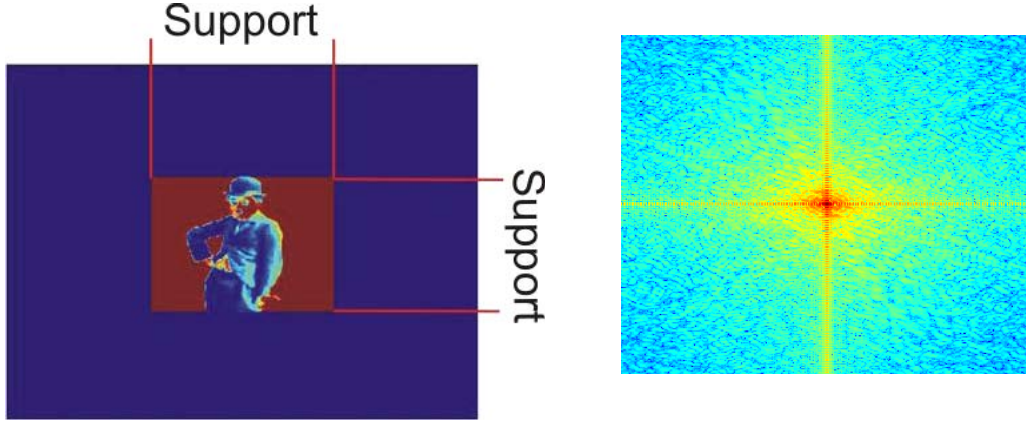


Figure 2.8 (A) Object in the form of support and surrounded by zero density region  
(B) Far field diffraction pattern of the object

$A(q_x, q_y)$  is in general a complex quantity and can be written as  $A(q_x, q_y) = |A(q_x, q_y)| e^{i\Phi}$ , where  $|A(q_x, q_y)|$  is the magnitude and  $\varphi$  is the phase of the scattered Amplitude. The detector used in any experiment can only measure the scattered intensity  $|A(q_x, q_y)|^2$  and not the complex amplitude  $A(q_x, q_y)$ . Hence the phase information is lost in the measurement. It can be easily seen from equation (2.43) that the scattered amplitude can be written as Fourier transform of real space density  $\rho(x, y)$ .

$$A(q_x, q_y) = \mathcal{F}(\rho(x, y)) \quad (2.44)$$

If the complex amplitude  $A(q_x, q_y)$  could be measured, then the real space density  $\rho(x, y)$  can be extracted simply by taking inverse Fourier transform of  $\rho(x, y)$ . But this is not possible because lack of phase information,  $e^{i\Phi}$ .

The density distribution can be reconstructed from the diffraction pattern by applying an iterative phase retrieval algorithm. Various algorithms are developed to retrieve the lost phases during the measurement. All of these iterate back and forth from real to reciprocal space. Constraints are applied in both real and reciprocal space to guide the algorithm to find a solution consistent with observed diffracted data and expected density distribution  $\rho(x, y)$ .

One of the earliest phase retrieval algorithms was presented by Gerchberg and Saxton [2.7]. This algorithm is developed to solve the problem of two intensity measurements, one in real space and the other in reciprocal space. There are two known constraints, one for the modulus of amplitude in diffraction plane and the second for the modulus in the object plane.

Following steps are involved (see Fig. 2.9):

Apply random phases in the interval  $[-\pi, \pi]$  to the modulus of measured amplitude in object plane to get a starting guess

$$\varphi_1 = \text{rand} [-\pi, \pi]$$

$$g_1(x) = |A(x)| \exp(i\varphi_1)$$

- (i) Fourier transform this estimate of the object

$$G_k(q) = |G_k(q)| \exp(i\Phi_k) = \mathcal{F}(g_k(x)) \quad (2.45)$$

- (ii) Replace the modulus of resulting transform with the modulus of measured diffraction amplitude

$$G'_k(q) = |A(q)| \exp(i\Phi_k) \quad (2.46)$$

- (iii) Inverse Fourier transform this diffraction amplitude to yield object

$$g'_k(x) = |g'_k(x)| \exp(i\varphi_k) = \mathcal{F}^{-1}(G'_k(q)) \quad (2.47)$$

- (iv) Replace the modulus thus acquired with the magnitude of measured amplitude in the object plane

$$g_{k+1}(x) = |A(x)| \exp(i\varphi_k) \quad (2.48)$$

Repeat steps (ii) to (v) for desired number of iterations to get acceptable solution.

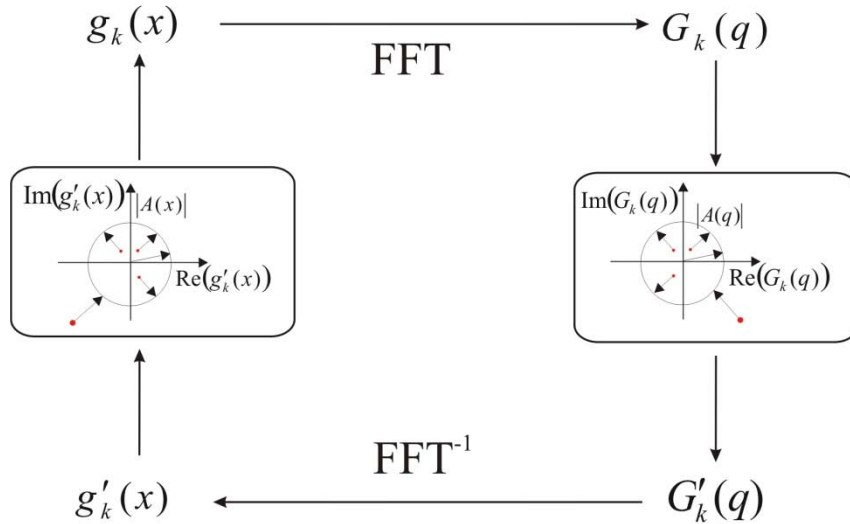


Figure 2.9 Gerchberg Saxton Algorithm

Fienup [2.8] proposed more generalized form of GS algorithm called as **error-reduction (ER) algorithm** which works for single intensity measurement in reciprocal space. Instead of real space intensity measurement, more generalized real space constraints of positivity and finite support (S) (Fig. 2.8) constraint requires that the real space density is occupied in a confined region. In particular the first three steps are identical to those of GS algorithm. The fourth step is replaced by the following (see Fig. 2.10):

$$g_{k+1}(x) = \begin{cases} g'_k(x) & , x \in S \\ 0 & , x \notin S \end{cases} \quad (2.49)$$

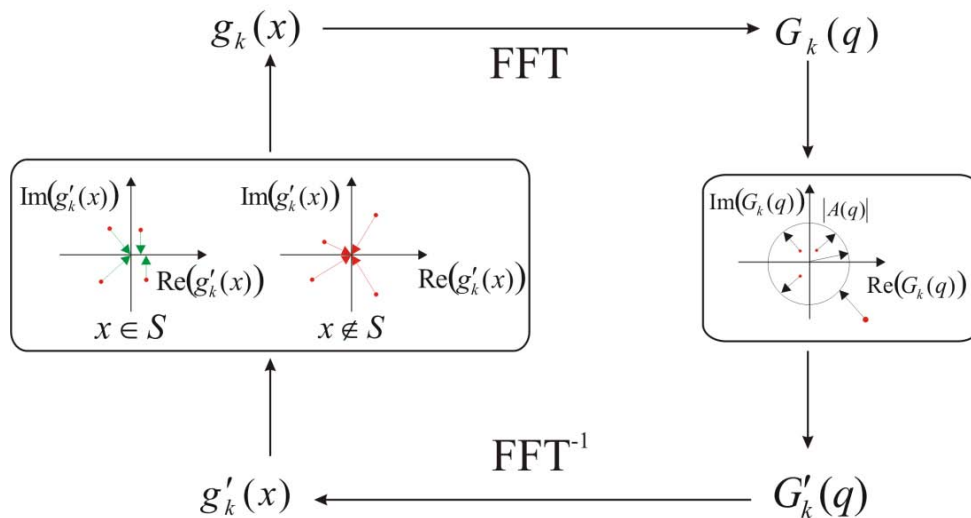


Figure 2.10 Error reduction algorithm



ER algorithm is in general poor in convergence and possesses a tendency to stagnate. This is overcome by a class of algorithms called as input-output algorithms. An input-output algorithm differs from ER algorithm only in object domain operation.

The first three steps in ER algorithm are retained but the real space constraint is enforced in different way. Here the input  $g_k(x)$  is no longer considered as a solution but as a driving function to produce the next output  $g'_k(x)$ . For a small change of the input  $g_k(x)$  the corresponding change of output is expected to be some constant  $\alpha$  times the change of the input. That is, if the input is  $g_k(x) + \Delta g_k(x)$  then the output is  $g'_k(x) + \alpha \Delta g_k(x)$ . The operation involved in getting  $g'_k(x)$  from  $g_k(x)$  is nonlinear and thus the exact changes in  $g'_k(x)$  cannot be predicted. Therefore the logical choice for the change of the input to produce the desired change of output becomes  $\beta \Delta g_k(x)$  instead of  $\Delta g_k(x)$ , with optimum value of  $\beta$  as  $\alpha^{-1}$ . Generally  $\alpha$  is not known and  $\beta$  is to be varied to get optimum value.

In case of single intensity measurement, the desired change in the output is

$$\Delta g_k(x) = \begin{cases} 0 & , x \in S \\ -g'_k(x) & , x \notin S \end{cases} \quad (2.50)$$

In the region S, where constraints are satisfied the output is not altered. In the region where constraints are violated  $g'_k(x)$  is changed in order to satisfy object-domain constraints. Thus a logical choice for the next input is

$$g_{k+1}(x) = g_k(x) + \beta \Delta g_k(x) \quad (2.51)$$

$$= \begin{cases} g_k(x) & , x \in S \\ g_k(x) - \beta g'_k(x) & , x \notin S \end{cases} \quad (2.52)$$

The algorithm with above driving function is **basic input-output (IO) algorithm**.

The interesting feature of the nonlinear operation is that if the output  $g'_k(x)$  is used as input, it gives output again as  $g'_k(x)$ . This gives another logical choice for the next input as

$$g_{k+1}(x) = g'_k(x) + \beta \Delta g_k(x) \quad (2.53)$$

$$= \begin{cases} g'_k(x) & , x \in S \\ g'_k(x) + \beta g_k(x) & , x \notin S \end{cases} \quad (2.54)$$

This is referred to as **output-output (OO) algorithm**. For  $\beta = 1$  output-output algorithm reduces to ER algorithm.

The OO algorithm also shares encounters the problem of stagnation as like ER algorithm but for some different reasons. This difficulty is overcome by combining basic IO and OO algorithms as follows (see Fig. 2.13):

$$g_{k+1}(x) = \begin{cases} g'_k(x) & , x \in S \\ g_k(x) - \beta g'_k(x) & , x \notin S \end{cases} \quad (2.55)$$

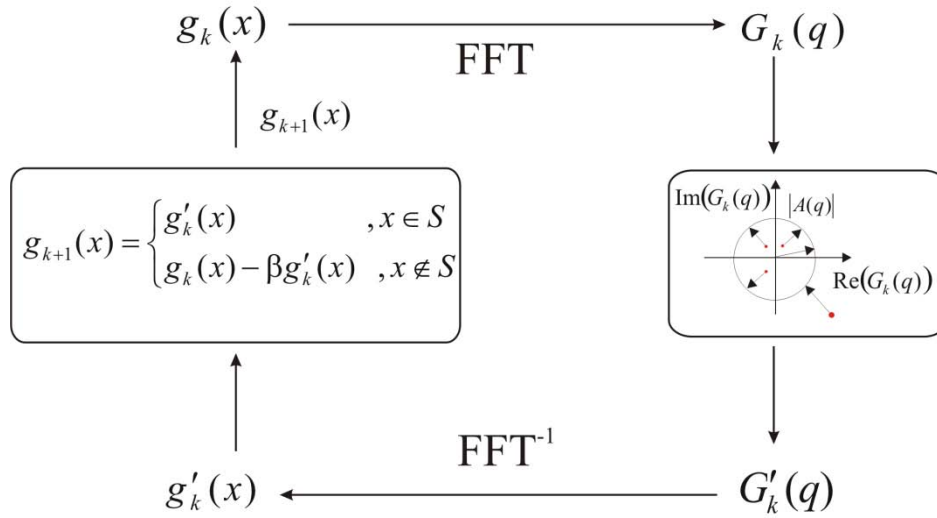


Figure 2.13 Hybrid input-output algorithm

This is called as **hybrid input-output (HIO) algorithm** as it creates hybrid driving function composed of input  $g_k(x)$  and output  $g'_k(x)$ .

Millane [2.9] modified HIO algorithm and introduced a general constraint function  $c_k(x)$  instead of positivity and support constraints. Here the real space constraint is changed to

$$g_{k+1}(x) = \begin{cases} g'_k(x) & , \text{if } |c_k(x) - g'_k(x)| \leq \varepsilon \\ g_k(x) - \beta(g'_k(x) - c_k(x)) & , \text{if } |c_k(x) - g'_k(x)| > \varepsilon \end{cases} \quad (2.56)$$

The constraint is the requirement that  $g'_k(x)$  agrees with the constraint function  $c_k(x)$  with small amount  $\varepsilon$ .

### 2.5.1 Uniqueness and Oversampling

The critical point of interest in reconstruction is the uniqueness of the solution. Consider  $f$  as a solution to the phase problem such that the scattering amplitude is  $A = \mathcal{F}(f)$ . In general, the

solution  $f$  is not unique and an infinite set of alternative solutions can be generated from  $f$ . Three trivial alternative solutions are:  $e^{i\theta}f(x, y)$ ,  $f^*(-x, -y)$  and  $f(x + x_0, y + y_0)$ . A constant phase shift  $e^{i\theta}$  gives the same solution for intensity  $I(q_x, q_y) = |A(q_x, q_y)|^2 = |\mathcal{F}(e^{i\theta}f(x, y))|^2$ . Thus two solutions with constant phase difference cannot be distinguished. The second alternative  $f^*(-x, -y)$  also gives the same intensity  $I(q_x, q_y) = |\mathcal{F}(f^*(-x, -y))|^2$ . The alternate solutions of this form are called as “duals” or “twin images”. Also the alternate solution generated by shifting of origin  $f(x + x_0, y + y_0)$  gives the same intensity  $I(q_x, q_y)$  and thus is indistinguishable from  $f(x, y)$ .

The success of reconstruction of iterative phase retrieval depends on things like sampling of the data and real space constraints based on *a priori* knowledge of the sample. In real experiment the intensity is measured for a finite region of reciprocal space and is sampled at a particular frequency. For such a discretely sampled data uniqueness of the solution is decided by the number of unknowns and the number of equations in the phase problem. The scattering amplitude in terms of discrete Fourier transform is

$$A(q_x, q_y) = \sum_{x,y} f(x, y) \exp \left[ \frac{2\pi i}{M} (q_x x) + \frac{2\pi i}{N} (q_y y) \right] \quad (2.57)$$

The physical sizes of discrete steps in  $x$  and  $y$  are related to the steps in  $q_x$  and  $q_y$  by

$$\Delta x \Delta q_x = \frac{2\pi}{M} \quad \text{and} \quad \Delta y \Delta q_y = \frac{2\pi}{N}$$

From the measurement of intensity array only the magnitude of the scattered amplitude  $A(q_x, q_y)$  is known. This yields  $MN$  equations, one for each reciprocal space point  $(q_x, q_y)$ . But there are  $2MN$  unknowns corresponding to the real and imaginary parts of each of the  $MN$  values of  $f(x, y)$ . In order to obtain a solution in such a case the reciprocal space is to be finely sampled by at least a factor of two. Thus the number of equations becomes  $\geq 2MN$ . Such oversampling in reciprocal space is equivalent to padding the real space array with a known set of zeros. Thus the region with nonzero value of  $f(x, y)$ , i.e. support, contains less than half of the whole array. The oversampling ratio [2.10]

$$\sigma = \frac{\text{Size of Array}}{\text{Size of Object}}$$

characterizes the degree of oversampling in reciprocal space.

In other words, the intensity represents Fourier transform of autocorrelation function  $f(x, y) \otimes f(-x, -y)$ . The autocorrelation is nonzero over an interval twice the size of the object. Thus the intensity should be sampled at least twice as finely as the amplitude.

## 2.6 References

- [2.1] M. Tolan, *X-ray scattering from soft matter thin films*, Springer Tracts in Modern Physics Vol. 148, Springer Verlag (1999)
- [2.2] J. Als-Nielsen, D. McMorrow, *Elements of Modern X-ray Physics*, John Wiley & Sohns Ltd. (2001)
- [2.3] W. Lauterborn, T. Kurz, *Coherent Optics: Fundamentals and Applications*, Second Edition, Advanced Texts in Physics, Springer Verlag (2003)
- [2.4] F. van der Veen, F. Pfeiffer, *Coherent X-ray Scattering*, J. Phys: Condns. Matter 16, 5003-5030, (2004)
- [2.5] Miao, J. *et al.*, *Extending the methodology of X-ray crystallography to allow imaging of micrometre-sized non-crystalline specimens*, Nature (London), 400, 342–344, (1999)
- [2.6] M. Born, E. Wolf, *Principles of Optics*, 7<sup>th</sup> edition, Cambridge University Press (2005)
- [2.7] R. W. Gerchberg, W. Saxton, *Phase determination from image and diffraction plane pictures in the electron microscope*, Optik, 35, 237-246, (1972)
- [2.8] J. R. Fienup, *Phase retrieval algorithms: a comparison*, Appl. Opt. 21, 2758-2769, (1982)
- [2.9] R.P. Millane, W. J. Stroud, *Reconstructing symmetric images from their undersampled Fourier intensities*, J. Opt. Soc. Am. A 14, 568-579, (1997)
- [2.10] J. Miao, D. Sayre, H. N. Chapman, *Phase retrieval from magnitude of the Fourier transforms of nonperiodic objects*, J. Opt. Soc. Am. A 15, 1662-1669, (1998)

## Chapter 3

### Experimental Details

This chapter shortly describes the experimental set up for the static speckle experiments using white x-rays at a synchrotron source. The experiments are performed at the Energy Dispersive Reflectometry (EDR) beamline at the synchrotron source of Berliner Elektronenspeicherring Gesellschaft für Synchrotronstrahlung II (**BESSY II**) in Berlin (Germany). The experimental conditions at the EDR beamline are discussed in the chapter. This chapter explains the peculiarities of energy dispersive experimental techniques. It also describes the kinds of scans possible at the beamline and the transformation of these scans into reciprocal space. The performance of the beamline is elaborated through an example of small angle x-ray scattering (SAXS) experiment.

#### 3.1 Energy Dispersive Reflectometry (EDR) beamline

The lay-out of EDR beamline is as shown in Fig. 3.1. It is a bending magnet beamline with no optical elements such as monochromators or focusing devices along the beam path after the bending magnet. Three pairs of slits viz. primary, secondary and exit are used for spatial confinement of the x-ray beam emitted at the bending magnet. A window with 50  $\mu\text{m}$  thick Be foil separates storage ring vacuum from high vacuum tube through which the x-ray beam is guided till the final exit window. Finally the x-ray beam exits the vacuum tube through a Kapton window located at around 30 m downstream the storage ring. The integrated intensity of incoming x-ray beam can be tuned by passing it through an absorber box comprising of Al plates with thickness 0.1, 0.2, 0.4, 0.8, 2, 4 mm. These plates provide attenuation factor of 0.27, 0.07,  $5.7 \times 10^{-3}$ ,  $3.3 \times 10^{-5}$ ,  $6.4 \times 10^{-12}$ ,  $4.2 \times 10^{-23}$  at 8 keV of photon energy respectively. The thickness of Al absorbing plate/s decides the onset of energy spectrum of incoming x-ray beam. Before the Kapton window inside the vacuum two multilayer super mirrors are optionally available. They can be used to make the x-ray beam incident on liquid surfaces to maximum angle of  $2^\circ$  to measure their reflectivity.

## Experimental Details

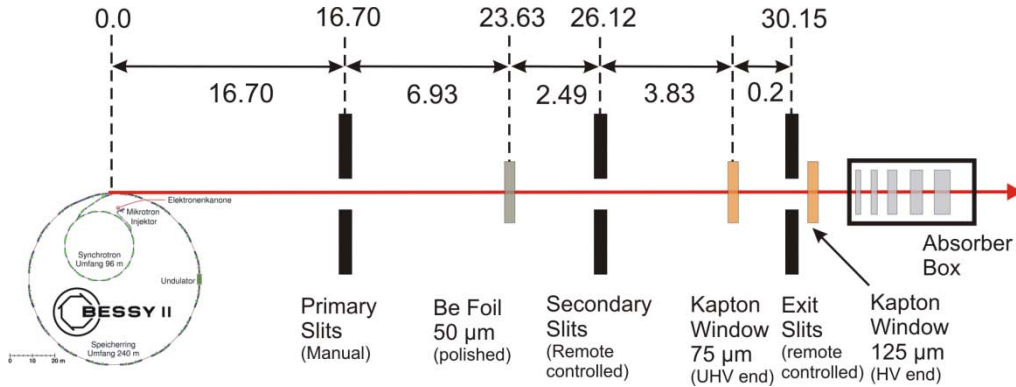


Fig. 3.1 Layout of EDR beamline. All the distances are in meter.

For the experiments with coherent beam, spatial confinement of the incoming beam less than the coherence length is necessary. This is achieved with the help of an entrance pinhole placed before the sample. A set of pinholes with different sizes 10, 15, 25, 50 and 100  $\mu\text{m}$  is available at the EDR beamline. The proper alignment of entrance pinhole in the incoming beam is important and hence the stage with the set entrance pinholes is assembled on an optical table. The optical table has dimensions 1.8 m  $\times$  1.6 m and it is placed inside radiation protected hutch. The entrance pinhole can be aligned in the incident beam with the help of horizontal and vertical motors. These motors can be moved with step size of 0.1  $\mu\text{m}$ .

The sample is placed on a HUBER goniometer. The sample can be properly aligned in the x-ray beam with the help of eight different motor movements of HUBER goniometer. These eight different motor movements available are as following:

incident angle rotational movement with step size 0.002 $^\circ$ ,

horizontal movement perpendicular to the direction of the beam for aligning the center of rotation with step size of 2.5  $\mu\text{m}$ ,

azimuthal rotational movement with step size 0.0025 $^\circ$ ,

vertical movement with step size 0.1  $\mu\text{m}$ ,

two horizontal movements with step size of 2.5  $\mu\text{m}$  independent of the movement of the center of rotation,

two rotational movements with step size of 0.0025 $^\circ$  to align the surface of the sample parallel to the beam.

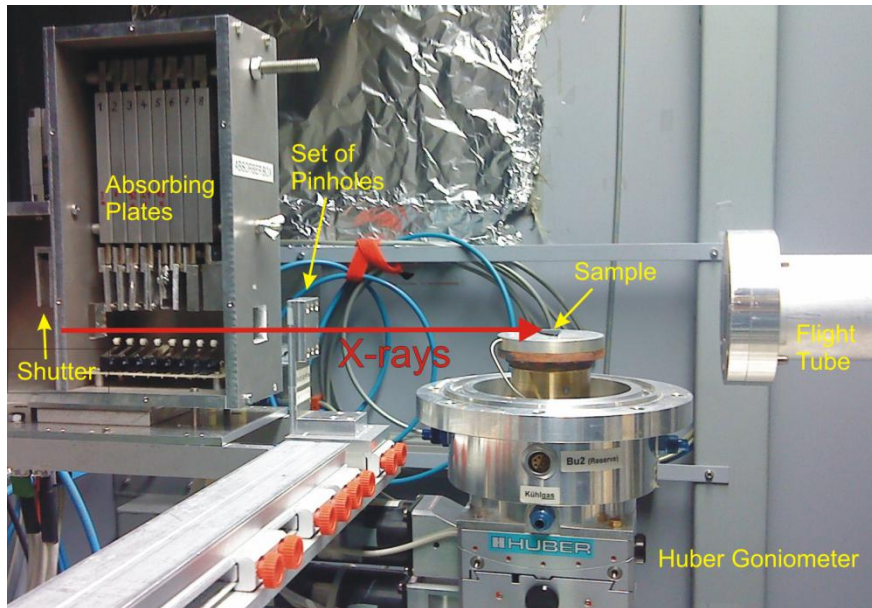


Fig. 3.2 Experimental set up at EDR beamline

The energy dispersive detector (more details in section 3.1.1) is placed on a stage with vertical movement with step size of  $0.1 \mu\text{m}$ , horizontal movement perpendicular to the beam with step size of  $2.5 \mu\text{m}$  and with rotational movement with step size of  $0.0025^\circ$  for the exit angle.

These motor movements facilitate proper alignment of the sample and detector in the incident and reflected x-ray beam, which is very critical in case of coherent reflectivity experiments. The reflected beam from the sample reaches the detector through an evacuated flight tube with entrance and exit Kapton windows and of length 1 m to reduce air absorption.

A pair of vertical and horizontal slits can be used in front of detector. Optionally a pinhole of various sizes 5, 10, 15, 20 to  $25 \mu\text{m}$  can be placed in front of detector. Proper choice of the detector pinhole decides the desired spatial resolution for the measurement.

The movement of pinhole stage, sample stage and detector stage is remotely controlled by the translation and rotational stages through 3 independent HUBER controllers each with 8 independent channels. For the control of movements of all the motors Certified Scientific Software's Spec 5 is used. Spec 5 can also acquire measured energy spectrum from the detector.

### 3.1.1 Energy dispersive detector

The energy dispersive detector used for measurement of x-rays is XFLASH 1000 detector from Röntec (now owned by Bruker). It is a silicon drifted diode detector with linear response up to integral photon count rate of  $10^6$  counts/s. Linearity in response is lost for higher count rates due to dead time and pile up effect. The working principle and physical background of such detectors can be found in Ref. [3.1]. It has active area of  $2 \times 2 \text{ mm}^2$ . Pinhole of size in the range of few microns is used so as to achieve the desired spatial resolution for scanning the speckle pattern.

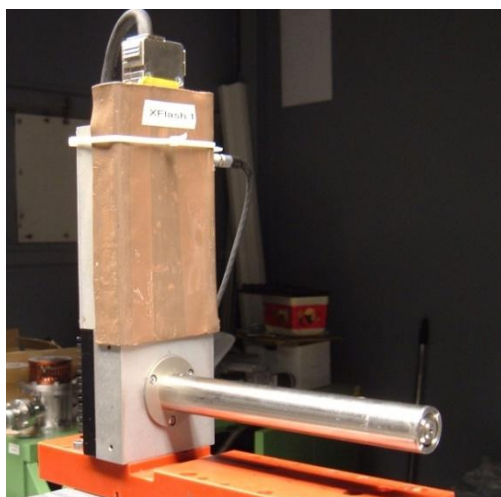


Fig 3.3 Photograph of Detector

It can measure intensities of x-rays within the energy of 0 to 80 keV but alternatively energy range of 0 - 20 keV or 0 - 40 keV can be chosen. For the present work energy range of 0-40 keV is used. The Multi Channel Analyzer (MCA) of the detector has 4095 channels. As the channel for zero point energy starts at 95<sup>th</sup> channel, 4000 channels out of 4095 are actually used for the measurement. It is essential to calibrate the detector to get the relation between channel number and energy of photons. Calibration is done by measuring Florescence from standard materials like Cu, Fe. One such measurement is shown in Fig. 3.5.



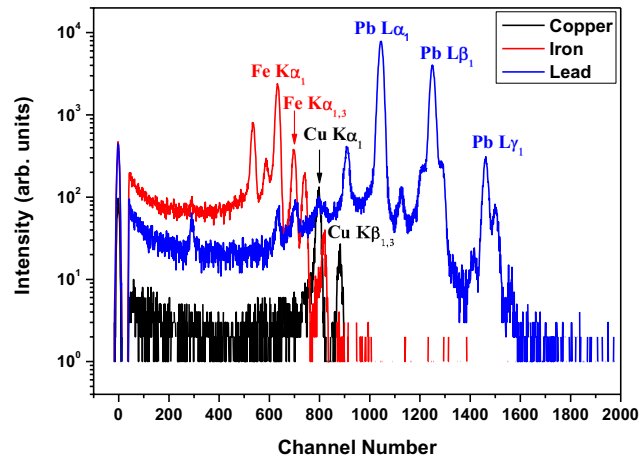


Fig. 3.5 Fluorescence measurements from 3 different samples of Cu, Fe, Pb. Major emission lines are identified and used for calibrating energy range of detector.

Using these Fluorescence lines the equation for calibration of the detector becomes

$$Energy(eV) = -952.18 + 10.08 \times (Channel\ Number) \quad (3.1)$$

Energy resolution of the detector is  $\sim 200$  eV in the energy range 2 to 40 keV. With increasing number of counts, additional peaks appear at high energies called as “pile up” [3.2, 3.3].

After measurement of signal, data is serially transferred to data acquisition computer. So as to reduce the amount of data to be transferred to the computer data binning is optionally available. Typically binning of factor 10 is used so that transferred data is an array of 410 different values. The average time between two spectra is 2.5 s, which is needed to transfer the data from MCA to the computer and storage of the data on hard disc.

### 3.1.2 Bending magnet emission at EDR

The Energy Dispersive Reflectometry (EDR) beamline provides white x-ray spectrum in hard x-ray regime emitted at bending dipole magnet at the BESSY storage ring. It exploits the exponentially decaying hard x-ray tail of the 1.7 GeV emission spectrum at bending magnet of BESSY II. The maximum useful energy in the spectrum with reasonable statistics is around 30 keV. The spectrum emitted at bending magnet is calculated by using software called X-ray Oriented Programs (XOP) developed at ESRF. The critical energy for bending magnet emission depends on the strength of magnetic field of bending magnet (B) and energy of

electrons (E) in the storage ring. At EDR beamline with  $B = 0.95$  T and  $E = 1.72$  GeV, the critical energy is 1.8 keV. Fig. 3.5 shows the calculated emission spectrum at EDR beamline at electron current of 100 mA.

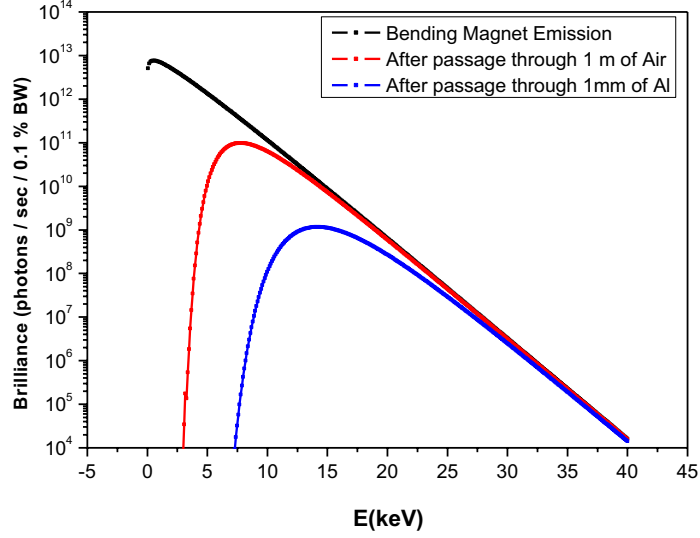


Fig. 3.5 Emission from bending magnet at BESSY II calculated using XOP. The spectrum gets modified due to absorption through medium like air and Al.

This spectrum gets modified at lower energies due to absorption effects through various media like air, Al absorbers. The transmitted intensity can be calculated by using the following law

$$I(E) = I_0(E)e^{-\mu(E)x} \quad (3.2)$$

Here  $I_0(E)$  is the intensity of incoming x-ray beam,  $\mu$  is linear absorption coefficient and  $x$  is the length of the path in the medium or in other words thickness of the medium. For x-rays the linear absorption coefficient  $\mu$  is a function of energy (E) of x-rays. The dependence of  $\mu$  on energy is calculated using XOP. At the EDR beamline after the exit window in vacuum the x-ray beam passes through air and through Al absorber plates of desired thickness. The transmitted intensity can be found by considering both the contributions

$$I(E) = I_0(E)(e^{-\mu_{air}(E)x_{air}}e^{-\mu_{Al}(E)x_{Al}}) \quad (3.3)$$

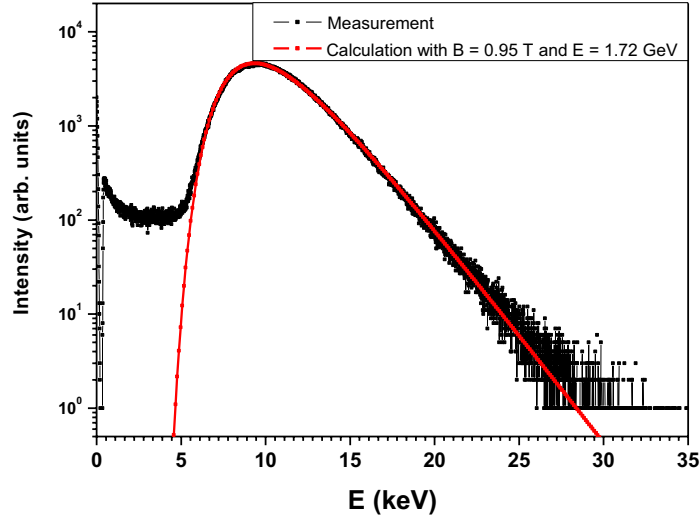


Fig. 3.6 Measured spectrum (black) with 1 m of air passage and 1 mm of Al absorber and its fit (red) calculated using XOP

Fig. 3.6 shows the total intensity measured (black) after passage of 1m through air and through 1 mm thick Al absorber plate. Figure also shows the fit (red) calculated using XOP based on equation (3.3) (as in Fig. 3.5) to the measured intensity (black). The thickness of Al absorbing plate decides the integral intensity incident on the sample and the onset of the spectrum in lower energy regime.

### 3.2 Experimental scans:

As discussed in Chapter 2 *wave vector transfer  $\mathbf{q}$*  is very essential entity to describe elastic scattering processes. As the dimension of *wave vector transfer  $\mathbf{q}$*  is the inverse of length, it is convenient to describe a scattering experiment in reciprocal space [3.4]. Scattered intensity can be expressed independent of angular variables or wavelength of radiation in reciprocal space. The co-ordinate system is chosen as laboratory system with Cartesian co-ordinates along  $q_x$ ,  $q_y$  and  $q_z$  centered at the origin of reciprocal lattice. Fig. 3.7 shows the geometry with incident vector  $\mathbf{k}_i$ , scattered vector  $\mathbf{k}_f$  and wave vector transfer  $\mathbf{q}$ .

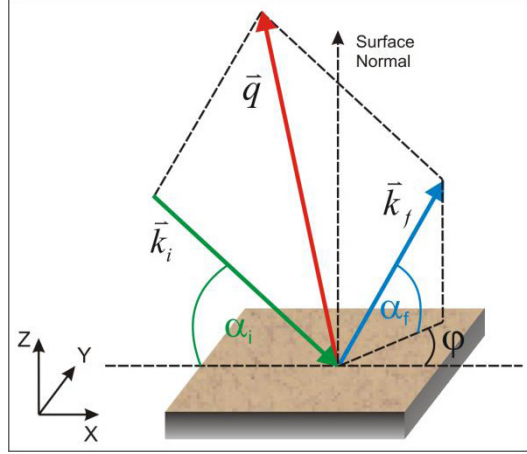


Fig. 3.7 Reciprocal space vectors for elastic scattering ( $|k_i| = |k_f|$ )

$q_z$  axis is chosen parallel to the surface normal and  $q_x$  axis parallel to the in-plane component of  $k_i$ . The components of  $k_i$ ,  $k_f$  and  $q$  in terms of angular variables  $\alpha_i$  and  $\alpha_f$  are as follows:

$$\mathbf{k}_i = k(\cos\alpha_i, 0, -\sin\alpha_i) \quad (3.5)$$

$$\mathbf{k}_f = k(\cos\alpha_f \cos\phi, \cos\alpha_f \sin\phi, \sin\alpha_f) \quad (3.6)$$

$$\mathbf{q} = \mathbf{k}_f - \mathbf{k}_i = k(\cos\alpha_f \cos\phi - \cos\alpha_i, \cos\alpha_f \sin\phi, \sin\alpha_f + \sin\alpha_i) \quad (3.7)$$

The wave vector transfer  $q$  can be written in terms of energy of x-ray radiation as:

$$\mathbf{q} = \frac{2\pi E}{hc} (\cos\alpha_f \cos\phi - \cos\alpha_i, \cos\alpha_f \sin\phi, \sin\alpha_f + \sin\alpha_i) \quad (3.8)$$

where  $h = 6.626 \times 10^{-34}$  Js is the Planck's constant and  $c = 3 \times 10^8$  m/s.

$$\mathbf{q} = \frac{2\pi E}{12.398} (\cos\alpha_f \cos\phi - \cos\alpha_i, \cos\alpha_f \sin\phi, \sin\alpha_f + \sin\alpha_i) \quad (3.9)$$

with energy ( $E$ ) is expressed in units keV and  $q$  in  $\text{\AA}^{-1}$ .

In conventional angular scans the components of  $q$  are varied by varying the angular variables  $\alpha_i$  and/or  $\alpha_f$ . In case of energy dispersive scattering set up variation of the components of  $q$  can be achieved because of multiple energies of the white x-ray beam while keeping the sample at fixed angle of incidence  $\alpha_f$ . The variation of vector  $q$  gives different scans in reciprocal space.

With the help of experimental set up at EDR beamline following scans are possible:

1. Specular scan: Intensity distribution is recorded as a function of energy ( $E$ ) at specular condition i.e.  $\alpha_i = \alpha_f$  and thus  $q_x = 0$ .
2. Detector scan: Intensity distribution is recorded by changing only the exit angle  $\alpha_f$  for fixed angle of incidence  $\alpha_i$  (Fig. 3.8) or by displacing the detector along  $z$  direction and measuring the energy spectrum at each  $z$  position. At each  $z$  position of the detector the energy spectrum corresponds to a line scan in  $q_x$ - $q_z$  space (Fig. 3.9).

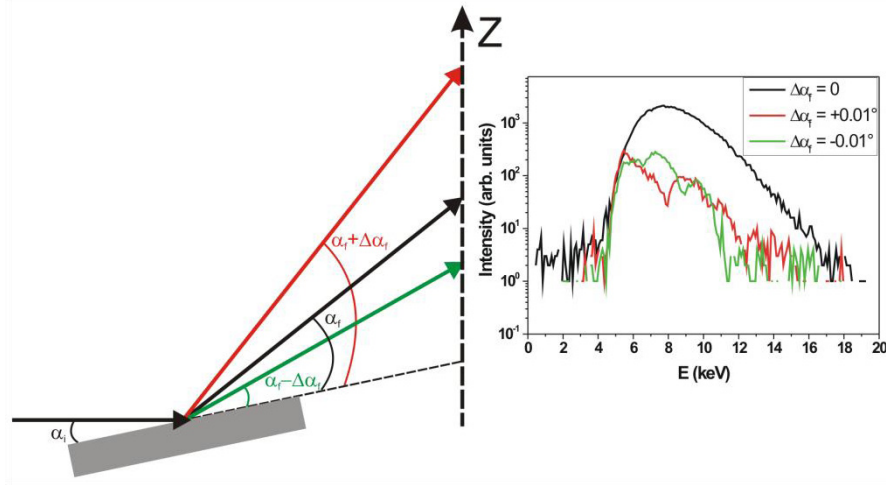


Fig 3.8 Detector scan with white beam and the corresponding spectra

Fig. 3.9 shows the representation of the detector scans at different offsets of exit angle ( $\Delta\alpha_f$ ). The scan at  $\Delta\alpha_f = 0$  (black curve) corresponds to the specular position where  $\alpha_i = \alpha_f$ . The energy spectrum gives a line parallel to energy axis in  $(E - z)$  space. Energy spectra can be recorded at different position of offset of exit angles, for example  $\Delta\alpha_f = -0.02^\circ, -0.01^\circ, +0.01^\circ, +0.02^\circ$ . Each of these lines gives a line parallel to energy axis in  $(E - z)$  space, for example green, blue, red and light blue curves in right of Fig. 3.9.

These scans can be translated in reciprocal space using the following equations (3.10) and (3.11) obtained from equation (3.9) with the in-plane angle  $\varphi = 0$ .

$$q_x = \frac{2\pi E}{12.398} (\cos \alpha_f - \cos \alpha_i) \quad (3.10)$$

$$q_z = \frac{2\pi E}{12.398} (\sin \alpha_f + \sin \alpha_i) \quad (3.11)$$

with energy ( $E$ ) expressed in keV and the reciprocal space vectors  $q_x, q_z$  in  $\text{\AA}^{-1}$ .

Each of these detector scans gives a line scan in  $(q_x, q_z)$  space (Fig. 3.9 right). The scan at specular position (black curve) gives a line scan parallel to  $q_z$  –axis. The other scans (green, blue, red and light blue) span certain  $q_x$  and  $q_z$  range depending on angle of incidence  $\alpha_i$ , offset of exit angle  $\Delta\alpha_f$  and the energy range measured (for example 0-30 keV in this case).

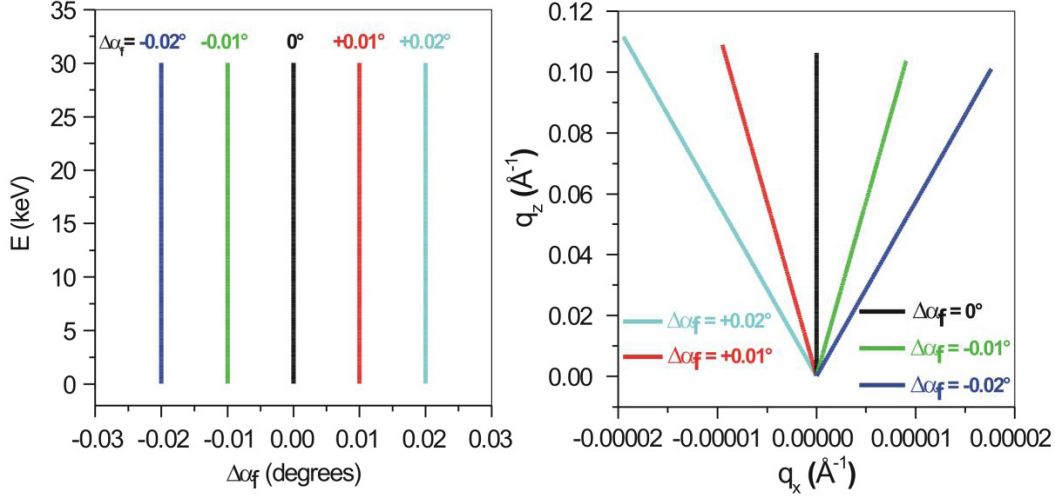


Fig. 3.9 Experimental detector scans in (a) E-z space (b)  $q_x$ - $q_z$  space

### 3.3 Diffraction from entrance pinhole

Transverse coherence length of the source at EDR beamline can be estimated with the help of equation (2.39). The root mean square size of the source is  $\sigma_v = 45 \pm 5 \mu\text{m}$  and  $\sigma_h = 55 \pm 5 \mu\text{m}$  [3.5]. At a distance of 24.36 m from the source the coherence lengths at 8 keV are  $\xi_v = 42 \mu\text{m}$  and  $\xi_h = 34 \mu\text{m}$ . In order to make experiments with coherent beam the incoming beam has to be confined spatially. Pinholes of different sizes from 5 to 35  $\mu\text{m}$  are available for this purpose. By choosing the pinhole of size less than the transverse coherence length ensures that the incoming beam striking the sample is coherent. Such a pinhole gives rise to Fresnel diffraction pattern at the position of sample (Fig. 3.10 (B)). This diffraction pattern in the form of Airy (disc) pattern is comprised of alternate rings of maxima and minima. Normally, in case of monochromatic beam, central maximum part of this pattern is chosen with the help of a second pinhole called guard pinhole placed at specific distance from the pinhole (Fig. 3.10(A)). The size of the guard pinhole is chosen to be smaller than the size of the first minimum of the diffraction pattern of the entrance pinhole. This eliminates the second or higher order fringes of the diffraction pattern to fall on the sample.

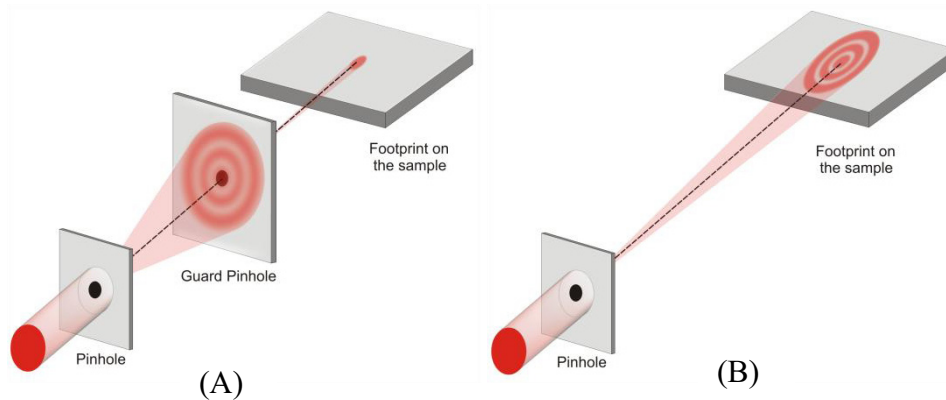


Fig. 3.10 Footprint on the sample with and without guard pinhole

In case of polychromatic beam, the diameter of Airy discs depends on the energy of radiation. As the energy of radiation increases diameter of Airy discs reduces. Thus a guard pinhole, however small, chosen to block the higher order fringes for a particular energy, it can pass higher order fringes for energies higher than that energy. Therefore it is not possible to use a guard pinhole at energy dispersive set up and one has to bear with the higher order fringes of the diffraction pattern of the pinhole (Fig 3.10-3.11).

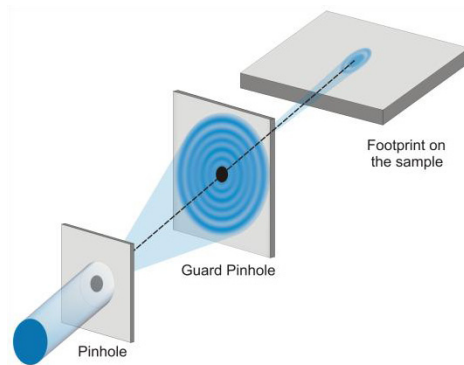


Fig. 3.11 Guard pinhole and footprint on the sample at higher energy than in Figure 3.7

The diffraction pattern of pinhole at the positions on the sample is investigated [3.3, 3.6]. The diffraction pattern from pinholes with different diameters are measured and numerically simulated. The numerical calculations are based on the Lommel formalism for Hygens – Fresnel integral.

### 3.3.1 Lommel Formalism for Fresnel Diffraction through Circular Aperture

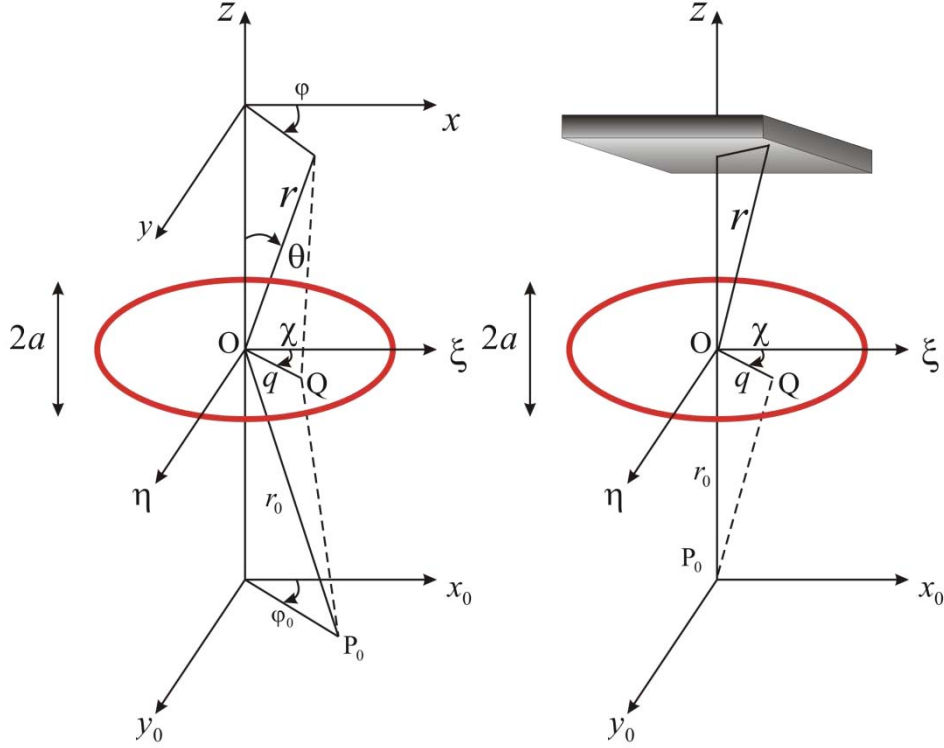


Fig. 3.12 Circular aperture and the co-ordinate system

Let us consider a pinhole or circular aperture with diameter  $2a$ . For the arrangement as shown in Fig. 3.12 the Fresnel diffraction integral is

$$\alpha_F(P) = \frac{ik(r_0 + r)}{2\pi r_0 r} \int dQ e^{ik\Delta(Q)} \quad (3.12)$$

where  $\Delta(Q) = (P_0Q + QP) - (P_0O + OP)$  is the path difference.

Here spherical coordinate system is considered with origin at O, with

$$P_0 = (x_0, y_0, z_0) = r_0(\cos\varphi_0 \sin\theta_0, \sin\varphi_0 \sin\theta_0, \cos\theta_0),$$

$$Q = (\xi, \eta, 0) = q(\cos\chi, \sin\chi, 0),$$

$$P = (x, y, z) = r(\cos\varphi \sin\theta, \sin\varphi \sin\theta, \cos\theta)$$

and by considering the following variables

$$\rho = \frac{q}{a}, u = \frac{ka^2(r_0 + r)}{r_0 r}, v = \frac{kac}{r}$$



the amplitude of diffracted wave is given by

$$\alpha_F(P) = -iu \int_0^1 \rho J_0(v\rho) e^{\frac{i}{2}u\rho^2} \quad (3.12)$$

According to Lommel Formalism the integral in equation (3.10) can be expressed as

$$\int_0^1 d\rho \rho J_0(v\rho) e^{\frac{i}{2}u\rho^2} = \frac{1}{2} [L(u, v) + iM(u, v)] \quad (3.13)$$

So that the amplitude becomes

$$\alpha_F(u, v) \equiv a_L(u, v) = \frac{u}{2} M(u, v) - i \frac{u}{2} L(u, v) \quad (3.14)$$

Where  $L(u, v)$  and  $M(u, v)$  are defined by

$$\frac{u}{2} L(u, v) = \begin{cases} \sin \frac{v^2}{2u} + V_0(u, v) \sin \frac{u}{2} - V_1(u, v) \cos \frac{u}{2} & v < u \\ U_1(u, v) \cos \frac{u}{2} + U_2(u, v) \sin \frac{u}{2} & v > u \end{cases} \quad (3.15)$$

$$\frac{u}{2} M(u, v) = \begin{cases} \cos \frac{v^2}{2u} - V_0(u, v) \cos \frac{u}{2} - V_1(u, v) \sin \frac{u}{2} & v < u \\ U_1(u, v) \sin \frac{u}{2} - U_2(u, v) \cos \frac{u}{2} & v > u \end{cases} \quad (3.16)$$

Where the functions  $V_0, V_1, U_0, U_1$  are defined as

$$V_0(u, v) = \sum_{n=0}^{\infty} (-1)^n \left(\frac{v}{u}\right)^{2n} J_{2n}(v) \quad (3.17)$$

$$V_1(u, v) = \sum_{n=0}^{\infty} (-1)^n \left(\frac{v}{u}\right)^{2n+1} J_{2n+1}(v) \quad (3.18)$$

$$U_1(u, v) = \sum_{n=0}^{\infty} (-1)^n \left(\frac{u}{v}\right)^{2n+1} J_{2n+1}(v) \quad (3.19)$$

$$U_2(u, v) = \sum_{n=0}^{\infty} (-1)^{n+1} \left(\frac{u}{v}\right)^{2n} J_{2n}(v) \quad (3.20)$$

For a reasonable numerical result the sums of at least 30 terms are evaluated in equations (3.16) - (3.19). The numerical calculation is obtained using an Origin C program on a personal computer with 3.2 GHz processor and 1 GB RAM.

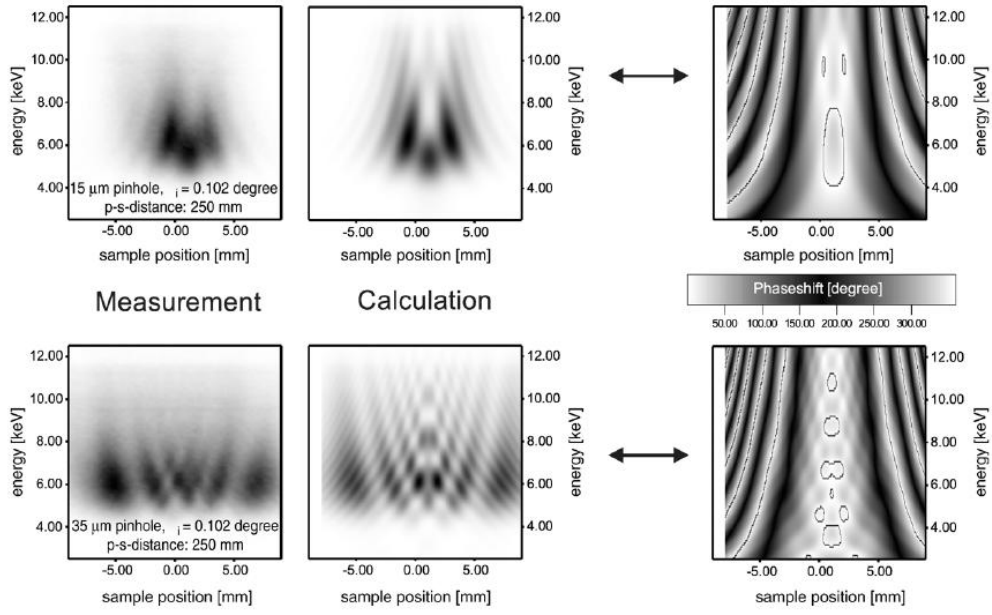


Fig. 3.13 The measured and simulated Fresnel diffraction pattern of pinholes with diameters 15  $\mu\text{m}$  and 35  $\mu\text{m}$  [3.3, 3.6]

Fig 3.13 shows the measured diffraction pattern and the simulated result for pinholes with 2 different diameters. The detector was placed at sample position, 250 mm downstream from the pinhole. The energy spectra are measured at sample position keeping fixed angle of incidence of  $0.102^\circ$ . The x coordinate in the Fig. 3.13 corresponds to the coordinate along the sample position at this fixed angle of incidence. Spatial resolution of the detector is improved by using a pinhole of 5  $\mu\text{m}$  in front of the detector.

Fresnel fringes are clearly visible in the measured diffraction map. Fringes can be seen to become narrower at higher energies. Due to the absorption effects at lower energies the maximum in the incident spectrum is observed at  $\sim 6$  keV. The diffraction intensity drops at higher energies because of the exponentially decaying intensity of incident beam at higher energies. The numerical simulation shows good agreement with the measured diffraction pattern. This allows one to use the diffracted amplitude  $B(x, y)$  along with its phase  $\varphi_F(x, y)$  for further calculations.

From equation (3.12), (3.13) and (3.14)

$$B(x, y) = \frac{u}{2} \sqrt{M^2(u, v) + L^2(u, v)} \quad (3.22)$$

$$\varphi_F(x, y) = \arg(a_L(u, v)) \quad (3.23)$$

The knowledge of the amplitude and phase of the illumination function plays a vital role in reconstructing the surface profile from the measured scattering data. The influence of illumination function on the coherent reflectivity pattern is extensively investigated by T. Panzner [3.3].

### 3.4 Demonstration of energy dispersive techniques: EDSAXS

The experimental set up at EDR beamline allows one to perform different kinds of scattering experiments. The unique feature of the energy dispersive scattering techniques is elaborated through an experiment of Energy Dispersive Small Angle X-ray Scattering (EDSAXS). In case of angular dispersive technique scattered intensity is measured as a function of scattering angle. In EDSAXS scattered intensity is measured as a function of energy at fixed scattering angle.

This experiment of EDSAXS exhibits the unique features of set up at EDR beamline. The set up is relatively simple with only one external slit to collimate the beam. The measurement of scattering over wide  $q$  range can be achieved even with single measurement which needed only 180 seconds in this case. The measurement time can be reduced further by improving the measurement set up. The monochromatic measurement at in-house set up took 3 hrs for the measurement over the same  $q$  range. Such a fast measurement is useful in systematic investigation of large series of samples or study of slow dynamics processes.

For simplicity, we describe the scattering in terms magnitude of wave vector transfer  $q$  as

$$q = \frac{4\pi \sin \theta}{\lambda} \quad (3.24)$$

where  $\theta$  is the scattering angle.

It can be expressed in terms of energy of radiation ( $E$ ) as [3.7]

$$q = \frac{4\pi E \sin \theta}{12.398} \quad (3.25)$$

with  $q$  in  $\text{\AA}^{-1}$  and energy  $E$  in keV.

For small angles, with good approximation  $q$  can be written as

$$q \approx \theta \cdot E \quad (3.26)$$

A single measurement of energy spectrum ( $E = 0$  to 40 keV) for scattered radiation at fixed  $\theta$  covers a specific range of  $q$  values simultaneously. Different  $q$  range can be accessed by taking measurement at different scattering angle.

Au nanoparticles suspended water with size 12 nm are investigated. The nanoparticles with low polydispersity are selected, thus expected to show narrow peaks in the scattering. Fig. 3.14 shows the scattering for 12 nm Au nanoparticles.

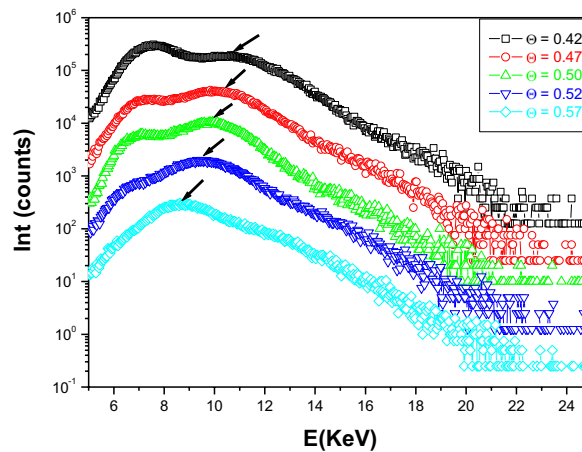


Fig. 3.14 Small angle scattering energy spectra from 12 nm Au nanoparticles

The characteristic incident spectrum, as in Fig. 3.6, gets modified due to the form factor of 12 nm nanoparticles. The scattering is measured at different scattering angles. The peak can be observed to shift to lower energies with increasing scattering angle. Due to the exponential behavior of the incident spectrum the scattering from the nanoparticle is not distinctly visible. To remove the influence of the incident spectrum, all the measured spectra are normalized by the scattering from pure distilled water measured at scattering angle of  $0.18^\circ$ . Fig. 3.15 shows the normalized spectra as a function of  $q$ .

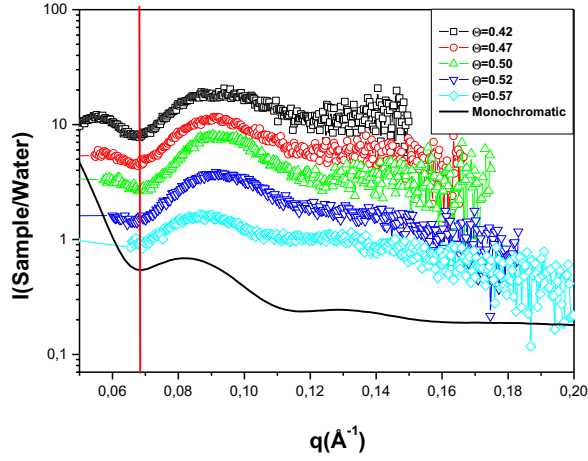


Fig. 3.15 SAXS measurement in reciprocal space with white and monochromatic x-rays

The monochromatic SAXS measurement with  $1.54 \text{ \AA}$  x-ray radiation at an in-house set up is also given for comparison. All the energy dispersive measurements at different scattering angle show first minimum at  $0.0668 \text{ \AA}^{-1}$  which agrees well with the monochromatic measurement.

The intensity of scattered x-rays from a dilute system of solid spherical particles of material with average mass density  $\rho_0$  is given by

$$I(q) = \rho_0^2 V^2 P(q) \quad (3.24)$$

where  $V$  is the total illuminated volume. The form factor  $P(q)$  for spherical particles is

$$P(q) = \left[ \frac{3(\sin qR - qR \cos qR)}{(qR)^3} \right]^2 = \left[ \frac{3 J_1(qR)}{qR} \right]^2 \quad (3.25)$$

where  $R$  is the mean radius of the particles and  $J_1(x)$  is the spherical Bessel function of the first order.

The form factor  $P(q)$  and hence the intensity  $I(q)$  has the first minimum at

$$q_{min}R = 4.5 \quad (3.26)$$

Using this for  $q_{min} = 0.068 \text{ \AA}^{-1}$ , radius of nanoparticles is determined to be  $6.6 \text{ nm}$ , which agrees fairly well with the independent determination of size (diameter)  $12 \text{ nm}$  from Photoluminescence and Transmission Electron Microscopy measurements (not presented here).

### 3.5 References

- [3.1] G. Lutz, *Silicon drift and pixel devices for x-ray imaging and spectroscopy*, JSR 13, 99 (2006).
- [3.2] T. Eggert, *Die spektrale Antwort von Silizium-Röntgendetektoren*, Ph. D. Thesis, Department of Physics, Technical University, Munich (2004).
- [3.3] T. Panzner, *Kohärente Reflexion mit weißer Synchrotronstrahlung im harten Röntgenbereich*, Ph.D. thesis, Department of Physics, University of Sigen (2007).
- [3.4] U. Pietsch, V. Holý, T. Baumbach, *High-resolution X-ray Scattering from Thin Films to Lateral Nanostructures*, Springer Verlag, ISBN 0387400923 (2004).
- [3.5] Holldack K, Feikes J and Peatman W B 2001 *Nucl. Instrum. Methods A* 467–468 235
- [3.6] T. Panzner, G. Gleber, T. Sant, W. Leitenberger, U. Pietsch, *Coherence experiments at the white-beam beamline of BESSYII*, Thin Solid Films 515, 5563-5567 (2007)
- [3.7] U. Pietsch, J. Grenzer, Th. Geue, F. Neissendorfer, G. Brezsesinski, Ch. Symietz, H. Möhwald, W. Gudat, *The energy-dispersive reflectometer at BESSY II: a challenge for thin film analysis*, Nucl. Instrum. Methods Phys. Res. A, 467/468, 1077-1080 (2001)

## Chapter 4

### Static speckle measurements from various test surfaces

This chapter discusses the details of coherent x-ray reflectivity measurements performed on various test surfaces at EDR beamline with white x-ray beam. At start it discusses the details of a typical measurement followed by measurements of coherent reflectivity from GaAs technologically flat surface and lateral periodic structure of GaAs surface grating. Coherent reflectivity measurements from thin Pt layer are discussed further. Due to the real space constraint of finite support region for faster convergence of phase retrieval algorithms, it is important to measure the coherent reflectivity from surface of spatially confined samples. The chapter finally discusses coherent reflectivity measurements on spatially confined Si wafer and GaAs surface gratings.

#### 4.1 Typical measurement

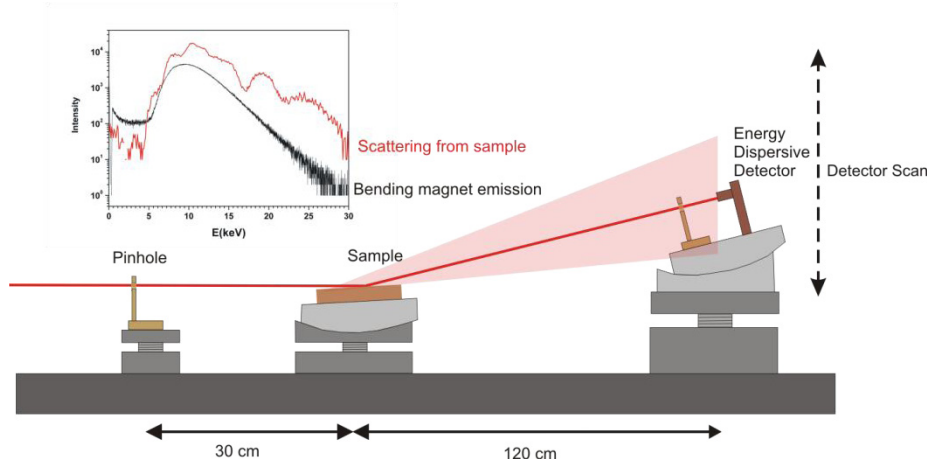


Fig .4.1 Measurement set up

For a typical coherent reflectivity measurement, sample surface is illuminated by white x-ray beam at grazing incidence. Pinhole of typical size  $10\ \mu\text{m}$  or  $15\ \mu\text{m}$  (transverse coherence lengths  $\xi_v \sim 53\ \mu\text{m}$ ,  $\xi_h \sim 43\ \mu\text{m}$  for 8 keV x-rays at  $\sim 31\ \text{m}$  from the source) is placed before the sample at a typical distance of 30 cm. This ensures that the incoming beam striking the sample is almost fully coherent between 5 keV and 25 keV. Specular and nonspecular scattering is measured with the help of energy dispersive point detector placed at a typical

distance of 1.2 m. The detector opening is spatially confined by a pinhole of size 10  $\mu\text{m}$  for getting good spatial resolution to resolve speckle pattern from the surface.

The EDR beamline is not exclusively designed for experiments with coherent x-rays. It is basically designed for x-ray diffraction or reflectivity experiments [4.1, 4.2]. With the apparatus available for performing these experiments with incoherent x-rays the precision required to perform coherent x-ray experiments is rather hard to achieve.

To align the detector with 10  $\mu\text{m}$  opening in the direction of spatially confined 10  $\mu\text{m}$  x-ray beam is the first essential part of the preparation. The alignment of the sample in horizontal plane and its center of rotation with the center of rotation of the angular motors (goniometers) are the next important steps. The stepper motors by HUBER play useful role in this respect. Although, the thermal drift in the motor movement cannot be completely eliminated.

The experimental table is placed in a closed radiation protected hutch but the internal environment possesses thermal fluctuation of fraction of degrees. The local heating of the sample by x-ray beam may contribute to the expansion of the sample depending on the thermal expansion coefficient of the sample material. This ultimately results in the movement of specularly reflected beam and the whole misalignment in the reciprocal space.

Thus the measurement with the expected location of the specular beam by considering the previous alignment might fall in some different region in reciprocal space. Considering all these factors the proper arrangement of the set up and all the alignments before the actual measurement is critical and time consuming.

The scattering from the surface of a sample is relatively strong at grazing incidence close to the critical angle (maximum at the critical angle) compared to the scattering at higher incident angles. With this set up it is possible to measure the nonspecular scattering almost 1.5 mm above and 1.5 mm below the specularly reflected beam, in the detector plane with reasonable statistics. This corresponds to  $\Delta\alpha_{f,max} = \pm 0.071^\circ$  at a typical sample-detector distance of 1.2 m. The detector is moved vertically in step size of 2  $\mu\text{m}$  and energy spectrum is measured at each position.

It should be noted here that the angle of incidence is fixed, thus the position of the sample in the incoming beam is not altered while performing the scan. Effectively the illuminated area on the sample, footprint, is constant throughout the complete scan. This assures that the whole measurement is related to the area on the sample corresponding to the footprint region only.



As discussed in section 3.1 the detector can measure with linear response up to count rate of  $10^5$ . Due to this limitation the scattering at and near the specular beam is measured in a set of various scans each with different thicknesses of the Al absorbing plates. The consecutive scans are measured with some overlap so as to have smooth continuation after normalization. The overlap also gives the possibility of recalibrating minor misalignment in the consecutive scans. When combined, the collective scan contains more than 1000 energy spectra corresponding to each vertical step of the detector. Each spectrum is measured for 10 sec and 2.5 sec are needed to transfer the data to the data acquisition computer.

As the energy spectra are measured with different Al absorbers, each spectrum is normalized by the calculated incident spectrum (Fig. 3.5) with corresponding thickness of Al plate and path of the x-ray beam in air. The consecutive scans are connected to get an intensity map and the intensities are corrected according to the overlap region as a reference so that the continuation from one scan to the next is smooth.

Due to this procedure the absolute intensities are lost but the measurement of absolute intensities is possible only with the detector with high dynamic range than the present one. The lack of absolute intensities is not a major problem as the relative intensities still possess the same contrast.

The map in energy-detector position  $I(E, z)$  space or energy-exit angle  $I(E, \Delta\alpha_f)$  space is converted to the scans in reciprocal space vector  $I(q_x, q_z)$  space, using the equations (3.10) and (3.11) as follows:

$$q_x = \frac{2\pi E}{12.398} (\cos \alpha_f - \cos \alpha_i) \quad (4.1)$$

$$q_z = \frac{2\pi E}{12.398} (\sin \alpha_f + \sin \alpha_i) \quad (4.2)$$

with energy (E) expressed in keV and the reciprocal space vectors  $q_x, q_z$  in  $\text{\AA}^{-1}$ . The in-plane angle  $\varphi$  for the measurement is 0.

## 4.2 Flat surface as a reflecting mirror

As discussed in section 3.3, it is not possible to use a guard pinhole to block second or higher order fringes of pinhole diffraction pattern to fall on the sample. Rather the complete diffraction pattern at the pinhole for all the energies of the incoming beam is incident on the sample. At incident angles below the critical angle it is expected that this diffraction pattern will get completely reflected from a flat surface. In other words a flat surface is expected to act like only a reflecting mirror for the pinhole diffraction pattern as shown in Fig. 4.2.

Diffraction at the entrance pinhole reflected from a smooth surface can be calculated by considering a “virtual” pinhole is situated along the outgoing beam direction backwards. It is discussed in section 5.1 in details. The calculated diffraction pattern (Fig. 5.2 (A)) at this “virtual” pinhole with detector plane making an angle of  $90 - 2\alpha_i$  is the pinhole diffraction pattern reflected from a smooth surface.

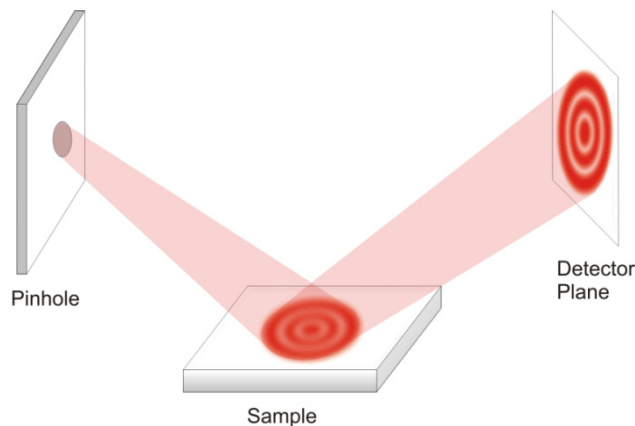


Fig. 4.2 Schematic of reflected image of pinhole diffraction from a smooth surface

With this expectation technologically smooth a GaAs (100) wafer is selected as a trivial sample. GaAs has critical angle of incidence of  $0.3^\circ$  at 8 keV. The wafer is illuminated at grazing incidence angle of  $0.204^\circ$ .

The measured  $I(E, z)$  map is shown in Fig. 4.3. This shows strong specularly reflected beam at detector position of 8.49 mm. Due to the use of Al absorbers of various thicknesses near the specular beam (See Fig. 4.3(B)), the information for lower energies, almost below 8 keV, is suppressed. The intensities in this region near specular beam at lower energies are higher only due to the normalization by exponentially increasing the incident energy spectrum at these energies. Off-specular scattering is irregularly spaced and the features are wider at lower energies and become narrower at higher energies continuously.

The scattered intensity is very weak at higher energies, almost above 15 keV, due to the exponentially decaying nature of the emission spectrum of the bending magnet. So as to make it independent of energy and detector position the intensity map is plotted in reciprocal space, as in Fig. 4.4. The  $I(q_x, q_z)$  map shows series of maxima lines parallel to  $q_z$  axis.

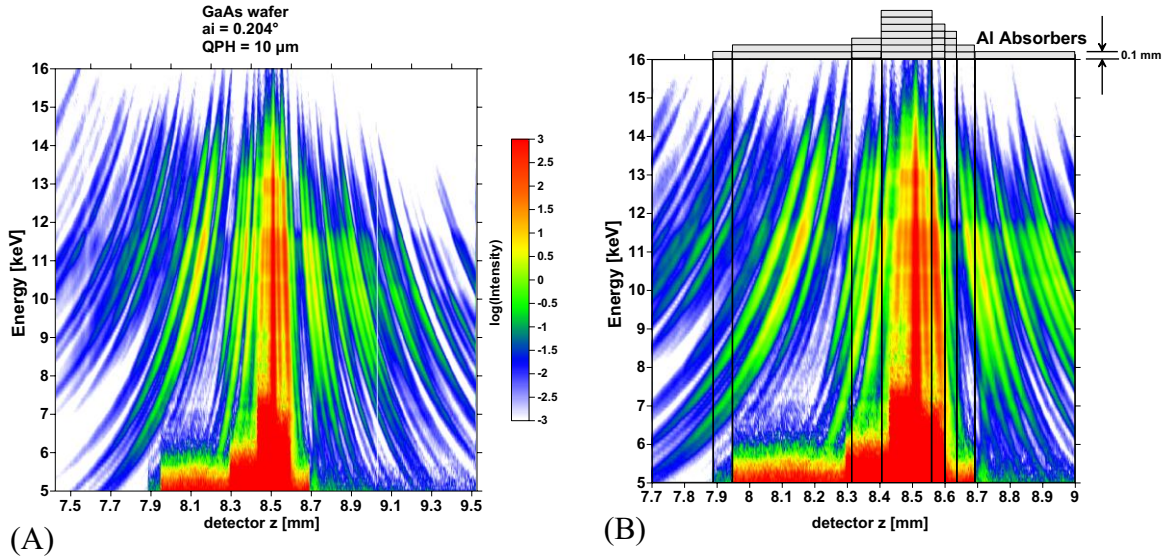


Fig. 4.3 Measured intensity map for (A) GaAs wafer (B) indicating Al absorbers

This map is similar to a reciprocal space map one would have obtained from a series of  $I(\alpha_i, (\alpha_i + \alpha_f))$  scans using a monochromatic x-ray beam. The sample is kept at different values of angle of incidence  $\alpha_i$  and at such position intensity is recorded as a function of  $(\alpha_i + \alpha_f)$ . Depending on the value of  $\alpha_i$  the illuminated area on the sample is larger or smaller.

The recorded information with  $I(\alpha_i, (\alpha_i + \alpha_f))$  scan in case of monochromatic source does not originate from a unique area on the sample surface. This is not the case for energy dispersive set up. The footprint on the sample is always the same and thus recorded information originates from a unique area on the sample.

The spectral distribution of the maxima lines is not regular. Figure 4.4 (B) shows the slices of the map (Fig. 4.4(A)) at different  $q_z$  values. It is clear from these slices that the observed coherent scattering possesses randomly distributed intensity and width of the peaks. Hence the scattering pattern can be called to be “speckled” as discussed in section 2.4.

The measured scattering data from the surface is not mere a reflected image of the illumination function from the sample. The latter one (Fig. 5.2(A)) consists of regularly

spaced fringes with gradually decreasing intensity away from the specular beam. The regularly spaced oscillations in the calculated pattern (Fig. 5.2(B)) are  $\sim 10$  times rapid than the oscillations in the measured pattern. The calculated pattern decays rapidly along  $q_x$  direction (more than  $10^{-6}$  of dynamic range). Whereas the measurement shows that there is still measurable intensity at higher  $q_x$  values away from the specular beam. The reflection of illumination function from a perfectly flat surface with zero roughness is discussed in details in Ph.D. thesis of T. Panzner [4.3].

The reflected image of the illumination function would appear only in case of reflection from an exactly smooth surface with zero roughness. This cannot be realized even for the best material. Height fluctuations of single atomic steps are in the order of probing wavelength and thus are responsible for spatial variation of the phase.

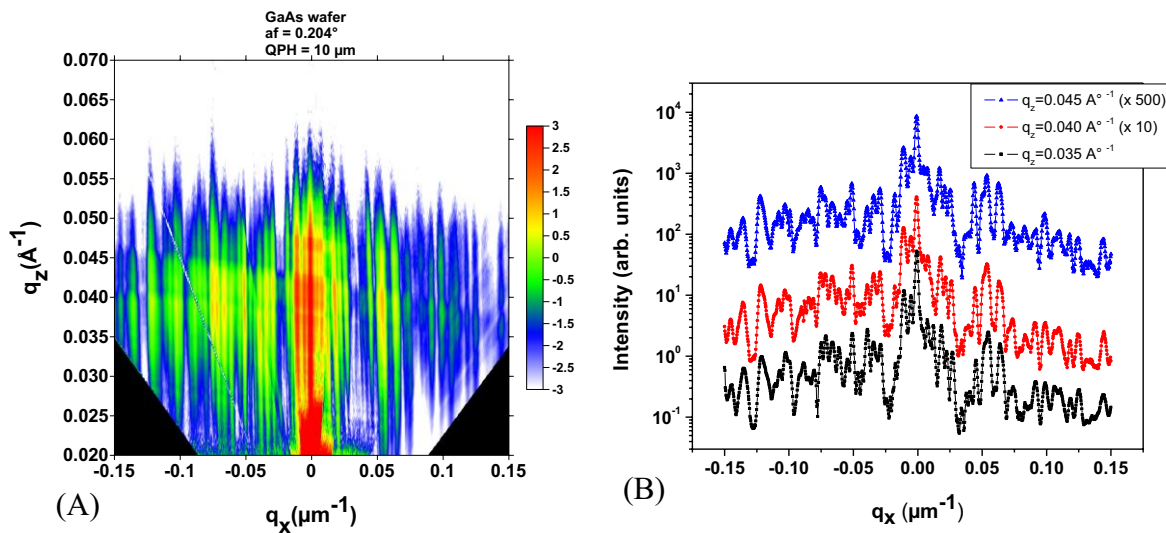


Fig 4.4 (A) Reciprocal space map of GaAs wafer  
(B) Slices for measurement map (Fig. 4.4(A)) at different  $q_z$  values

There is a strong contribution from the sample surface scattering. Even though the surface is technologically smooth, there exists certain nonzero roughness. The surface height distribution need not be constant throughout the sample surface. The regions of maxima and minima arise due to the constructive and destructive interference of the scattered waves from the different parts of the surface which have different local height.

### 4.3 Lateral periodic surface

Periodic distribution of surface height of the sample can yield some periodicity in the randomly distributed intensity pattern as observed in Fig. 4.4. Bearing this idea in mind, measurements are performed on lateral periodic surfaces. Surface grating on GaAs with nominal lateral period of 500 nm and depth of about 10 nm are chosen as a sample.

At first the sample surface is examined under Atomic Force Microscope (AFM). Figure 4.5 shows the AFM image of GaAs surface grating at different positions on the surface. The shape of the gratings is almost trapezoidal. The average period of the gratings comes out to be  $D_0 \sim 620$  nm. But the depth at the troughs is not constant over the whole surface and the height at the crests is also not uniform at different positions on the surface.

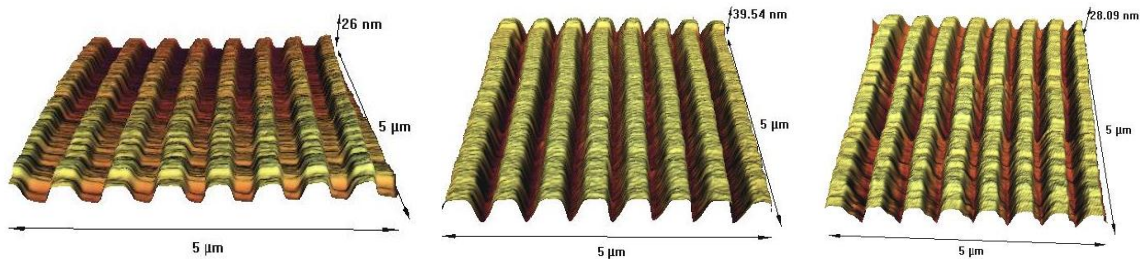


Fig. 4.5 AFM images of GaAs surface gratings at different positions on the surface.

The sample was examined with incoherent monochromatic x-rays at an in-house facility. Cu  $K_{\alpha}$  8 keV x-ray radiation is used and the specular and nonspecular scattering is measured at high resolution diffractometer of GE.

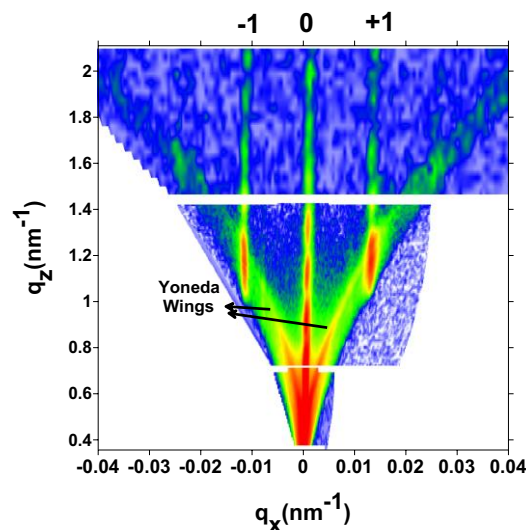


Fig. 4.6 Reciprocal space measurement for GaAs surface grating with 8 keV x-rays

The first order peaks due to grating lateral period can be seen at  $q_x = \pm 0.0125 \text{ nm}^{-1}$ . The second and higher order peaks are hardly visible. The grating period comes out to be  $2\pi/q_x = 502 \text{ nm}$ , which is less as compared to the grating period measured with the help of AFM. Oscillations can also be seen along  $q_z$  at the specular beam as well as at both the first order peaks (Fig. 4.6). These oscillations indicate presence of some buried layer under the surface of the gratings. The oscillations at the first order peaks are out of phase of the corresponding oscillation at the specular beam beyond  $q_z = 1.2 \text{ nm}^{-1}$ . These oscillations have periodicity of  $\Delta q_z = 0.15 \text{ nm}^{-1}$ , which corresponds to real space periodicity of  $2\pi/\Delta q_z = 41 \text{ nm}$ .

At EDR beamline, the maximum inspected detector position z-range of  $\pm 1 \text{ mm}$  or the exit angle range of  $\Delta\alpha_f = \pm 0.047^\circ$  corresponds to the maximum lateral momentum transfer of  $q_{x,max} = \pm 0.15 \mu\text{m}^{-1} = \pm 0.15 \times 10^{-3} \text{ nm}^{-1}$  for the angle of incidence of  $0.2^\circ$ .  $q_{x,max}$  can be increased by inspecting larger detector z-range but signal is too weak for detector z-position more than  $\pm 1.5 \text{ mm}$ . The maximum achievable value of lateral momentum transfer at this detector position is  $q_{x,max} = \pm 0.20 = \pm 0.20 \times 10^{-3} \text{ nm}^{-1}$ . Hence the peaks due to grating period observed at  $q_x = \pm 0.0125 \text{ nm}^{-1}$  (Fig. 4.6) are not be accessible in this inspected detector z-range. Nevertheless, the position of peaks due to grating period depends on the orientation of grating lines along the beam direction. For the grating lines along the direction making an azimuthal angle of  $\phi$ , the peaks due to grating are expected at  $\Delta q_x = 2\pi/D$ , where  $D = D_0/\sin\phi$  is the projection of  $D_0$  to the incident beam direction. By keeping the sample at  $\phi = 0.75^\circ$ , the effective period of the grating was  $D \sim 47 \mu\text{m}$ . The grating peaks were expected at  $\Delta q_x = 0.21 \mu\text{m}^{-1}$ . The vertical transverse coherence length at 31 m from the source for 8 keV is  $\sim 50 \mu\text{m}$  and the incoming beam is spatially confined by  $10 \mu\text{m}$  entrance pinhole. But for the sample at grazing incidence angle of  $0.1^\circ$ , the entire footprint region of width  $10 \mu\text{m}/\sin(0.1^\circ) \sim 5730 \mu\text{m}$  is irradiated by coherent x-rays. For the orientation of the grating lines with  $\phi = 0.75^\circ$ ,  $5730 \mu\text{m}/47 \mu\text{m} \sim 122$  grating lines are coherently irradiated. Fig. 4.8 (B) shows the reciprocal map of the coherent scattering for this particular orientation of the grating sample at incident angle of  $0.1^\circ$ , with  $10 \mu\text{m}$  entrance pinhole.

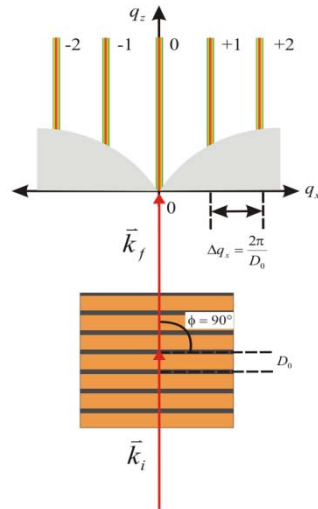
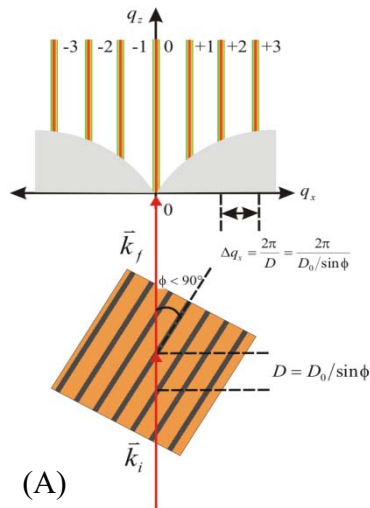
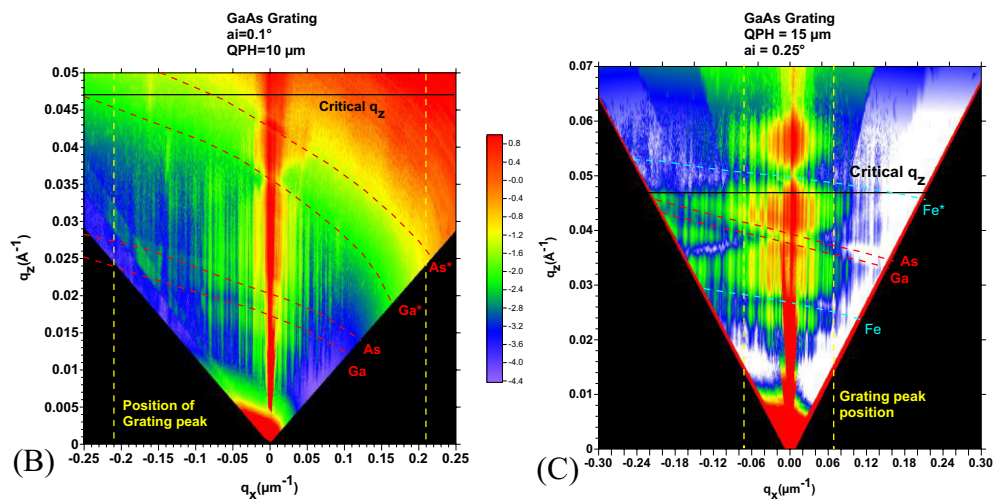


Fig. 4.7 Orientation of grating with grating lines perpendicular to direction of incident beam



(A)



(B)

(C)

Fig. 4.8 (A) Orientation of grating with grating line making certain angle  $\phi$  with the direction of incident beam  
 (B) Reciprocal space map of GaAs surface gratings oriented at  $\phi = 0.75^\circ$  at incident angle of  $\alpha_i = 0.1^\circ$   
 (C) Reciprocal space map of GaAs surface gratings oriented at  $\phi = 0.40^\circ$  at  $\alpha_i = 0.25^\circ$

The first order grating peaks are hardly visible at expected positions  $q_x = 0.21 \mu m^{-1}$ . The absence of distinct grating peaks might be due to the nonuniform height of the grating crests and nonuniform depths of grating troughs, as seen in Fig. 4.5. The effect of this nonuniformity is still enhanced when the grating lines are aligned making very small azimuthal angle of  $\phi = 0.75^\circ$  for Fig. 4.8 (B) or  $\phi = 0.4^\circ$  for Fig. 4.8 (C).

Apart from this, it exhibits again a series of lines parallel to  $q_z$  axis as observed in case of GaAs plain wafer (Fig. 4.4(A)). The spatial distribution of these lines is again not regular. The curved dotted red lines going across the whole map mark the K-absorption lines (Ga, As) for gallium and arsenic at 10.367 keV and 11.867 keV respectively and their respective pile ups (Ga\*,As\*). With the critical value for the vertical momentum transfer  $q_{z,c} = 0.047 \text{ \AA}^{-1}$ , it was expected that the peaks due to grating periodicity will be strongly visible above this value of  $q_{z,c}$ . The measured reciprocal space map in Fig. 4.8 (B) shows the situation of total external reflection ( $< q_{z,c}$ ).

The reciprocal map in Fig. 4.8 (C) shows the measurement of scattering for the same sample but at higher angle of incidence of  $0.25^\circ$ . The entrance pinhole of  $15 \mu m$  was used this time so as to get higher coherent flux on the sample. The grating lines were oriented making an angle of  $\phi = 0.4^\circ$  with the incident beam direction, which gives the effective period of grating as  $D \sim 90 \mu m$ . With the footprint of  $15 \mu m / \sin(0.25^\circ) \sim 3440 \mu m$ , the number of grating lines coherently irradiated is  $3440 \mu m / 90 \mu m \sim 38$ .

The grating peaks are hard to distinguish amongst the irregularly spaced vertical scattering lines, even above  $q_{z,c}$ . The map exhibits discontinuity due to K- absorption for Ga and As (dotted lines in Red), similar to the measurement in Fig. (4.8(B)). It also shows the sample is contaminated with the traces of iron due to the presence of the K- absorption line for Fe at 7.112 keV (dotted line in Cyan) and its pile up (Fe\*).

#### 4.4 Pt thin layer on Glass

Coherent reflectivity from thin layer of Pt on glass is measured at different angles of incidence of  $0.20^\circ$ ,  $0.35^\circ$  and  $0.50^\circ$ . Due to different penetration depths at different incident angles  $\alpha_i = 0.35^\circ$ ,  $0.50^\circ$  the measured scattering intensity corresponds to different depths inside the thin film. Thus, it gives access to information from interface between Pt layer and



glass substrate. For  $\alpha_i = 0.20^\circ$  the x-rays are sensitive only to the surface as  $\alpha_i < \alpha_c$  in this case. Fig. 4.9 and Fig. 4.10 displays the reciprocal maps. The maps exhibit similar features as observed in case of previous samples. Series of irregularly spaced lines parallel to  $q_z$  axis can

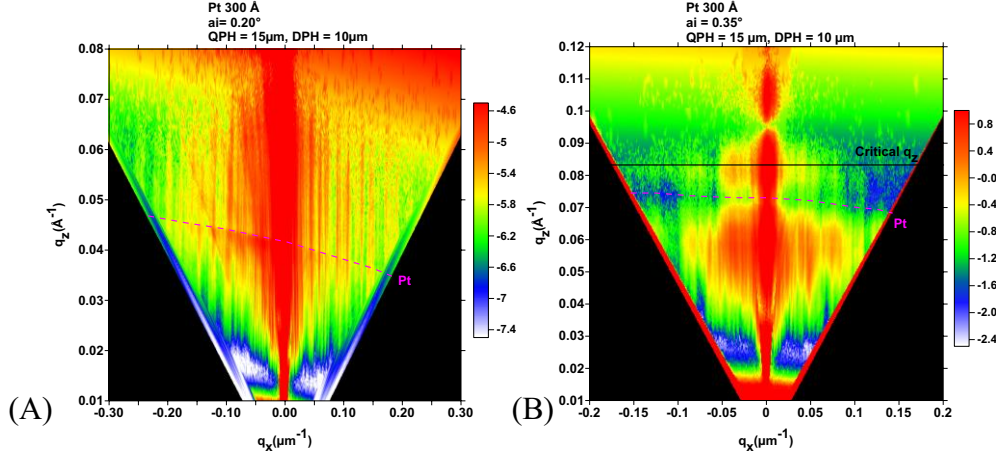


Fig. 4.9 Reciprocal space measurement of Pt thin film at (A)  $\alpha_i = 0.20^\circ$  (B)  $\alpha_i = 0.35^\circ$

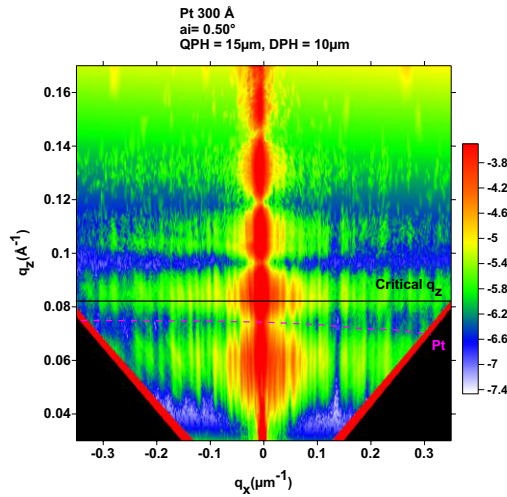


Fig. 4.10 Reciprocal space measurement of Pt thin film at  $\alpha_i = 0.50^\circ$

be observed. The maps exhibit L-absorption line for Pt at 11.564 keV. The oscillations along  $q_z$  for  $q_z > q_{z,c}$  correspond to thickness oscillations of the Pt layer. These can be observed for higher angles of incidence of  $0.35^\circ$  and  $0.50^\circ$ . These oscillations are present at specular as well as off-specular positions. The critical value of vertical momentum transfer for Pt is  $q_{z,c} = 0.082 \text{ \AA}^{-1}$ . The distribution of maximum lines at specular and off-specular regions below and above  $q_{z,c} = 0.082 \text{ \AA}^{-1}$  is qualitatively similar.

Fig. 4.11 shows the slices to the reciprocal space maps at  $\alpha_i = 0.35^\circ$  and  $0.50^\circ$  along  $q_z$  axis. The measured  $q_z -$  scans are fitted with the calculated intensity pattern using reflectivity tool

Parratt32 [4.4]. The thickness of the film comes out to be 200 Å with the mean roughness  $\sim$  10 nm.

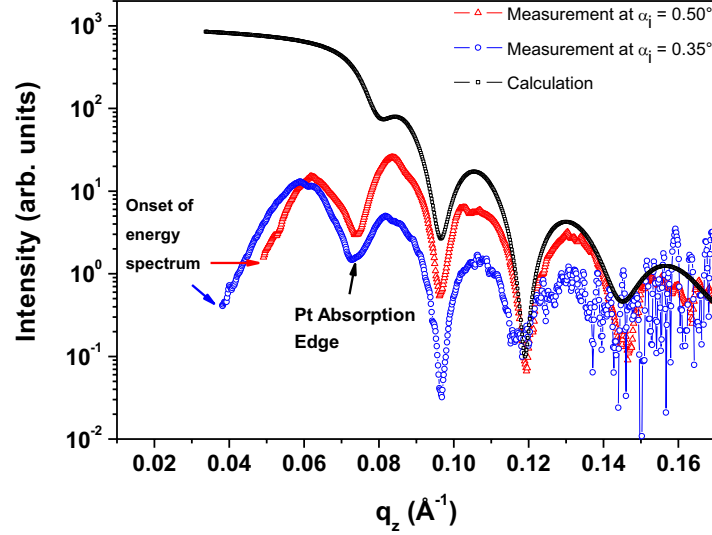


Fig. 4.11 Slices to the measured reciprocal space maps at 0.35°, 0.50° along  $q_z$  and the calculated fit using Parratt32 [4.4]

## 4.5 Spatially confined Si wafer

As discussed in section 2.6, the object is comprised of a nonzero density region, support (S), surrounded by zero density region. This is a useful real space constraint necessary for faster convergence of phase retrieval algorithms. In case of coherent reflectivity experiments although the incoming x-ray beam is spatially confined by a pinhole, the footprint of the beam decides the illuminated area on the sample. For a typical pinhole of size  $d_p = 10 \mu\text{m}$  and sample kept at angle of incidence  $\alpha_i = 0.2^\circ$ , the footprint on the sample is  $l = d_p / \sin\alpha_i = 2.86 \text{ mm}$  along the incident beam direction. All the samples discussed in previous sections have width larger than the footprint of the beam. Hence the real space constraint of finite support region is not satisfied.

Experiments are performed on technologically flat Si wafer but triangular in shape. It is illuminated by x-ray beam at different positions on the sample at an angle of incidence of  $0.2^\circ$ . Starting with the footprint within the sample width, like the previous measurements, successively the sample is translated in the beam so that the footprint covers shorter width of the sample. For the case where the footprint covers the sample width of 0.8 mm the finite

support region constraint is fulfilled. Here the support region is about 28 % of the footprint region, which is still smaller than the maximum of 50 % required for faster convergence of phase retrieval algorithms [4.5].

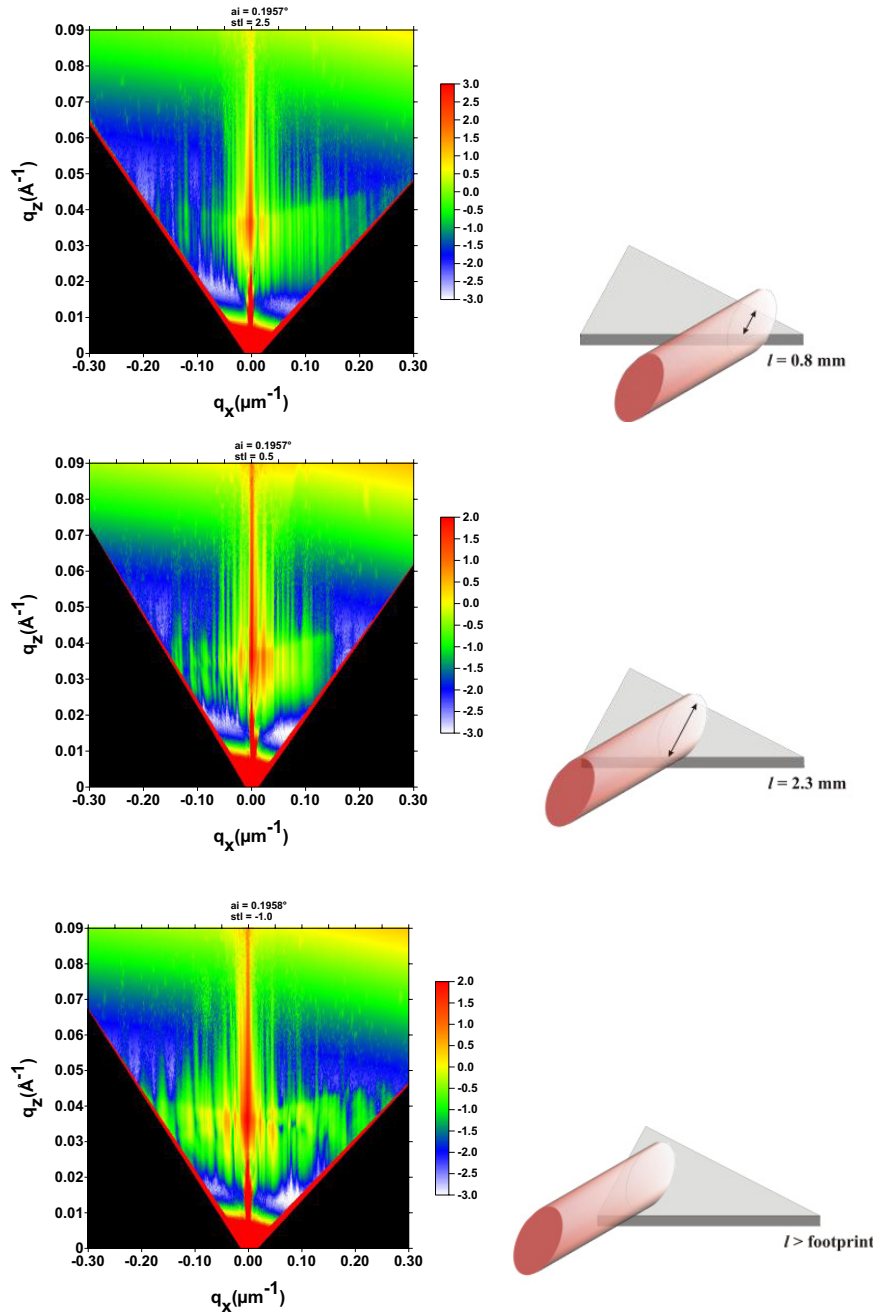


Fig. 4.12 Reciprocal space maps of triangular shaped Si wafer at different positions on the sample

The reciprocal space maps (Fig. 4.12) at different positions contain similar set of maximum lines parallel to  $q_z$  axis like observed for previous measurements. The distribution of these lines differs from position to position. This indicates that the scattered intensity distribution depends on the local surface height distribution of the sample.

This can be well observed in Fig. 4.13 for slices at  $q_z = 0.035 \text{ \AA}^{-1}$  at different positions on the sample. For the case with effective sample width of  $l = 0.8 \text{ mm}$ , the scattering is calculated from the slit of size  $0.8 \text{ mm}$ . Many peaks of the calculated slit scattering coincide with the peaks in measured scattering intensity profile especially in the region of  $q_x < 0$ . The corresponding peaks are missing for other two measurements. Also the widths of the calculated peaks look qualitatively the same as those of the measured ones. This implies that the width of the sample plays important role in the coherent reflectivity from the sample surface. The scattered intensity does not decrease gradually with  $q_x$  as the calculated slit scattering. The distribution in intensity at peaks is random and the widths of peaks also

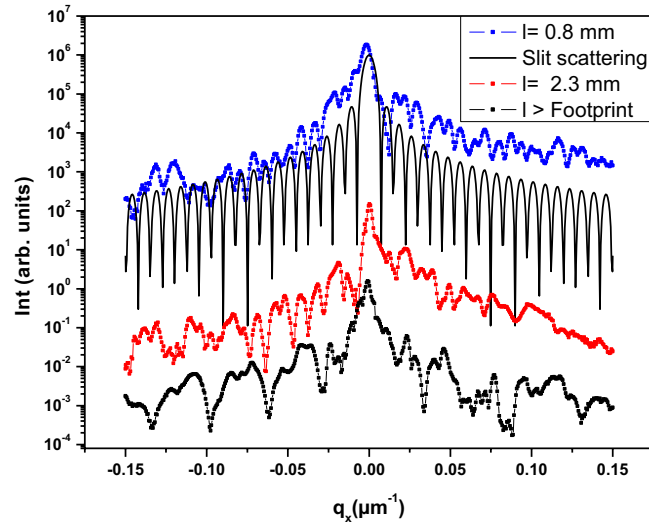


Fig. 4.13 Measured scattering amplitude at different position on the sample

differ. This originates from the contribution of height distribution from the length scales smaller than  $l$ . This is also evident from the scattering measured at two other sample positions. The oscillations measured at these positions are much wider than those for  $l = 0.8 \text{ mm}$ . The calculation of detailed height distribution is discussed in chapter 6.

## 4.6 Spatially confined GaAs grating

Coherent reflectivity is measured from spatially confined sample of lateral periodic surface of GaAs grating as in section 4.3. The width of the sample is confined to  $1.6 \text{ mm}$  perpendicular to the direction of grating lines. The sample is kept with grating lines making an azimuthal angle  $\phi = 0.5^\circ$  with the incident beam direction. Initially the sample was illuminated with

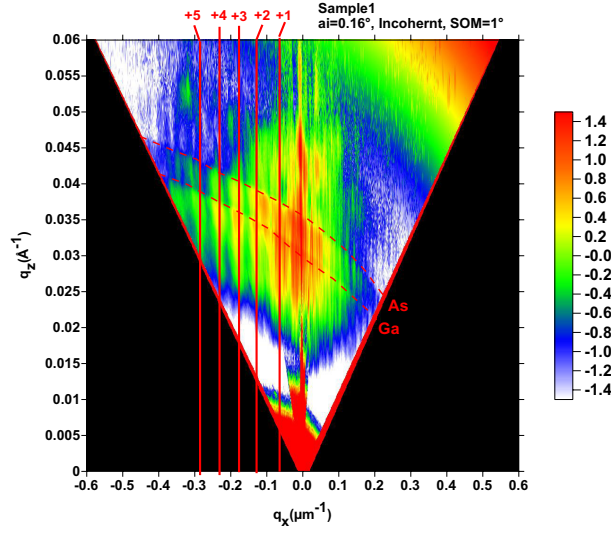


Fig. 4.14 Reciprocal space map of spatially confined GaAs grating with partially coherent beam ( $200 \mu\text{m} \times 200 \mu\text{m}$ ) at  $\alpha_i = 0.16^\circ$

x-ray beam of size  $200 \mu\text{m} \times 200 \mu\text{m}$ . This size of the beam is larger than the vertical and horizontal transverse coherence lengths ( $\xi_v \sim 53 \mu\text{m}$ ,  $\xi_h \sim 43 \mu\text{m}$  for 8 keV x-rays at  $\sim 31 \text{ m}$  from the source) at the EDR beamline. But the projected transverse coherence length in vertical direction at the sample position at shallow angle of incidence of  $\alpha_i = 0.16^\circ$  is  $\xi_v / \sin \alpha_i = 18.9 \text{ mm}$ . This is much larger than the width of the sample (1.6 mm). Hence the sample can be supposed to be under coherent illumination.

The peaks due to grating period (marked with vertical red lines) can be clearly seen at  $q_x = 0.063, 0.127, 0.175, 0.230, 0.284 \mu\text{m}^{-1}$  in reciprocal space map (Fig. 4.14) in the region  $q_x < 0$ . From the spacing between the grating peaks, the effective period of the grating comes out to be  $2\pi / \Delta q_x \sim 2\pi / 0.062 = 100 \mu\text{m}$ . The other scattering maximum lines parallel to  $q_z$  axis can be seen, which are observed in all the previous coherent reflectivity measurements (sections 4.2 - 4.5). The grating peaks are hard to identify in the region  $q_x > 0$ .

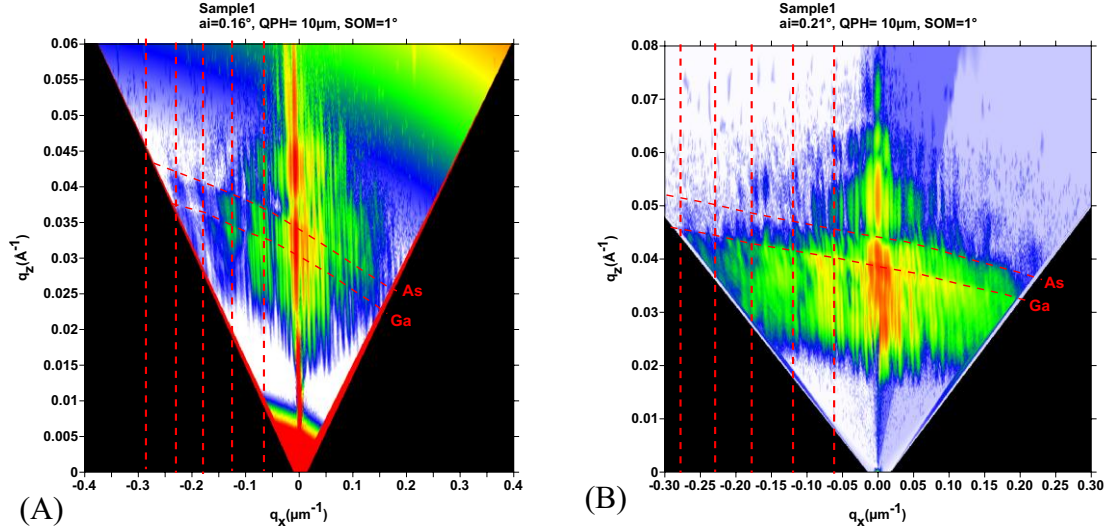


Fig. 4.15 Reciprocal space maps of spatially confined GaAs grating with coherent beam (A) at  $\alpha_i = 0.16^\circ$  and (B) at  $\alpha_i = 0.21^\circ$

Further for the measurement of coherent reflectivity, the sample was illuminated at different angles of incidence,  $\alpha_i = 0.16^\circ$  and  $0.21^\circ$ . For  $10\ \mu\text{m}$  entrance pinhole the footprint on the sample is  $3.58\ \text{mm}$  and  $2.72\ \text{mm}$  at  $\alpha_i = 0.16^\circ$  and  $0.21^\circ$  respectively. The nature of the reciprocal space map looks qualitatively similar to earlier coherent reflectivity measurement maps (sections 4.2 - 4.4). Here also the vertical maximum lines parallel to  $q_z$  axis can be observed. The spatial distribution of these lines is random also in this case. Dashed vertical red lines indicate the expected positions of the grating peaks which are observed in case of partially coherent case (Fig. 4.14). It is hard to identify the grating peaks amongst other vertical scattering lines. The discontinuity in the scattering along  $q_z$  direction is observed also in this case. There exists a weak minimum in the coherent reflectivity at  $q_z \approx 0.038\ \text{\AA}^{-1}$  at  $\alpha_i = 0.16^\circ$  (Fig. 4.15(A)). Minima are also observed in coherent reflectivity at  $q_z \approx 0.045, 0.058, 0.065\ \text{\AA}^{-1}$  at  $\alpha_i = 0.21^\circ$  (Fig. 4.15(B)).

## 4.7 References

- [4.1] U. Pietsch *et al.*, *The energy-dispersive reflectometer at BESSY II: a challenge for thin film analysis*, Nuclear Instruments and Methods in Physics Research A, 467–468, 1077–1080, (2001).
- [4.2] Y. Bodenthin *et al.*, *Temperature- and time-resolved X-ray scattering at thin organic films*, J. Synch. Rad., 9, 206-209, (2002).
- [4.3] T. Panzner, *Kohärente Reflexion mit weißer Synchrotronstrahlung im harten Röntgenbereich*, Ph.D. thesis, Department of Physics, University of Sigen (2007).
- [4.4] Reflectivity tool Parratte32,  
[http://www.hmi.de/bensc/instrumentation/instrumente/v6/refl/parratt\\_en.htm](http://www.hmi.de/bensc/instrumentation/instrumente/v6/refl/parratt_en.htm)
- [4.5] J. Miao, D. Sayre, H. N. Chapman, *Phase retrieval from the magnitude of the Fourier transforms of nonperiodic objects*, J. Opt. Soc. Am., 15, 1662-1669 (1998).

## Chapter 5

# Surface profile reconstruction from coherent x-ray reflectivity

After discussing the coherent reflectivity measurements in the last chapter, this chapter focuses on the theoretical explanation of the observed speckle patterns. The chapter starts with the calculations by considering the sample as a reflecting mirror. The diffraction pattern at the entrance pinhole reflected from a perfectly smooth surface is calculated. Here the contribution to the scattering from a surface is completely excluded. So as to consider the contribution from sample surface, the scattering amplitude is initially calculated based on the commonly used approach with detector in the far-field [5.1]. Calculations are performed by considering the sample surface to be made up of random arrangement of steps with different widths and different heights.

Due to the specific set up conditions at EDR beamline the far-field approximation is no more valid. The distance between the sample and the detector is never taken into account in the far-field approximation. Hence the theory based on Fresnel electron density [5.2] is been applied to explain the measurements. Here the physical electron density is multiplied by a complex phase factor which depends on the directions of the incident and scattered beams.

The results of direct calculation of speckle amplitude in far as well as near field are not satisfactory. It is seldom to get unique and converging solution of a surface profile from direct calculation of the speckle amplitude. Fourier based phase retrieval algorithms are widely used to retrieve electron density in coherent x-ray diffraction measurements in transmission. These algorithms are also applied in case of coherent reflectivity measurements in the far-field regime with monochromatic x-ray radiation. The next section of this chapter discusses the modifications performed in Gerchberg-Saxton (GS) algorithm to take into account the distance of detector from sample and also the second order terms in the phase from the sample. The algorithm is also modified to include the illumination function at the position of the sample. The modified algorithm is tested for a model surface.



## 5.1 Reflected image of illumination function from a flat surface

As discussed in section 4.2, the complete diffraction pattern at the entrance pinhole for all the energies of the incoming beam is incident on the sample. At incident angles below the critical angle it is expected that this diffraction pattern will get completely reflected from a flat surface. In other words a flat surface is expected to act like only a reflecting mirror which reflects the pinhole diffraction pattern as shown in Fig. 5.1. Diffraction at the entrance pinhole reflected from a smooth surface can be calculated by considering a “virtual” pinhole is situated along the outgoing beam direction backwards. The diffraction pattern (Fig. 5.2(A)) is calculated based on Lommel Formalism for Fresnel-Kirchhoff integral (section 3.3.1) with detector plane making an angle of  $90 - 2\alpha_i$ . This calculated pattern gives the pinhole diffraction reflected from a smooth surface.

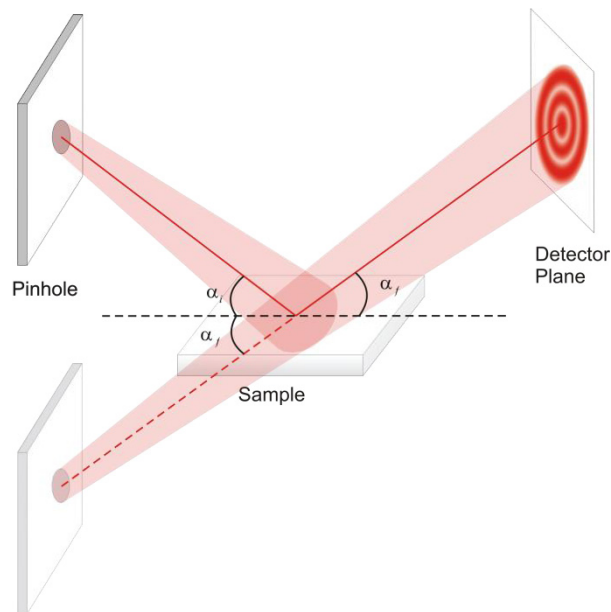


Fig 5.1 Smooth sample surface expected to act like a mirror

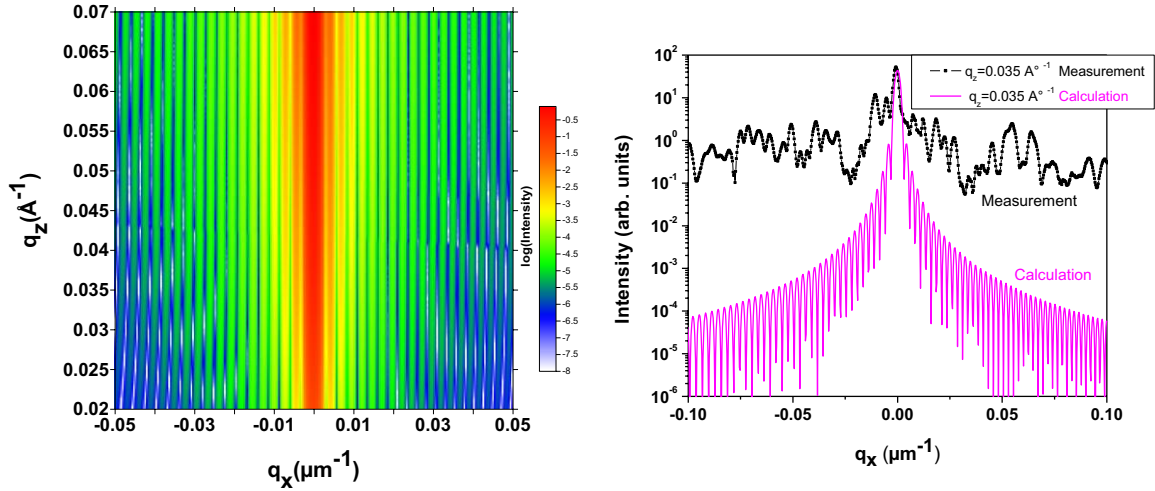


Fig 5.2 (A) Calculated reciprocal space map of reflection of the pinhole diffraction pattern  
 (B) Comparison of slice of measured map for GaAs flat surface (Fig.4.4(A)) and calculated map at  $q_z = 0.035 \text{ \AA}^{-1}$

Fig. 5.2(A) shows the calculated reciprocal space map for reflected pattern from a smooth surface at an angle of incidence of  $\alpha_i = 0.204^\circ$  at pinhole-detector distance of 1.425 m (pinhole-sample distance 0.230 m and sample-pinhole distance 1.195 m). It shows strong specular maximum line along with other maximum lines parallel to the  $q_z$  -axis with constant width and regular periodicity.

Although the contribution of sample surface scattering is not considered in this approach, the periodicity of the calculated scattering pattern is larger than that for the measurement (Fig. 5.2(B)). The local surface height can give additional contribution in the phase of the illumination function and can change the distribution of speckles observed in detector plane. But the width and the intensity of the peaks of the calculated pattern does not resemble those of the measured ones.

## 5.2 Single surface with random steps of different widths and different heights

It is hard to realize a perfectly smooth surface with zero roughness even with the state of the art manufacturing technology. It is realistic to consider a surface with certain nonzero roughness. The surface is considered to be comprised of facets with different widths and different heights. The distribution of widths and heights of the facets is considered to be completely random.

Calculations are performed for the experimental conditions of coherent reflectivity measurements from GaAs wafer as discussed in section 4.2.

Let us first consider the commonly used approach [5.4] is used to calculate the speckle amplitude by considering the detector in far-field. So as to test the formalism and to reduce the computing time, one dimensional case is considered.

The amplitude of scattered x-rays, or speckle amplitude, from a sample with surface described by function  $h(x)$  is given by

$$A(q) = \int_{-\infty}^{\infty} B(x) e^{iq_z h(x)} e^{iq_x x} dx \quad (5.1)$$

Thus the speckle amplitude is Fourier transform of the product of illumination function  $B(x)$  and the phase factor due to the height distribution function,

$$A(q) = \mathcal{F}(B(x) e^{iq_z h(x)}) \quad (5.2)$$

Now the surface is described by height function  $h(x)$  consisting of random widths  $d_j$  with random heights  $h_j$ . Calculations are performed by varying the widths and heights as parameters in different ranges. The calculated speckle intensity is compared with the measured intensity at  $q_z = 0.035 \text{ \AA}^{-1}$ .

The quality of the calculated fit can be expressed in terms of the quantity  $\chi^2$  expressed as

$$\chi^2 = \frac{\sum_j \{ \sqrt{I_{obs}(q_{x,j})} - |A(q_{x,j})| \}^2}{\sum_j I_{obs}(q_{x,j})} \quad (5.3)$$

The calculation is performed for several iterations with different distribution of the widths  $d_j$  and heights  $h_j$ . The quantity  $\chi^2$  is calculated for each iteration. The calculated intensity for minimum value of  $\chi^2$  can be considered as final result.

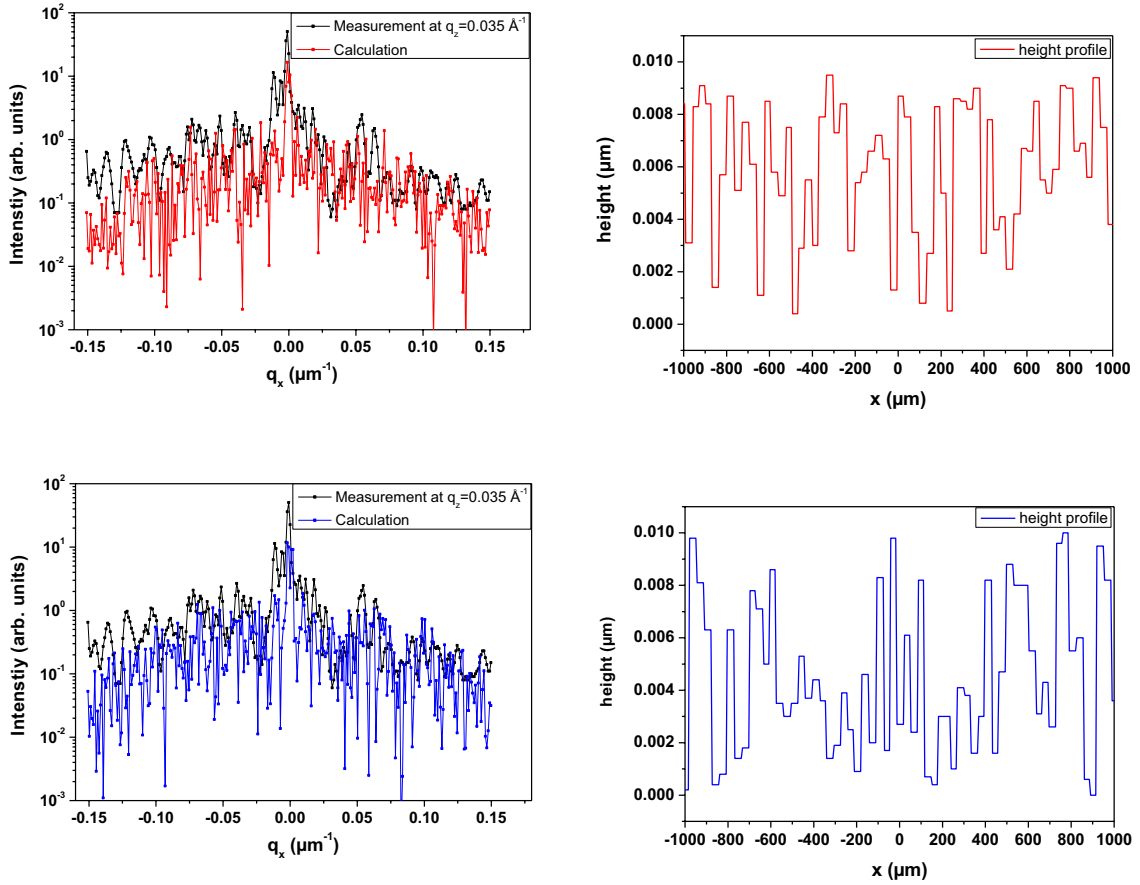


Fig. 5.3 Comparison of measurement for coherent reflectivity from GaAs wafer and two attempts (Red and Blue curve) of calculated speckle patterns (left) using equation (5.15) for a surface with random steps. The final result for surface height distribution function are plotted to the right of the figure.

The red and blue curves in Fig. 5.3 show the intensity for such calculation with widths  $5 < d_j < 7 \mu\text{m}$  and heights  $0 < h_j < 10 \text{ nm}$ . The inset shows the final result of height function. The minimum value of  $\chi^2$  achieved after 1000 iterations is 0.3352 for red curve and 0.3374 for blue curve. The minimum value of  $\chi^2$  is almost 0.33 for various repetitions of the calculation (not shown here). This value of  $\chi^2$  indicates that the fit of the calculated intensity pattern to the measured one is not good enough, also visible in Fig. 5.3 (left) from the red and blue curves of the calculated intensity. It is not realistic to consider variation in surface height of  $\sim 10 \text{ nm}$ .

The width of the central specular peak of the calculated pattern appears to match with that of the measured pattern. The widths of the smaller peaks of the calculated pattern appear in the same range as those of the measured speckle pattern. But the position and the intensity of the calculated peaks do not match with those of the measured pattern. Also the broader peaks in

the measurement cannot be calculated with this formalism. Moreover the solution is not unique, after each attempt one can get a different solution with almost the same value for the minimum of  $\chi^2$ .

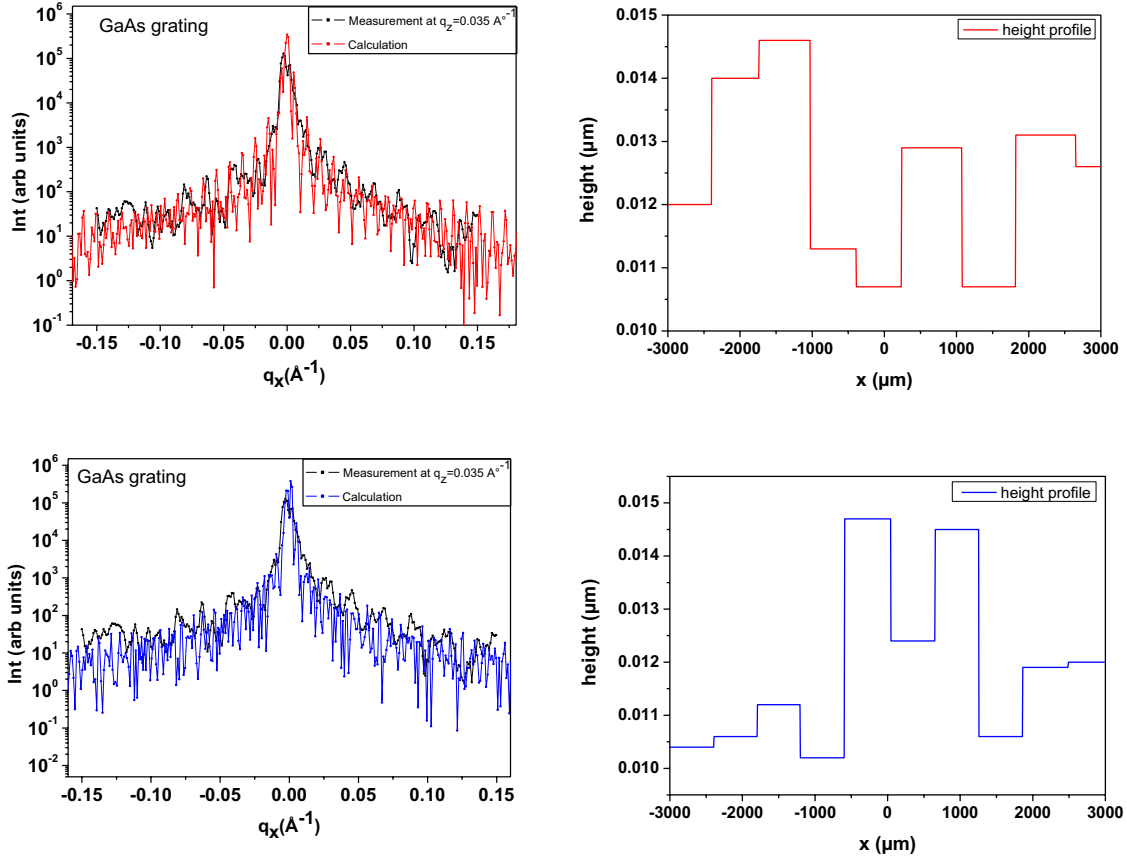


Fig. 5.4 Comparison of coherent reflectivity measurement from GaAs surface grating with two attempts (Red and Blue) of the calculated speckle pattern (left) using equation (5.15) for a surface with random steps. The final result of surface height distribution function are plotted to the right of the figure.

Similar calculations are performed and compared with the measurement (Fig. 5.4) of speckle pattern from GaAs surface gratings (section 4.3) at angle of incidence of  $0.1^\circ$ . The surface height function with random widths  $490 < d_j < 510 \mu\text{m}$  and random height  $0 < h_j < 10 \text{ nm}$  is considered and speckle intensity is calculated and compared with the measured for 1000 iterations. The minimum value of  $\chi^2$  for the red curve is 0.4699 and for the blue curve is 0.4664. The larger value of minimum of  $\chi^2$  is mainly because of the mismatch of the measured intensity and its fit near the specular position at  $q_x = 0$  where the intensities are high.

Here, again, the central specular peak for the calculation appears of the same width as that of the measured. Also the nonspecular peaks for the calculated pattern appear to be almost of the

same widths as those for the measured one. This calculation looks more realistic than the previous calculation in Fig. 5.2, although the minimum value of  $\chi^2$  is larger in this case than the previous. But like the previous calculation, the broader peaks cannot be simulated and the calculation is not unique.

### 5.3 Scattering amplitude in the near field based on Fresnel electron density

In the expression for the speckle amplitude according to equation (5.1) the detector is considered to be in the far field of the sample. This might not be the case always. Fresnel number ( $N$ ) decides the region for using Fresnel or Fraunhofer approximation for the diffraction amplitude [5.4]. It is defined as follows

$$N = \frac{a^2}{\lambda L} \quad (5.4)$$

where  $a$  is the size of the aperture and  $L$  is the distance from source to observation plane. For  $N \geq 1$ , it is required to use the Fresnel approximation but for  $N \ll 1$  Fraunhofer approximation works well.

For the typical distances at set up of the EDR beamline (see Fig. 4.1), the Fresnel number is plotted for the measurable energy range of  $5 < E < 40 \text{ keV}$  in Fig. 5.5. For pinhole-sample arrangement, with size of the aperture  $a$  as the size of pinhole =  $10 \mu\text{m}$ , the Fresnel number is  $> 1$  for the measurable energies and is  $\sim 10$  for  $40 \text{ keV}$  (Fig. 5.5(A)). Thus the sample is in the Fresnel region of the entrance pinhole, which is also clear from the diffraction pattern of the entrance pinhole measured at the sample position [5.5].

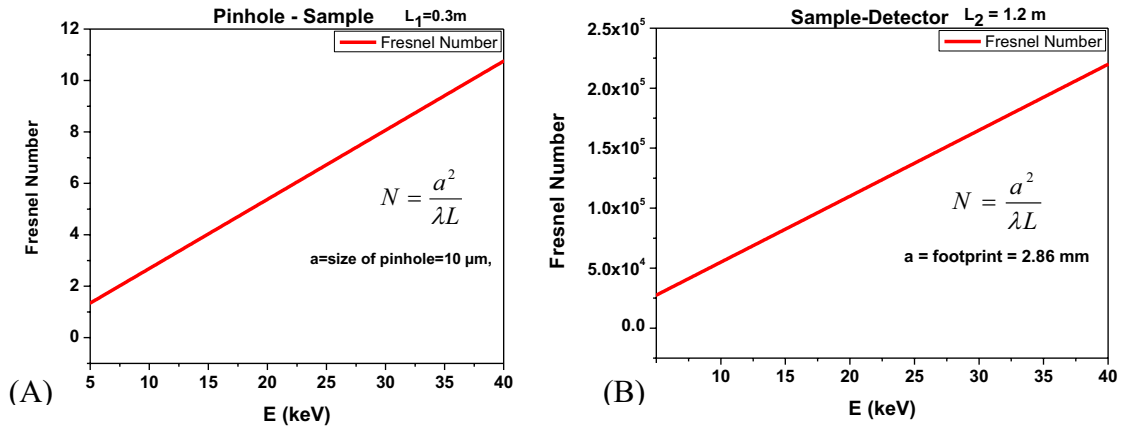


Fig. 5.5 Fresnel number versus energy for (A) pinhole - sample arrangement  
(B) sample - detector arrangement

For the arrangement of sample – detector, the footprint at the sample position for  $10\ \mu\text{m}$  pinhole at  $\alpha_i = 0.2^\circ$  is considered as the size of the aperture  $a$ . At a typical distance of 1.2 m from the sample the Fresnel number at the detector position is in the range  $10^4 - 10^5$  for the measurable energies (Fig. 5.5 (B)). This justifies the use of Fresnel approximation in calculating the scattered amplitude from the sample surface and hence it is important to retain the second order terms in the phase contribution from the sample.

### 5.3.1 The formalism based on the Fresnel electron density

The scattered amplitude should be calculated by considering the propagation of mutual coherence function from source to detector via the sample. The complete discussion can be found in the reference [5.2]. Following is a short discussion on these calculations based on Hygens-Fresnel principle in the kinematic range of the scattering i.e. without any multiple scattering from the sample.

A set up is illustrated in Fig. 5.6 schematically. The beam emerges from an aperture  $A$  with its plane normal to the mean direction of the beam. The distance between the center of the aperture  $A$  and center of the sample  $S$  is  $L_1$ .

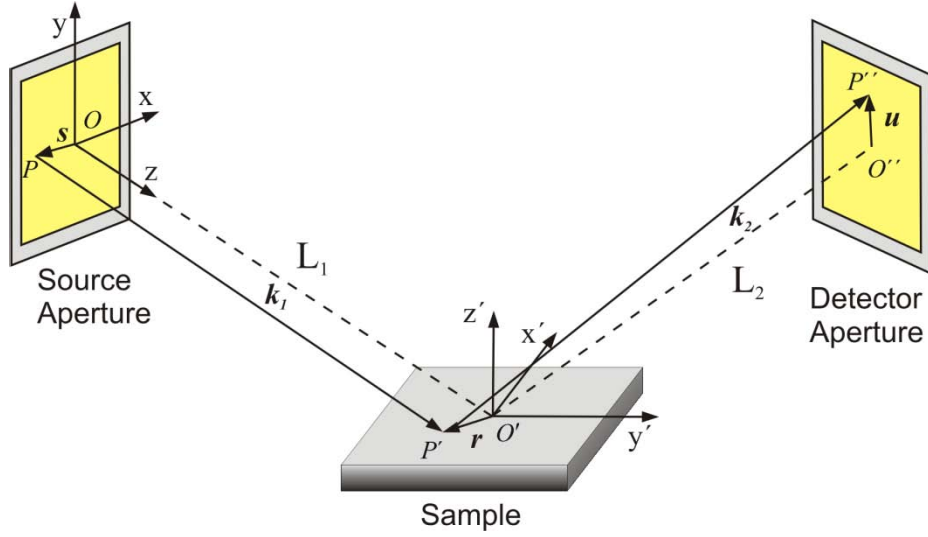


Fig. 5.6 Schematic set up of scattering geometry with source-fixed coordinates  $x$ - $y$ - $z$  and sample-fixed coordinates  $x'$ - $y'$ - $z'$ .

The scattered beam reaches the detector through aperture  $B$  normally oriented to the mean direction of the scattered beam at a distance  $L_2$ . Here it is assumed that the distances  $L_1$  and  $L_2$  are much larger than the typical aperture dimension of  $A$  and  $B$ .

The general expression for the scattered intensity is [5.3]

$$I(\mathbf{q}) = \left( \frac{e^2}{mc^2} \right)^2 \frac{\bar{\omega}}{2\pi\lambda^2} \frac{1}{L_1^2} \frac{1}{L_2^2} \frac{I}{A} \int d\Omega \tilde{F}[\bar{\omega}(1-\Omega)] \int_B d\mathbf{u} \hat{S}_\Omega(\mathbf{q} + k_{L_2}^2 \mathbf{u}) \quad (5.5)$$

Where  $S_\Omega(\mathbf{q})$  is given by the expression

$$\begin{aligned} \hat{S}_\Omega(\mathbf{K}) = & \iint d\mathbf{s} d\mathbf{s}' \Psi(\mathbf{s}) \Psi^*(\mathbf{s}') g(\mathbf{s} - \mathbf{s}') \exp\left\{i \frac{\Omega}{2} k_{L_1}^2 (s^2 - s'^2)\right\} \tilde{Q}_F(\mathbf{K} \\ & + \Omega k_{L_1}^2 \mathbf{s}) \tilde{Q}_F^*(\mathbf{K} + \Omega k_{L_1}^2 \mathbf{s}') \end{aligned} \quad (5.6)$$

The nominal wave vector transfer is  $\mathbf{q} = \mathbf{k}_2 - \mathbf{k}_1$  with mean wavelength and frequency  $\lambda$  and  $\bar{\omega}$  respectively. The variable  $\Omega$  is given by  $\Omega = 1 - \Delta\omega/\bar{\omega} = 1 + \Delta\lambda/\lambda$  with  $\Delta\lambda/\lambda$  expressing the deviation from the monochromaticity of the incoming radiation.  $\Omega \equiv 1$  means a perfectly monochromatic incident beam. The function  $\tilde{F}[\bar{\omega}(1-\Omega)]$  is the Fourier transform of the normalized time autocorrelation function  $F(\tau) = \exp(-\tau/\tau_l)$  of the source which decays with a characteristic time  $\tau_l$  corresponding to the longitudinal coherence length  $\xi_l = c\tau_l$ , where  $c$  is the speed of light.



The terms  $k_{L_1}$  and  $k_{L_2}$  are defined as

$$k_{L_{1,2}} = \sqrt{\frac{k_0}{L_{1,2}}} \quad (5.7)$$

The function  $\Psi(\mathbf{s})$  defines the shape of the incoming aperture and the function  $g(x)$  is the coherence factor and may be approximated by a Gaussian form

$$g(x) = \exp\left(-\frac{1}{2}x^2/\xi_x^2\right) \exp\left(-\frac{1}{2}y^2/\xi_y^2\right) \quad (5.8)$$

The term  $\tilde{\varrho}_F$  is the Fourier transform of a modified density referred to as Fresnel electron density given by

$$\varrho_F(\mathbf{r}) = \varrho(\mathbf{r}) \exp\left\{i\frac{\Omega}{2}(k_{L_1}^2 \mathbf{r}_{\perp,1}^2 + k_{L_2}^2 \mathbf{r}_{\perp,2}^2)\right\} \quad (5.9)$$

Where  $\mathbf{r}_{\perp,1}$  and  $\mathbf{r}_{\perp,2}$  are the components of  $\mathbf{r}$  perpendicular to the mean directions of the incoming and outgoing x-ray beams  $\hat{\mathbf{k}}_1$  and  $\hat{\mathbf{k}}_2$  respectively and similarly for  $\mathbf{r}'$ .

The Fresnel electron density  $\varrho_F(\mathbf{r})$  contains physical electron density  $\varrho(\mathbf{r})$  along with a phase factor which depends on the directions of the incident and scattered beams.

The arguments of  $\tilde{\varrho}_F$  in equation (5.18) represent the Cartesian components  $(K_x, K_y, K_z)$  relative to the  $(x, y, z)$  axes with  $z$  axis along the average incident beam direction (see Fig. 5.4) and  $x$  – and  $y$  – axes are in the plane of the incident slit.

The sample-fixed coordinates  $(K_{x'}, K_{y'}, K_{z'})$  are more appropriate in scattering experiments (see Fig. 3.7) and these may be easily calculated via

$$K_{x'} = K_x \quad (5.10)$$

$$K_{y'} = -K_y \sin\alpha + K_z \cos\alpha \quad (5.11)$$

$$K_{z'} = -K_y \cos\alpha - K_z \sin\alpha \quad (5.12)$$

where  $\alpha$  is the mean angle between  $\mathbf{k}_1$  and the surface of the sample or the incident angle  $\alpha_i$  in Fig. 3.7.

The vertical and horizontal transverse coherence lengths at EDR beamline are  $\xi_v \sim 53 \mu\text{m}$  and  $\xi_h \sim 43 \mu\text{m}$  respectively for 8 keV x-rays at  $\sim 31$  m from the source. Entrance pinhole of typical size  $10 \mu\text{m}$  or  $15 \mu\text{m}$  ensures that the incoming x-ray beam is fully coherent. For such coherent limit the expression for  $\hat{S}_\Omega(\mathbf{K})$  takes the following form

$$\hat{S}(\mathbf{K}) = \left| \int d\mathbf{s} \Psi(\mathbf{s}) \exp(i\Omega k_{L_1}^2 s^2 / 2) \tilde{q}_F(\mathbf{K} + \Omega k_{L_1}^2 \mathbf{s}) \right|^2 \quad (5.13)$$

Here the suffix  $\Omega$  is omitted.

Let us consider a single surface with random steps of width  $d_j$  and height  $h_j$ , as in section 5.1.1. The Fourier transform of the Fresnel electron density is given by [5.3]

$$\begin{aligned} \tilde{q}_F(\mathbf{K}') &= \frac{C}{2K_{z',-y'}} \exp \left\{ -\frac{i}{2\Omega} \frac{K_{y'}^2}{k_s^2 + ik_{L_1}^2 \varepsilon^2} \right\} \\ &\times \sum_j \exp(-iK_{z',-y'} h_j) \{ [C(y_{j+1}) - C(y_j)] + i[S(y_{j+1}) - S(y_j)] \} \end{aligned} \quad (5.14)$$

with  $y_j$  and  $y_{j+1}$  given by

$$y_{j,j+1} = \frac{K_{y'} - 2\Omega k_s^2 d_{j,j+1} - 2\Omega k_{sc}^2 h_j}{\sqrt{2\Omega\pi k_s^2}} \quad (5.15)$$

The functions  $C(x)$  and  $S(x)$  are the Fresnel integrals

$$C(x) = \frac{2}{\sqrt{\pi}} \int_0^x dt \cos(t^2) \text{ and } S(x) = \frac{2}{\sqrt{\pi}} \int_0^x dt \sin(t^2)$$

Different terms in equations (5.14) and (5.15) are as follows

$$C = \frac{(2\Omega)^{-\frac{1}{2}}l^3}{[2\Omega l^2(k_{L_1}^2 + k_{L_2}^2) + 4\pi^2 i]^{\frac{1}{2}}(k_s^2 + ik_{L_1}^2 \varepsilon^2)^{\frac{1}{2}}} \quad (5.16)$$

$$K_{z',-y'} = K_{z'} - \frac{k_{sc}^2}{k_s^2 + ik_{L_1}^2 \varepsilon^2} K_{y'} \quad (5.17)$$

$$k_s^2 = k_{L_1}^2 \sin^2 \alpha + k_{L_2}^2 \sin^2 \beta \quad (5.18)$$

$$k_{sc}^2 = k_{L_1}^2 \sin \alpha \cos \alpha - k_{L_2}^2 \sin \beta \cos \beta \quad (5.19)$$

$$\varepsilon^2 = 2\pi^2 / \Omega l^2 k_{L_1}^2 \quad (5.20)$$

where  $l$  is the extent of the sample and  $\beta$  is the angle between  $\mathbf{k}_2$  and the surface of the sample or the exit angle  $\alpha_f$  in Fig. 3.7.

### 5.3.2 Calculations based on the Fresnel electron density formalism

Calculations are performed, for the model set up as in ref. [5.3], for the scattered intensity distribution from a single smooth surface with zero roughness in the completely coherent limit based on equations (5.14) and (5.15). Slit width  $s = 50 \mu\text{m}$ , wavelength  $\lambda = 1 \text{ \AA}$  and the size of sample  $l = 1 \text{ cm}$  is chosen as in ref [5.3]. Perfect monochromatic x-ray beam with  $\Omega \equiv 1$  and the symmetric case with  $L_1 = L_2 = L$  is considered. Detector resolution folding in equation (5.5) i.e. the integration over the aperture B is neglected, to reduce the computation time.

Fig. 5.5 shows the calculated transverse  $q_{y'}$  scans with  $\alpha = \beta = 0.5^\circ$  for various slit-sample-detector distances  $L_1 = L_2 = L$ .

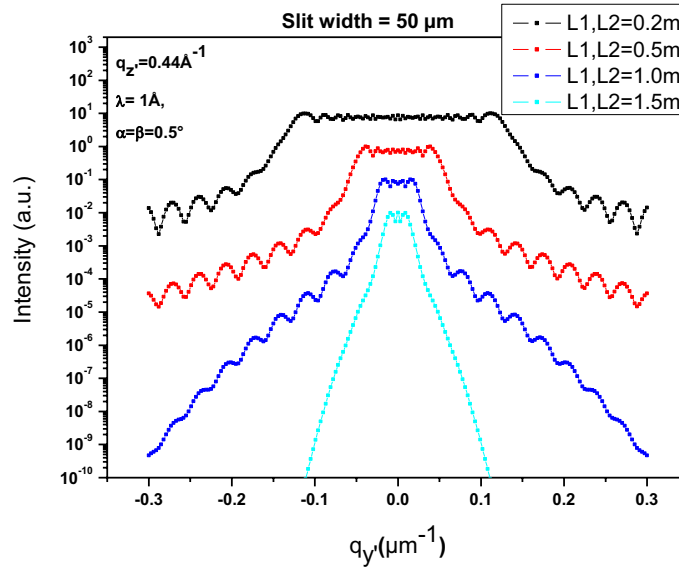


Fig. 5.5 Calculated transverse  $q_y$  scans at various distances  $L_1 = L_2 = L$  for a single smooth surface with zero roughness with  $s = 50 \mu\text{m}$ ,  $\lambda = 1 \text{ \AA}$ ,  $l = 1 \text{ cm}$  and  $q_z = 0.44 \text{ \AA}^{-1}$

Here the calculated intensity pattern exhibits fringe like structures even from a smooth surface with zero roughness. This fringe pattern originates from the slit diffraction effects. These effects are clearly visible for small distances. The fringe pattern is more enhanced at short distances and becomes less pronounced at larger distance  $\sim 1.5 \text{ m}$ . Also the peak is broader at short distances and becomes narrower with increasing distances. Thus it is clear that as the distance  $L$  increases the Fraunhofer regime is approached from the Fresnel regime and at distances  $L$  even larger than  $1.5 \text{ m}$ , the peak takes the form of delta function.

After testing for the model set up as in ref [5.3], the formalism is used to calculate the scattered intensity pattern in the detector plane for the set up of the real experiments. Various parameters are: slit width  $s = 10 \mu\text{m}$ ,  $\alpha = \beta = 0.2^\circ$ ,  $L_1 = 0.23 \text{ m}$ ,  $L_2 = 1.195 \text{ m}$ ,  $\lambda = 1 \text{ \AA}$  and  $\Omega \equiv 1$ . The size of the sample  $l$  is considered to be the footprint of the entrance pinhole at the sample position. Thus for  $10 \mu\text{m}$  pinhole at  $\alpha = 0.2^\circ$ ,  $l = \text{footprint} = 2.86 \text{ mm} \sim 3 \text{ mm}$ . The surface is considered to be perfectly smooth with zero roughness. The Fourier transform of the Fresnel electron density is calculated using equations (5.14) - (5.15). It is used to calculate the term  $\hat{S}(\mathbf{K})$  using equation (5.13) and further the scattered intensity using equation (5.5). Again here the detector resolution folding in equation (5.5) i.e. the integration over the aperture  $B$  is neglected.

The calculated transverse  $q_y$  scan based on the above formalism does not exhibit any diffraction pattern. It shows only a peak at the specular position (black curve) (Fig. 5.6) in contrast to the measured transverse  $q_y$  scan (red curve). Although the calculation is performed for the incoming aperture in the form of vertical slit instead of a pinhole as in the real experiment, the order of magnitude of various parameters are the same in calculation and experiment. It necessary to examine various terms involved in calculation of the scattered intensity.

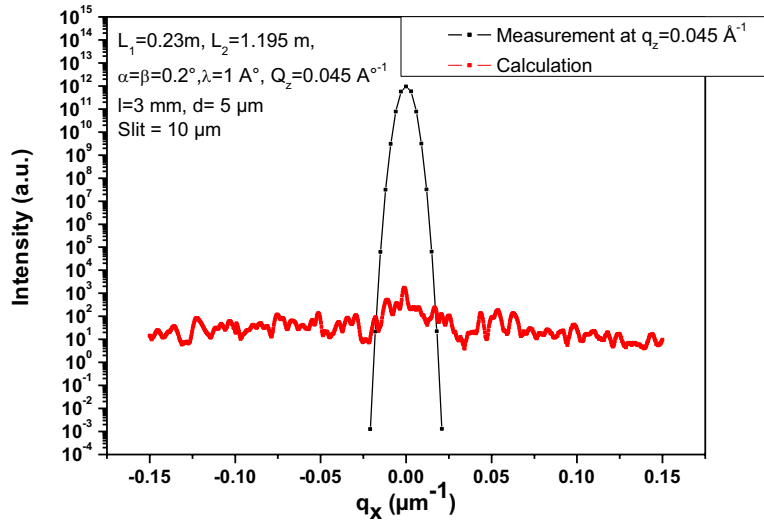


Fig. 5.6 Comparison of measured and calculated transverse  $q_y$  scan based on equation (5.17). Calculated pattern (black) shows a peak only at the specular position and cannot yield any fringe like pattern which like measured scan (red).

For the surface with  $h_j = 0$ , which is considered for the calculation, using equation (5.15) the term  $y_j$  becomes

$$y_j = \frac{K_{y'} - 2\Omega k_s^2 d_j}{\sqrt{2\Omega\pi k_s^2}} \quad (5.21)$$

For the present case with  $\alpha = \beta = 0.2^\circ$  and  $k_{L_1}^2 = 0.2732 \mu m^{-1}$ ,  $k_{L_2}^2 = 0.0526 \mu m^{-1}$ , the scattering vectors using equations (5.18) and (5.19) are  $k_s = 1.992 \times 10^{-3} \mu m^{-1}$  and  $k_{sc} = 2.775 \times 10^{-2} \mu m^{-1}$ .

The height function is described by a random arrangement of steps with widths  $0 \leq d_j \leq 5 \mu\text{m}$  and heights  $h_j = 0$  for all  $j$ 's over the length of the sample  $l = 3 \text{ mm}$ . With all these values in equation (5.21),

$$2\Omega k_s^2 d_j \sim 10^{-5} \mu\text{m}^{-1}$$

and  $K_{y'} \sim 10^{-1} \mu\text{m}^{-1}$

Hence the term  $2\Omega k_s^2 d_j$  is negligible as compared to  $K_{y'}$ , and the value of  $y_j$  is constant, typically  $\sim 20$  for all  $j$ 's.

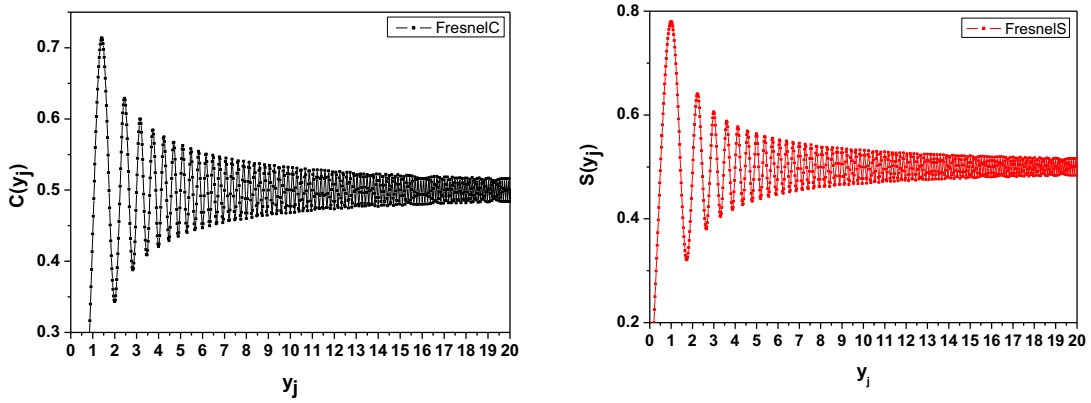


Fig. 5.7. Fresnel integrals as a function of  $y_j$ . Both  $C(y_j)$  and  $S(y_j)$  approach the value 0.5 for larger values of  $y_j$

For such a value of  $y_j$ , the Fresnel integrals  $C(y_j)$ ,  $S(y_j)$  reach a constant value  $\sim 0.5$  for all  $j$ 's (Fig.5.7). The Fourier transform of the Fresnel density, using equation (5.14), therefore, is zero and cannot contribute to any oscillatory behavior in the scattering amplitude.

As flat surface with zero roughness is hard to realize, surface can be considered to have certain roughness. Fig. 5.8 shows the values of  $y_j$  calculated using equation (5.21) for different surface heights  $h_j$  for a typical width of  $d_j = 5 \mu\text{m}$ . All other parameters are the same as in Fig. 5.6. The value of  $y_j < 10$  for  $h_j \approx 32 \mu\text{m}$  and  $y_j$  approaches  $\sim 4$  for  $h_j \approx 50 \mu\text{m}$ . Thus the surface with average roughness of few 10's of  $\mu\text{m}$  can exhibit some oscillatory behavior. But it is not realistic to consider a surface with such a large average roughness.

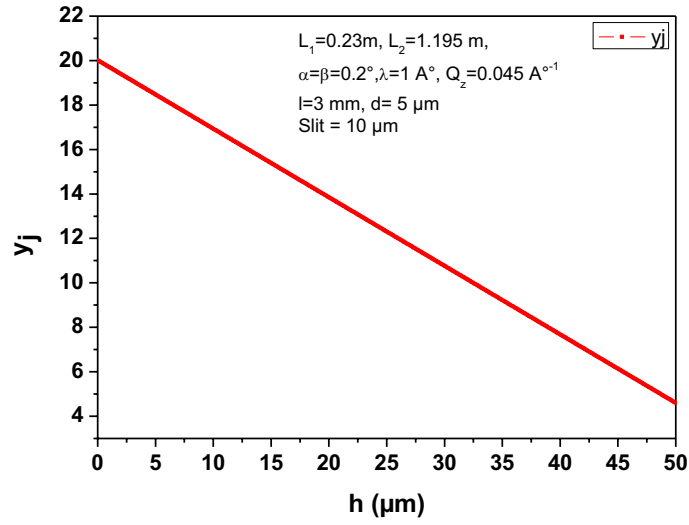


Fig. 5.8 The values of  $y_j$  against different surface heights  $h_j$

By increasing the width of the steps  $d_j$ 's the second term,  $2\Omega k_s^2 d_j$ , can be made larger and hence can yield different values of  $y_j$  for different  $j$ 's. Fig. (5.7) shows the calculation for  $0 \leq d_j \leq 100 \mu\text{m}$  and  $h_j = 0$  for all  $j$ 's with  $l = 100 \text{ mm}$ , thus 1001 different random values of  $d_j$ 's.

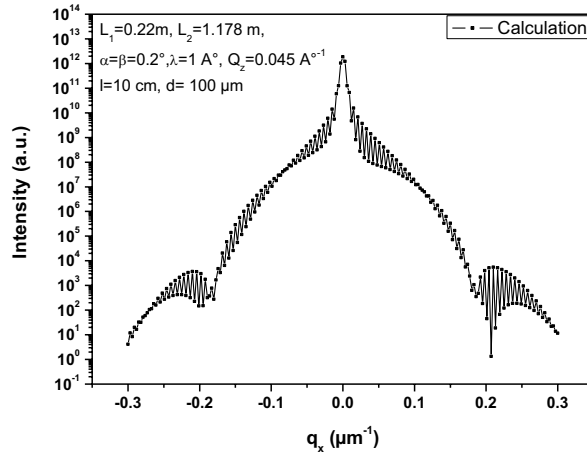


Fig. 5.9 Calculated transverse  $q_y$  scan for sample with length  $l = 100 \text{ mm}$  comprised of steps with widths  $0 \leq d_j \leq 100 \mu\text{m}$  and  $h_j = 0$  for all  $j$ 's.

But it is not realistic to consider that the entire sample length of  $l = 100 \text{ mm}$  to contribute to the scattering, while the footprint of the incoming beam is  $\sim 3 \text{ mm}$  only.

The formalism is expected to work well for the present set up parameters for large values of angles  $\geq 1^\circ$  but cannot exhibit any slit diffraction effects at smaller angles. Calculation is performed keeping all the parameters the same as in Fig. 5.6 but changing only the incident and exit angle to  $1^\circ$ . The calculated intensity scan (Fig. 5.10) does show slit diffraction effects.

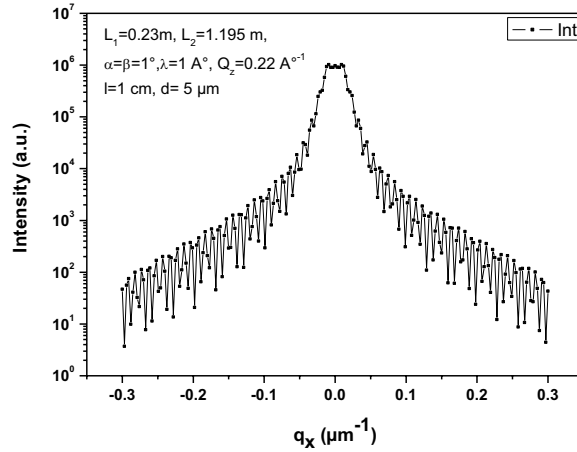


Fig. 5.10 Calculated transverse  $q_y$  scan at incident and exit angle of  $1^\circ$  at the same slit-sample and sample-detector distances ( $L_1$ ,  $L_2$  respectively) as in the real measurement.

## 5.4 Reconstruction using phase retrieval

The calculations of the amplitude of scattered wave from a surface as discussed in previous sections (sections 5.1, 5.2) are not satisfactory. The calculation of scattered intensity using equation (5.15) for a surface with random height distribution shows similar features as the measured intensity (Fig. 5.3). But the fit of calculated intensity pattern to the measured one is not promising. It is only by chance that the calculated pattern might fit the measured one after various attempts for the random surface height function. The calculations performed based Fresnel electron density approach (section 5.2) cannot exhibit any fringe pattern in the calculated intensity, rather shows only a broad specular peak for a perfectly flat surface with zero roughness (Fig. 5.6).

Phase retrieval techniques, as discussed in section 2.5, are widely used to reconstruct electron density from coherent x-ray diffraction experiments [5.6, 5.7]. These techniques are also used to reconstruct surface from coherent reflectivity measurements [5.8, 5.9] with monochromatic



x-rays. Although, it is more difficult task to retrieve surface morphology from the coherent reflectivity data than to retrieve electron density from coherent diffraction data as the quantity sought itself is the phase. Symmetry properties of electron density do not help to improve the quality of reconstruction.

This section discusses the calculations based on phase retrieval techniques. The commonly used phase retrieval algorithms, as discussed in section 2.6, cannot be directly applied to reconstruct the surface height distribution for the present experimental set up parameters. This section discusses the modifications performed on the algorithms to take into account the reflection geometry in one dimension, the illumination function at the sample position and the Fresnel propagator for the path from the sample to the detector plane in reflection geometry. The modified algorithms are initially tested for a model surface and then applied to reconstruct surface morphology from the real measurements.

The commonly used Fourier based phase retrieval algorithms, as discussed in section 2.6, consider that the detector is in the far-field of the object. The second order terms in the phase contribution from the object are not considered. As pointed out in Fig. 5.2(B), for the set up parameters at EDR beamline the Fresnel number is in the range  $10^4 - 10^5$  for the energies from  $\sim 2$  to  $40$  keV for typical sample-detector distance of 1.2 m. Hence it is essential to consider these second order terms as discussed in section 5.2.

### **5.4.1 Reconstruction of object electron density from near-field diffraction**

In far-field Fraunhofer regime, because of the direct Fourier transform relationship between an object and the diffraction pattern it is possible to retrieve the original object using the conventional phase retrieval algorithms. The retrieval of the original object from a near-field diffraction pattern is not so straightforward because of the presence of Fresnel diffraction fringes.

The introduction of a phase chirped distorted object relates the diffraction pattern to the object by the direct Fourier transform. In fact, this makes it is valid for all the wave propagation regimes, from near-field to far-field.

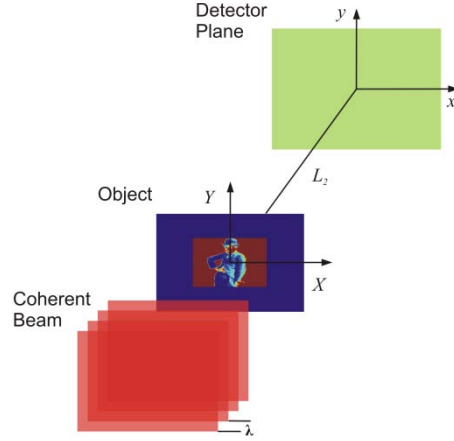


Fig. 5.11 Schematic set up for diffraction geometry in transmission for coherent x-ray radiation of wavelength  $\lambda$ . Object in  $X$ - $Y$  plane and detector in  $x$ - $y$  plane

Let us consider a transmission diffraction geometry, as in Fig. 5.11, for a thin object with density function  $\rho(X, Y)$ . The object with nonzero density is surrounded by a zero density region (Blue). The region with nonzero density is called as support  $S$  (see Fig. 2.10).

The amplitude of diffracted wave in transmission is given by Fresnel-Kirchhoff diffraction formula as [5.4],

$$A(x, y) = \frac{i}{\lambda} \iint \rho(X, Y) \frac{e^{-ikr}}{r} dXdY \quad (5.22)$$

where  $r = (L_2^2 + (x - X)^2 + (y - Y)^2)^{1/2}$  is the length of the position vector from point  $P_0(X, Y)$  on the object plane to point  $P_1(x, y)$  on the detector plane.

For  $L_2 \gg \max(X, Y)$ , using standard paraxial approximation  $r$  can be expanded as

$$r \approx L_2 + \frac{(x - X)^2 + (y - Y)^2}{2L_2} \quad (5.23)$$

For the term in the denominator in the integrand  $r \approx L_2$  at large distances. The diffracted amplitude is

$$A(x, y) = \frac{ie^{ikL_2}}{\lambda L_2} \iint \rho(X, Y) e^{-ik \frac{(x-X)^2 + (y-Y)^2}{2L_2}} dXdY \quad (5.24)$$

Expanding the exponential terms the amplitude can be written as

$$A(x, y) = \frac{ie^{ikL_2}}{\lambda L_2} \iint \rho(X, Y) e^{-\frac{ik}{2L_2}(X^2+Y^2)} e^{-\frac{ik}{L_2}(xX+yY)} dXdY \quad (5.25)$$

In the far-field regime where  $L_2 \gg \frac{(X^2+Y^2)}{\lambda}$ , the Fresnel propagator term

$$e^{-i\varphi_P} = e^{-\frac{ik}{2L_2}(X^2+Y^2)} \approx \text{constant}$$

over the whole image. The amplitude, in this case, can be simply written as

$$A(x, y) \approx \frac{ie^{ikL_2}}{\lambda L_2} \iint \rho(X, Y) e^{-\frac{ik}{L_2}(xX+yY)} dXdY \quad (5.26)$$

which is similar to equation (2.55). Thus the diffraction amplitude and the object density function are related by Fourier transform i.e.  $A(x, y) \approx \mathcal{F}(\rho(X, Y))$ .

In near-field regime, the Fresnel propagator term  $e^{-i\varphi_P}$  is not constant and cannot be omitted. So as to relate  $A(x, y)$  and  $\rho(X, Y)$  by Fourier transform a phase chirped distorted object is defined as

$$\bar{\rho}(X, Y) = \rho(X, Y) e^{-\frac{ik}{2L_2}(X^2+Y^2)} \quad (5.27)$$

so that the diffraction amplitude is written as

$$A(x, y) = \frac{ie^{ikL_2}}{\lambda L_2} \iint \bar{\rho}(X, Y) e^{-\frac{ik}{L_2}(xX+yY)} dXdY \quad (5.28)$$

$$A(x, y) = \mathcal{F}(\bar{\rho}(X, Y)) \quad (5.29)$$

$$A(q_x, q_y) = \mathcal{F}(\bar{\rho}(X, Y)) \quad (5.30)$$

where the momentum transfer  $(q_x, q_y) = (kx/L_2, ky/L_2)$ .

The insertion of the additional quadratic phase term  $e^{-i\varphi_P}$  makes the relationship (5.28) universal. It can be used both in the near-field as well as in the far-field [5.10, 5.11].

Fig. 5.12 shows the calculation of diffracted intensity of x-rays with wavelength  $\lambda = 1.54 \text{ \AA}$  at various distances from the object. In near-field regime, the diffraction pattern resembles

the object itself. As the distance of the detector plane from the object increases, the diffraction pattern shows bright central spot and speckle pattern along with strong oscillations along  $x$  and  $y$  directions. Fig. 5.12 also shows the calculation of Fresnel propagator term  $e^{-i\varphi_P}$  at various distances. At short distances large number of Fresnel phase zones of width  $\pi$  are clearly visible. At larger distances only the first phase zone contributes. At such distances the propagator term  $e^{-i\varphi_P}$  can be approximated to unity over the whole detector and hence can be omitted.

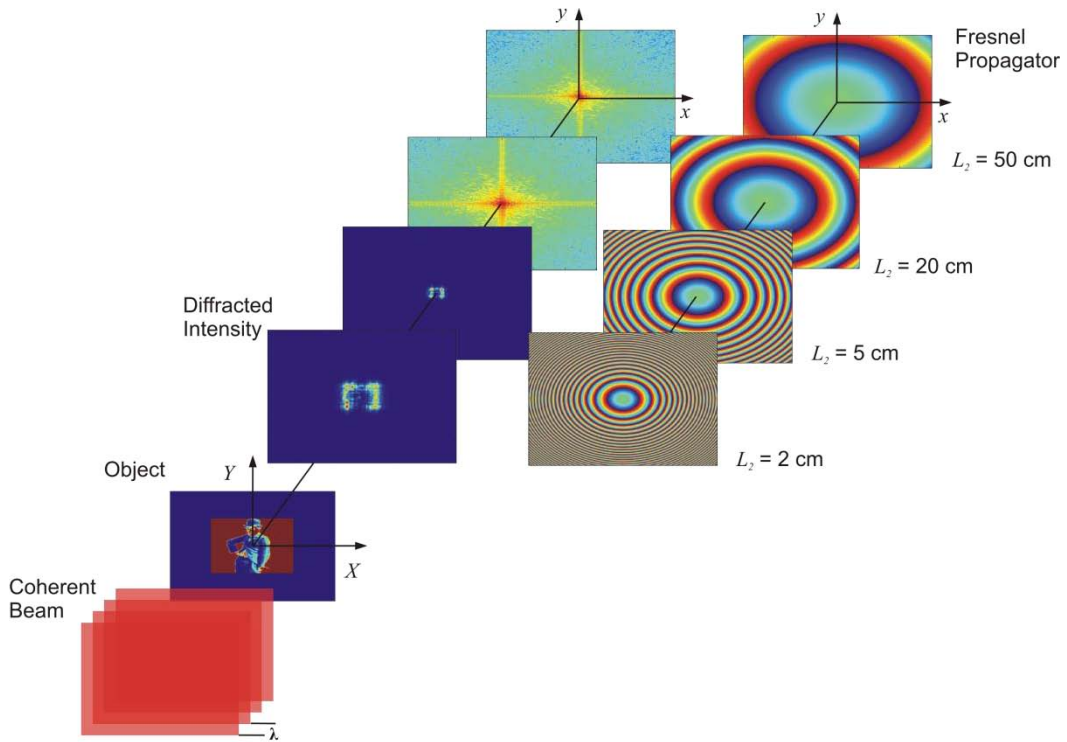


Fig. 5.12 Calculation of diffraction pattern for a model object in transmission at various distances. Calculated Fresnel propagator term is also shown at various distances.

The propagator term is introduced in the commonly used hybrid input-output algorithm (see Fig. 2.13) as described below:

Start with the random phases in the interval  $[-\pi, \pi]$  in the detector plane

$$\varphi_1 = \text{rand} [-\pi, \pi] \quad (5.31)$$

$$G'_1(q_x, q_y) = |A(q_x, q_y)| \exp(-i\varphi_1) \quad (5.32)$$

$$g_1(X, Y) = |g_1(X, Y)| \exp(i\Phi_1) = \mathcal{F}^{-1}(G'_1(q_x, q_y)) \quad (5.33)$$

- (i) Get the scattering amplitude by replacing the modulus of the measured scattered amplitude

$$G_k(q_x, q_y) = |A(q_x, q_y)| \exp(-i\Phi_k) \quad (5.34)$$

- (ii) Fourier transform this estimate of the scattered amplitude

$$g'_k(X, Y) = |g'_k(X, Y)| \exp(i\varphi_k) = \mathcal{F}^{-1}(G_k(q_x, q_y)) \quad (5.35)$$

- (iii) Get the estimate of the object for the next iteration

$$g_{k+1}(X, Y) = \begin{cases} g'_k(X, Y), & (X, Y) \in S \\ g_k(X, Y) - \beta |g'_k(X, Y)| \exp\left(-\frac{ik}{2L_2}(X^2 + Y^2)\right), & (X, Y) \notin S \end{cases} \quad (5.36)$$

where  $S$  is the support region with nonzero electron density and  $\beta$  is the feedback factor.

- (iv) Fourier transform the estimate of the object to get the scattering amplitude for the next iteration

$$\begin{aligned} G_{k+1}(q_x, q_y) &= |G_{k+1}(q_x, q_y)| \exp(i\Phi_{k+1}) \\ &= \mathcal{F}\left(|g_{k+1}(X, Y)| \exp\left(-\frac{ik}{2L_2}(X^2 + Y^2)\right)\right) \end{aligned} \quad (5.37)$$

The introduction of the propagator term  $e^{-i\varphi_P}$  makes the modified HIO algorithm faster for reconstructions in near-field region. It is illustrated below in case of reconstruction for diffraction by a model object.

Fig. 5.13 shows the reconstruction for far-field diffraction of x-rays with  $\lambda = 1.54 \text{ \AA}$  at 1m from the object. The HIO algorithm applied for far-field diffraction faces a problem of twin image. The algorithm cannot distinguish between the real object with density function  $\rho(X, Y)$  and its twin image  $\rho^*(-X, -Y)$ . Even after 300 iterations the reconstruction shows the twin image of the real object and the sum squared error  $\chi^2$  reaches 0.2701. The existence of the twin image slows down the convergence of the retrieval. Also the algorithm stagnates and cannot result in a unique reconstruction. The additional quadratic factor  $e^{-i\varphi_P}$  in the

phase helps to remove the twin image problem in reconstruction and makes the reconstruction faster and unique.

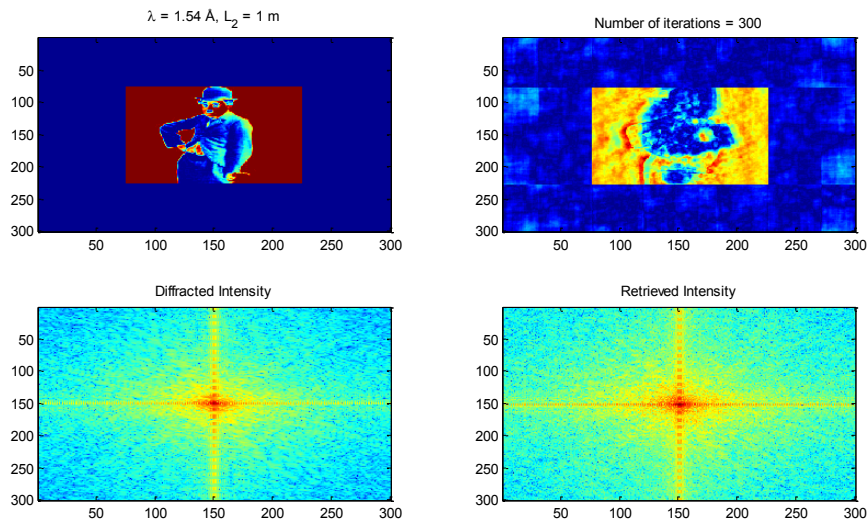


Fig. 5.13 Reconstruction after 300 iterations for far-field (1 m) diffraction using normal HIO algorithm. The reconstruction (upper right) shows the twin image of the real object (upper left).

Fig. 5.14, 5.15 show the reconstruction for near-field diffraction of  $\lambda = 1.54 \text{ \AA}$  x-rays at 5 cm from the model object<sup>o</sup>, with the feedback factor  $\beta = 0.8$ . Within few numbers of iterations the reconstruction already starts to show the features of the real object. The algorithm does not stagnate and converges to an unambiguous solution in only  $\sim 20$  iterations. The quality of the reconstruction improves by applying the algorithm for further number of iterations. In 150 iterations the algorithm finds a converging solution with sum squared error of  $4.6 \times 10^{-3}$ .

## Surface profile reconstruction from coherent x-ray reflectivity

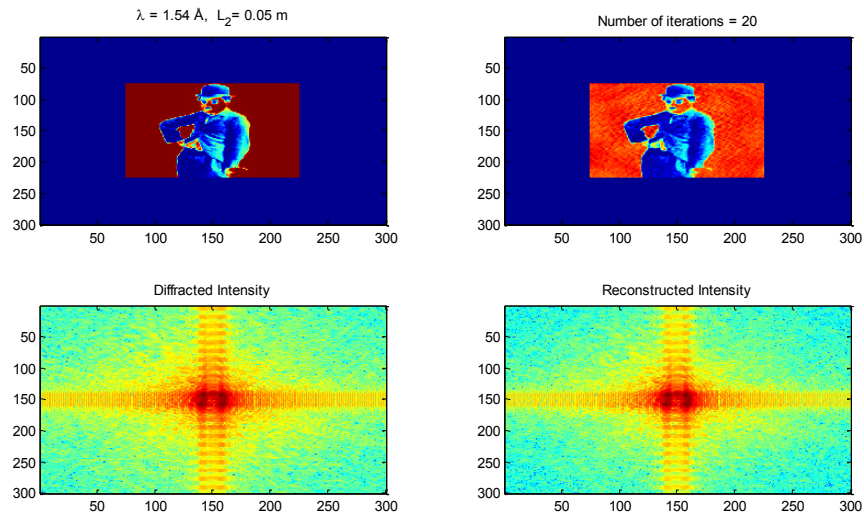


Fig. 5.14 Reconstruction for near-field (5 cm) diffraction using modified HIO algorithm with additional propagator term, with the feedback factor  $\beta = 0.8$ . The algorithm reaches unambiguous solution in  $\sim 20$  iterations.

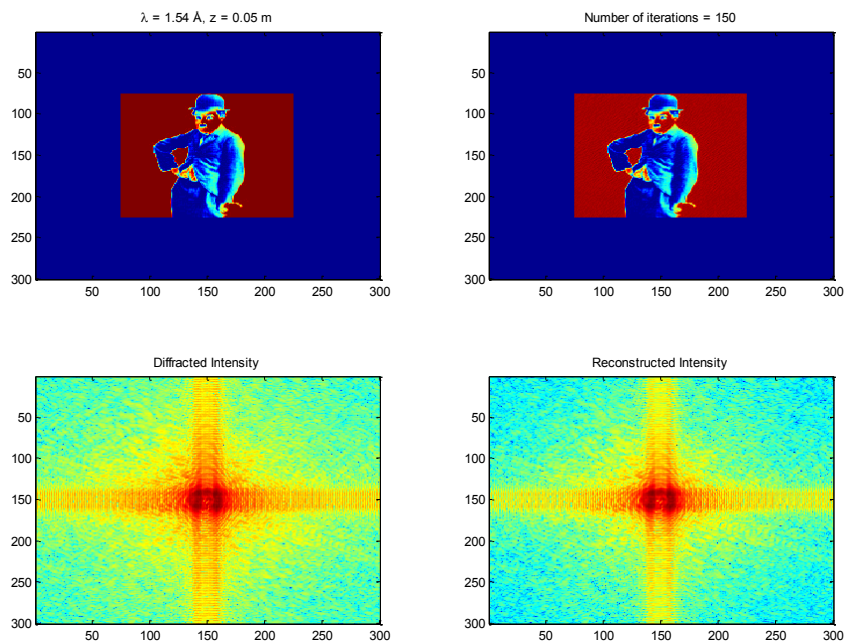


Fig. 5.15 Reconstruction for near-field (5 cm) diffraction using modified HIO algorithm with additional propagator term, with the feedback factor  $\beta = 0.8$ . The algorithm reaches converging solution in 150 iterations with sum squared error of  $4.6 \times 10^{-3}$ .

### 5.4.2 Reconstruction from near-field diffraction in reflection geometry

In case of reflection of light from sample surface, the direction of propagation undergoes important and major changes. The theory developed for scattering amplitude is for the case of light propagation in transmission. So as to get a Fourier transform relationship between the density distribution and the scattering amplitude, the theory needs to be extended further for reflection geometry.

Consider a schematic setup as in Fig. 5.15. In the sample fixed coordinate system the sample is in  $X - Y$  plane and  $Z$  axis normal to the sample surface. The incoming beam is incident on the sample along  $Y$  direction making an incident angle of  $\alpha_i$ . The coordinate system for the detector is the same as in Fig. 5.11 with the following relation between the axes of the two coordinate systems

$$x - axis \parallel X - axis$$

$$y - axis \parallel Z - axis$$

$$z - axis \parallel Y - axis$$

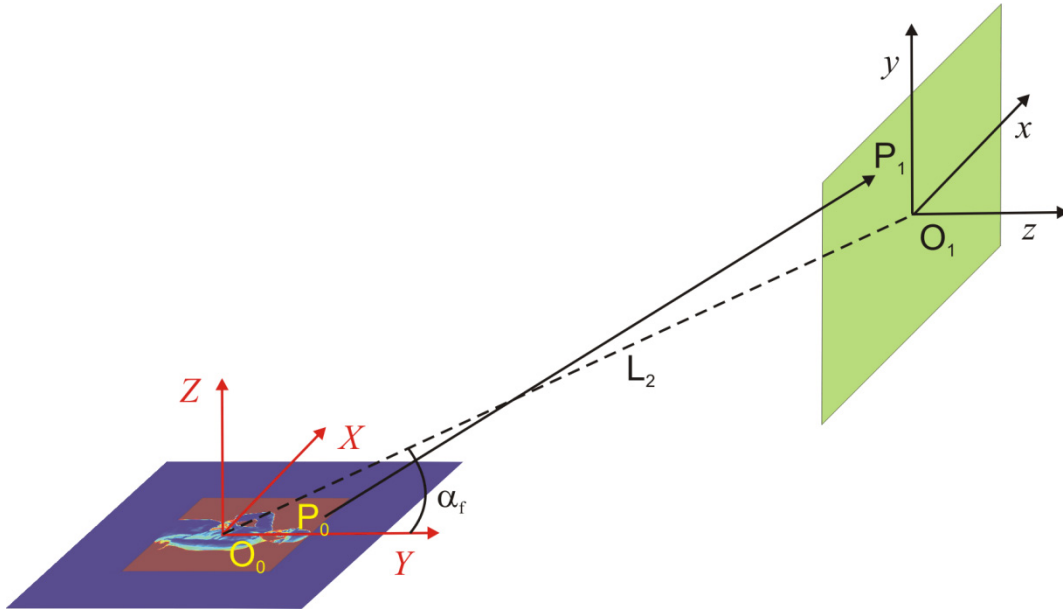


Fig. 5.15 Schematic set up for diffraction geometry in reflection for coherent x-ray radiation of wavelength  $\lambda$ . Object in  $X$ - $Y$  plane and detector in  $x$ - $y$  plane



Let the coordinates of the origin  $O_1$  in the coordinate system  $(O_1, X, Y, Z)$  be  $(X_1, Y_1, Z_1)$ .

The general expression for amplitude of diffracted wave [5.4], similar to equation (5.31),

$$A(x, y) = \frac{i}{\lambda} \iint \rho(X, Y) \frac{e^{-ikr}}{r} \times \cos(\mathbf{n}, \mathbf{r}) dXdY \quad (5.38)$$

where  $\mathbf{r}$  is the position vector from  $P_0$  to  $P_1$  and  $\mathbf{n}$  is the normal the surface of the sample i.e. along  $Z - axis$  in this case.  $\cos(\mathbf{n}, \mathbf{r})$  is the cosine of the angle between  $\mathbf{n}$  and  $\mathbf{r}$  which is given by

$$\cos(\mathbf{n}, \mathbf{r}) = \frac{y+Z_1}{r} \approx \frac{Z_1}{r} \quad \text{where } y \ll Z_1.$$

In case of transmission geometry, as in Fig. 5.11,  $\cos(\mathbf{n}, \mathbf{r}) = 1$  as angle between the surface normal  $\mathbf{n}$  and position vector  $\mathbf{r}$  is zero.

Also at large distances  $r \approx L_2$ , hence the expression for diffraction amplitude becomes

$$A(x, y) = \frac{iZ_1}{\lambda L_2^2} \iint \rho(X, Y) e^{-ikr} dXdY \quad (5.39)$$

The length of the position vector  $\mathbf{r}$  is given by

$$r = [(x + X_1 - X)^2 + (y + Y_1 - Y)^2 + (z + Z_1 - Z)^2]^{1/2} \quad (5.40)$$

After expanding the expression for  $r$  and substituting, the diffraction amplitude can be written as

$$A(x, y) = C \times \mathcal{F} \left( \rho(X, Y) \exp \left\{ -\frac{ik}{L_2} \left( \frac{1-l^2}{2} X^2 + \frac{1-m^2}{2} Y^2 - nlXY \right) \right\} \right) \quad (5.41)$$

Here  $C$  is a constant and  $l = \frac{X_1}{L_2}$ ,  $m = \frac{Y_1}{L_2}$ ,  $n = \frac{Z_1}{L_2}$  are the direction cosines.

The detail steps can be found in Appendix (A).

The quadratic propagator term given by,

$$e^{-i\Phi_P} = \exp \left\{ -\frac{ik}{L_2} \left( \frac{1-l^2}{2} X^2 + \frac{1-m^2}{2} Y^2 - nlXY \right) \right\} \quad (5.42)$$

For a coplanar geometry in  $Y-Z$  plane,  $O_1 \equiv (0, Y_1, Z_1)$  with sample confined in  $X-Y$  plane and for any point on the detector plane ( $x-y$  plane) the direction cosines are given by

$$\begin{aligned} l &= \frac{X_1}{L_2} = 0 \\ m &= \frac{Y_1}{L_2} = \cos \alpha_f \\ n &= \frac{Z_1}{L_2} = \sin \alpha_f \end{aligned}$$

where  $\alpha_f$  is the mean exit angle.

The propagator term can be written as

$$e^{-i\Phi_P} = \exp \left\{ -\frac{ik}{L_2} \left( \frac{1-0^2}{2} X^2 + \frac{1-\cos^2 \alpha_f}{2} Y^2 - \sin \alpha_f \cdot 0 \cdot XY \right) \right\} \quad (5.43)$$

$$e^{-i\Phi_P} = \exp \left\{ -\frac{ik}{2L_2} (X^2 + Y^2 \sin^2 \alpha_f) \right\} \quad (5.44)$$

The quadratic propagator phase term  $e^{-i\Phi_P}$  is similar to that for the transmission case except additional angular component  $\sin^2 \alpha_f$  along  $Y$  - direction. The propagator term  $e^{-i\Phi_P}$  can now be introduced in the conventional Hybrid input-output algorithm as discussed through equations (5.40) - (5.45) by replacing  $e^{-i\phi_P}$  with  $e^{-i\Phi_P}$ .

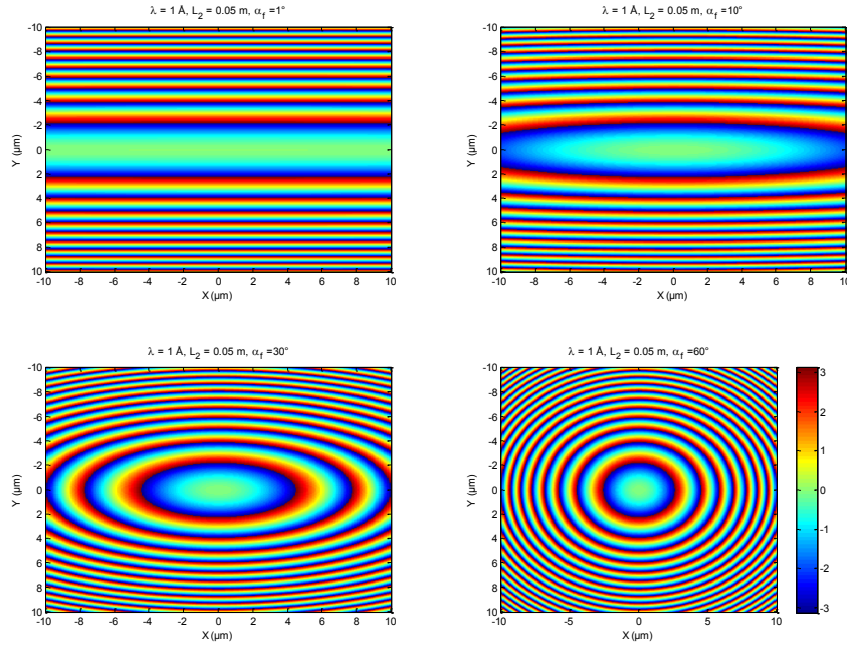


Fig. 5.16 Calculations for  $e^{-i\Phi_P}$  for sample-detector distance of 5 cm at  $\alpha_f = 1^\circ, 10^\circ, 30^\circ, 60^\circ$

Fig. 5.16 shows the calculated propagator phase term  $e^{-i\Phi_P}$  for sample-detector distance  $L_2 = 5 \text{ cm}$  at different values of exit angle  $\alpha_f = 1^\circ, 10^\circ, 30^\circ, 60^\circ$ . The dimensions of the object are  $10 \mu\text{m} \times 10 \mu\text{m}$ . At lower values of  $\alpha_f = 1^\circ$  and  $\alpha_f = 10^\circ$  the phase  $e^{-i\Phi_P}$  oscillates rapidly along  $Y$  – direction which is the direction of inclination of the sample. Fresnel zones of period  $\pi$  along  $Y$  – direction can be observed. Along  $X$  – direction the phase  $e^{-i\Phi_P}$  is almost constant over the whole sample and shows only first Fresnel zone. At higher values of  $\alpha_f = 30^\circ$  and  $\alpha_f = 60^\circ$  the shape of the phase term becomes to more symmetric. More number of Fresnel zones appear along  $X$  – direction. The propagator term  $e^{-i\Phi_P}$  is symmetric with concentric phase rings of width  $\pi$  at  $\alpha_f = 90^\circ$  and is equivalent to its transmission counterpart  $e^{-i\Phi_P}$ , as it is evident from its expression in equation (5.44).

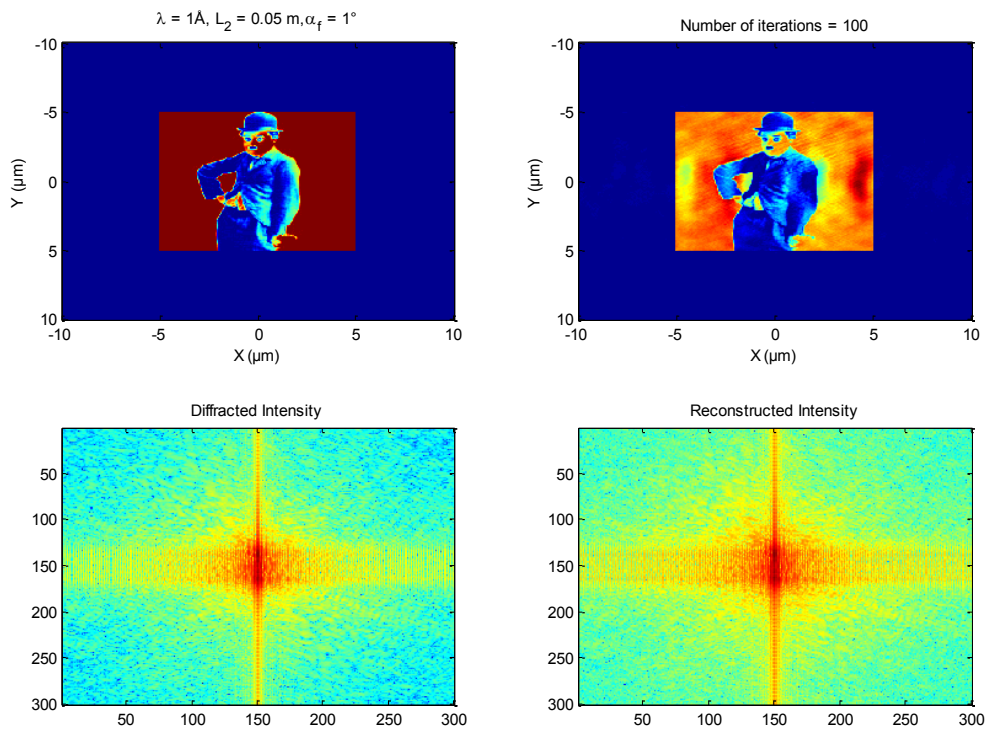


Fig. 5.17 Reconstruction for near field (5cm) diffraction for a model object in reflection at  $\alpha_i = \alpha_f = 1^\circ$ , with the feedback factor  $\beta = 0.8$ . The propagator term in equation (5.44) is included to the modified HIO algorithm as described through equations (5.31)-(5.37).

Fig. 5.17 shows the reconstruction for the near-field diffraction at  $L_2 = 5 \text{ cm}$  from a model object in reflection at incident and exit angle of  $1^\circ$ , with the feedback factor  $\beta = 0.8$ . The calculated diffraction pattern shows rapid oscillations along  $x$  – direction than along  $y$  – direction.

The rate of reconstruction is slower than for transmission case. One of the reasons being the asymmetry in the quadratic phase term for  $\alpha_f = 1^\circ$  as shown in Fig. 5.16. It oscillates rapidly along  $Y$  – direction, whereas it is almost constant along  $X$  – direction. Within 100 iterations unambiguous solutions starts to appear. The reconstruction also shows the images of the object, which disappear if the algorithm is run for further iterations. Finally it yields a unique solution in  $\sim 300$  iterations. The presence of the additional quadratic phase term helps to remove the twin image problem also for this case.

## 5.5 Reconstruction of surface height profile from near-field diffraction

The above stated phase retrieval algorithms reconstruct the electron density from the diffraction pattern. In case of scattering of coherent x-rays from a surface, it is the phase of the scattered amplitude which is modulated by the local surface height. It is more difficult to reconstruct the phase than the electron density as the real space properties of the electron density are no more applicable.

In section 5.3, it is made clear that for the measurement performed in near-field of the sample it is important to include the quadratic propagator phase term. The phase retrieval algorithms are now further modified to include the propagator term and to seek the surface height profile.

For the scattering geometry in Fig. 3.7, the amplitude of the scattered wave from a surface or the speckle amplitude is [5.6, 5.7]

$$A(q_x) = \int |B(x)| e^{i\varphi_F(x)} e^{iq_z h(x)} e^{iq_x x} dx \quad (5.45)$$

As pointed out in section 5.4, for the measurement of performed in near-field of the sample, the inclusion of the propagator phase term is important. The 1D quadratic propagator term for the scattering geometry in Fig. 3.7 can be written as

$$e^{-i\Phi_P^1} = \exp\left\{-\frac{ik}{2L_2}(x^2 \sin^2 \alpha_f)\right\} = \exp\left\{-\frac{i\pi}{\lambda L_2}(x^2 \sin^2 \alpha_f)\right\} \quad (5.46)$$

With this the expression for the speckle amplitude is

$$A(q_x) = \int |B(x)| e^{i\varphi_F(x)} e^{iq_z h(x)} e^{-i\Phi_P^1} e^{iq_x x} dx \quad (5.47)$$

$$A(q_x) = \int |B(x)| e^{i\varphi_F(x)} e^{iq_z h(x)} e^{-\frac{i\pi}{\lambda L_2} (x^2 \sin^2 \alpha_f)} e^{iq_x x} dx \quad (5.48)$$

So as to use it in phase retrieval algorithm, this is recognized as Fourier transform

$$A(q_x) = \mathcal{F} \left( |B(x)| e^{i\varphi_F(x)} e^{iq_z h(x)} e^{-\frac{i\pi}{\lambda L_2} (x^2 \sin^2 \alpha_f)} \right) \quad (5.49)$$

For the measurement with sample size larger than the footprint, the real space constraint of support region ( $S$ ) cannot be applied. There exists no region with zero electron density, but the whole footprint region on the sample surface contributes to the scattering. Hence the modified HIO algorithms as discussed in section 5.4 cannot be used to retrieve the surface height profile.

Instead, the Gerchberg-Saxton (GS) algorithm, as described in Fig. 2.11, is the suitable algorithm.

Initially the calculations based on the GS algorithm without the inclusion of the phase of the illumination function and the propagator term is discussed.

The constraint is applied in real space by replacing the magnitude of the estimate by the magnitude of the illumination function i.e.  $|B(x)|$ . The surface height profile is obtained from the retrieved phase. The steps in the algorithm are described below:

Start with the random phases in the interval  $[-\pi, \pi]$  in the sample plane

$$\varphi_1 = \text{rand} [-\pi, \pi] \quad (5.50)$$

- (i) Replace the modulus of the estimate by modulus of the illumination function

$$g'_k(x) = |B(x)| \exp(-i\varphi_k) \quad (5.51)$$

- (ii) Fourier transform this estimate of the scatterer to get the scattering amplitude

$$G'_k(q_x) \exp(-i\Phi'_k) = \mathcal{F}(g'_k(x)) \quad (5.52)$$

- (iii) Replace the modulus of the scattering amplitude by the modulus of the calculated amplitude  $|A(q_x)|$ ,

$$G_k(q_x) = |A(q_x)| \exp(-i\Phi'_k(q_x)) \quad (5.53)$$

- (iv) Fourier transform the estimate of the scattering amplitude to get the next estimate for the phase

$$g_{k+1}(x) = |g_{k+1}(x)| \exp(i\varphi_{k+1}) = \mathcal{F}^{-1}(G_k(q_x)) \quad (5.54)$$

$$h_{k+1}(x) = \varphi_{k+1}/q_z \quad (5.55)$$

The above stated algorithm is tested for a test periodic surface. A surface in the form a grating with period 100  $\mu\text{m}$  and depth 10 nm is considered. Fig. 5.18 shows various attempts of the reconstruction with different initial phase and for 1000 iterations each.

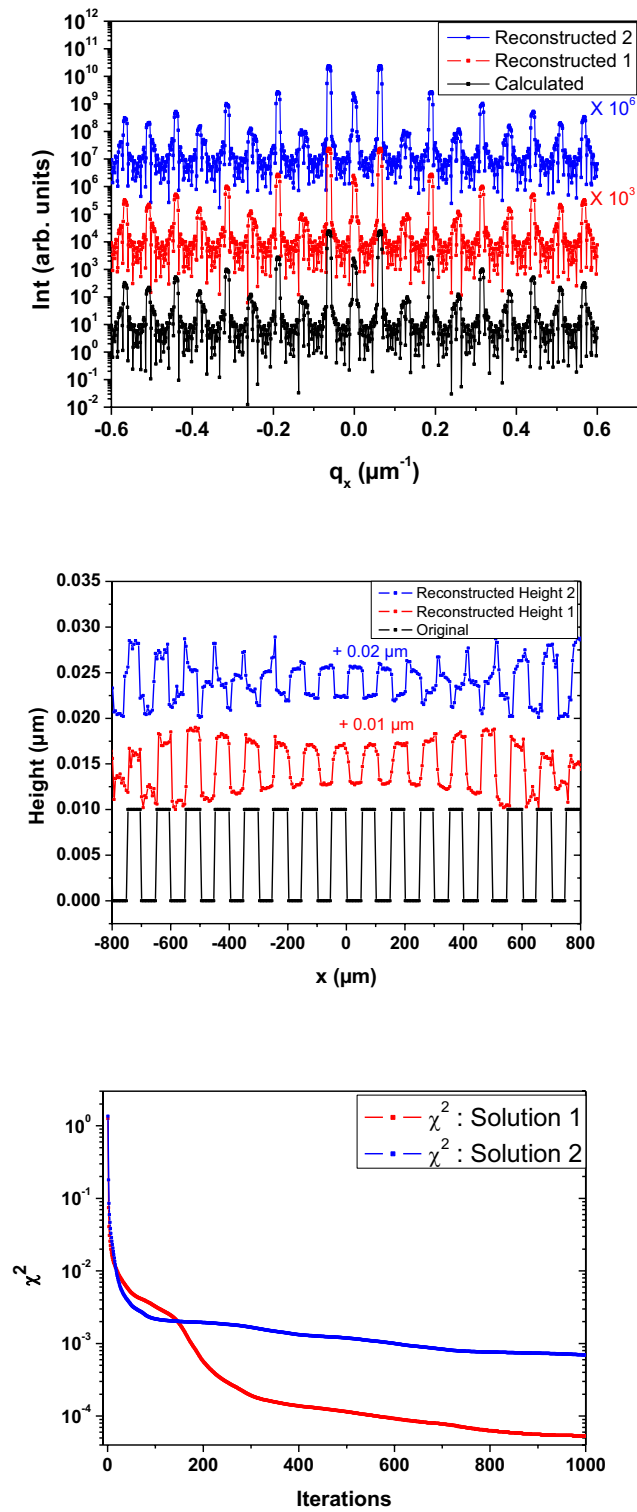


Fig. 5.18 Surface height reconstruction for a model surface in the form a grating with period  $100 \mu\text{m}$  and depth  $10 \text{ nm}$ . The algorithm mentioned in equations (5.50)-(5.55) is used to retrieve the surface profile. The final results are shown for two solutions with different set of initial phases.



The quality of the reconstruction is quantified by calculating the quantity  $\chi^2$ , as in equation (5.6),

$$\chi^2 = \frac{\sum_j \{|G'_k(q_x)| - |A(q_x)|\}^2}{\sum_j |A(q_x)|^2} \quad (5.56)$$

The quantity  $\chi^2$  is below  $10^{-4}$  for the first attempt but for the second attempt it is  $\sim 10^{-3}$  in 1000 iterations. The convergence of the algorithm depends on the initial random set of phases provided in each attempt. It is clear from the two attempts in Fig. 5.18 for reconstructed surface profile that the solution is not unique. Although the value of  $\chi^2$  is sufficiently small, the reconstructed surface profile is far from satisfactory. Also for every different set of initial random phases the algorithm gives different solution and it cannot approach any unique solution. This has been verified by running the algorithm several times with different set of initial phases for  $\sim 1000$  iterations.

The algorithm mentioned in equations (5.50)-(5.55) is now modified to include the phase of the illumination function and quadratic phase term of the propagator. With the additional phase information the algorithm is expected to approach a converging solution. The steps in the algorithm are as follows:

Start with the random phases in the interval  $[-\pi, \pi]$  in the sample plane

$$\varphi_1 = \text{rand} [-\pi, \pi] \quad (5.57)$$

- (i) Replace the modulus of the estimate by the modulus of the illumination function and add the phase of illumination function  $\varphi_F$  and 1D propagator phase term  $\Phi_P^1$  in the estimated phase

$$g'_k(x) = |B(x)| \exp(-i(\varphi_k + \varphi_F + \Phi_P^1)) \quad (5.58)$$

- (ii) Fourier transform this estimate of the scatterer to get the scattering amplitude

$$G'_k(q_x) = |G'_k(q_x)| \exp(i\Phi'_k) = \mathcal{F}(g'_k(x)) \quad (5.59)$$

- (iii) Replace the modulus of the scattering amplitude by the modulus of the calculated amplitude  $|A(q_x)|$ ,

$$G_k(q_x) = |A(q_x)| \exp(-i\Phi'_k(q_x)) \quad (5.60)$$

- (iv) Fourier transform the estimate of the scattering amplitude. The phase for the next iteration is obtained by subtracting the phase of illumination function  $\varphi_F$  and 1D propagator phase term  $\Phi_P^1$  from the phase of the real space estimate

$$g_k(x) = |g_k(x)| \exp(-i\varphi_k) = \mathcal{F}^{-1}(G_k(q_x)) \quad (5.61)$$

$$\varphi_{k+1} = \varphi_k - \varphi_F - \Phi_P^1 \quad (5.62)$$

$$h_{k+1}(x) = \varphi_{k+1}/q_z \quad (5.63)$$

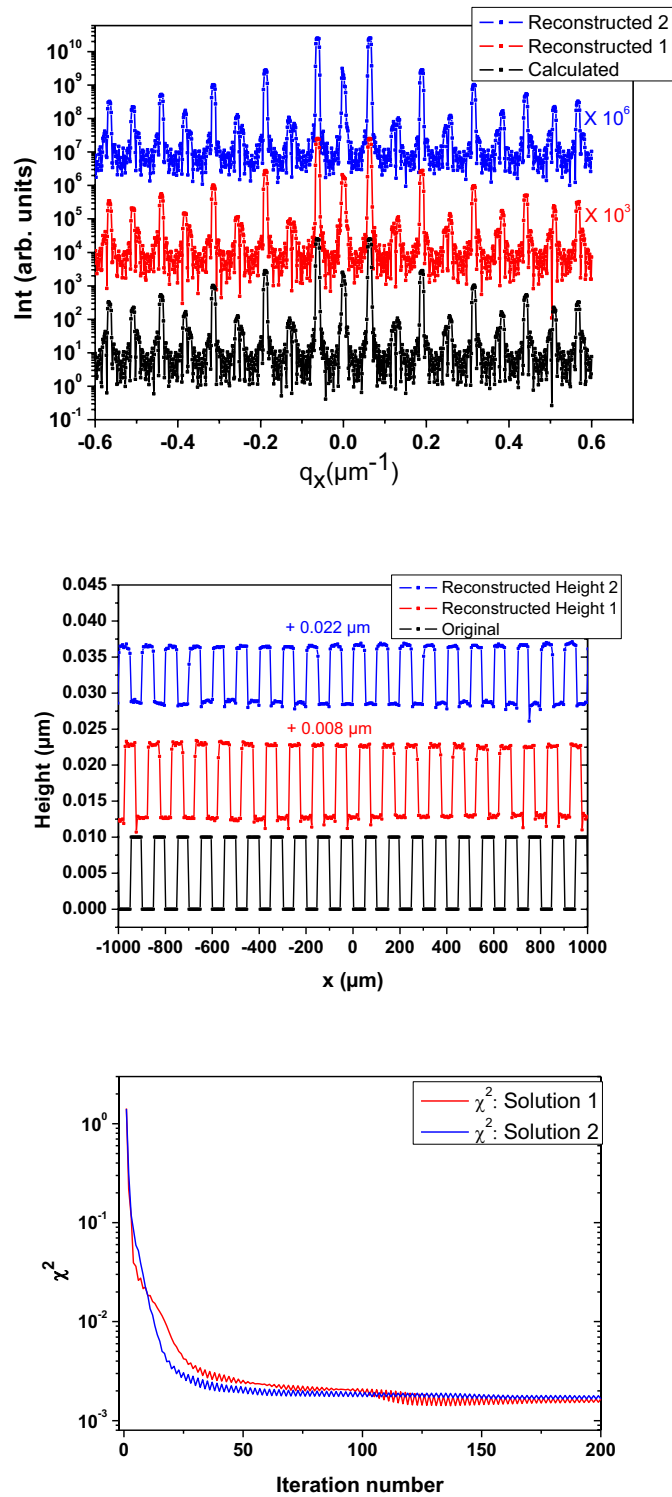


Fig. 5.19 Surface height reconstruction for a model surface in the form a grating with period  $100 \mu\text{m}$  and depth  $10 \text{ nm}$ . The algorithm mentioned in equations (5.57)-(5.63) is used to retrieve the surface profile. The final results (red and blue) are shown for two solutions with different set of initial phases

The reconstruction of the surface profile (Fig. 5.19 middle) with modified algorithm looks promising. The reconstructed solutions (red and blue) can be observed to have almost the same periodicity of  $100 \mu\text{m}$  as the test structure (black) irrespective of different starting phase. Although, the lateral position of the height profile for solutions differs. This might be due to different starting phases for each of the solution. There is influence of the local height difference between the trough and the crest of the grating for the reconstructed solution because of this. The local height difference reconstructed for the solution 2 (blue) is  $\sim 8 \text{ nm}$  compared to  $\sim 10 \text{ nm}$  for the solution 1 (red) which is more correct as the height difference between the trough and the crest is  $10 \text{ nm}$ . The value of  $\chi_{min}^2$  (Fig. 5.19 lower) reaches a minimum  $\sim 9 \times 10^{-2}$  for both the solutions (red and blue) irrespective of different initial phases. It has been verified that the value of  $\chi_{min}^2$  remains stable at  $\sim 9 \times 10^{-2}$  for the solutions (not shown here) with different starting phase for each. This indicates the good agreement between the reconstructed intensities (red and blue in Fig. 5.19 upper) and the calculated intensity for the model surface. The value of  $\chi_{min}^2 \sim 9 \times 10^{-2}$  in this case (Fig. 5.19) with modified algorithm is larger than the value of  $\chi_{min}^2$  with the conventional GS algorithm (Fig. 5.18) where it can reach a value below  $10^{-4}$  for some cases (Solution 1 in Fig. 5.18). But the agreement of the reconstructed height profile with the test structure (Fig. 5.19 middle) is far better with the modified algorithm than that with the conventional GS algorithm (Fig. 5.18 middle). This justifies the use of the modified algorithm (equations 5.57-5.63) for the reconstruction of height profile from the measured scattering data from the surfaces without any a priori information. It is presented in the next chapter in details.

## 5.6 References

- [5.1] U. Pietsch, T. Baumbach, V.Holy, *High-Resolution X-Ray Scattering From Thin Films to Lateral Nanostructures*, Springer-Verlag, ISBN 0387400923, (2004).
- [5.2] S.K. Sinha, M. Tolan, A. Gibaud, *Effect of partial coherence on the scattering of x rays by matter*, Phys. Rev. B 57, 2470-2758, (1998).

- [5.3] M. Tolan, S.K. Sinha, *X-ray scattering with partial coherent radiation: The exact relationship between “resolution” and “coherence”*, Physica 248, 399-404, (1998).
- [5.4] M. Born, E. Wolf, *Principles of Optics*, 7th edition, Cambridge University Press (2005)
- [5.5] T. Panzner, G. Gleber, T. Sant, W. Leitenberger, U. Pietsch, *Coherence experiments at the white-beam beamline of BESSYII*, Thin Solid Films 515, 5563-5567 (2007)
- [5.6] G. J. Williams, M. A. Pfeifer, I. A. Vartanyants and I. K. Robinson, *Internal structure in small Au crystals resolved by three-dimensional inversion of coherent x-ray diffraction*, Phys. Rev. B 73, 094112, (2006).
- [5.7] J. Miao, Y. Nishino, Y. Kohmura, B. Johnson, C. Song, S. H. Risbud and T. Ishikawa, *Quantitative image reconstruction of GaN quantum dots from oversampled diffraction intensities alone*, Phys. Rev. Lett 95, 085503-1-4, (2005).
- [5.8] I.A. Vartanyants, J.A. Pitney, J.L. Libbert, I.K. Robinson, *Reconstruction of surface morphology from surface reflectivity*, Phys. Rev. B 55, 13193, (1997).
- [5.9] I.K. Robinson, J.L. Libbert, I.A. Vartanyants, J.A. Pitney, D.M. Smilgies, D.L. Abernathy and G. Grübel, *Coherent x-ray diffraction imaging of silicon oxide growth*, Phys. Rev. B 60, 9965 (1999).
- [5.10] X. Xiao and Q. Shen, *Wave propagation and phase retrieval in Fresnel diffraction by a distorted-object approach*, Phys. Rev. B 72, 033103 (2005).
- [5.11] X. Xiao, M.D. de Jonge, Y. S. Chu, Q. Shen, *A unified phase retrieval algorithm for both far-field and near-field diffractive imaging*, Proc. Of SPIE 6316, 63160F (2006).

## Chapter 6

# Surface height profile reconstruction from the measured surface speckle data

After the successful reconstruction of the model surface profile (Fig. 5.19) the modified GS algorithm (equations (5.57) to (5.63)) can now be applied to reconstruct surface height profile from the measured speckle data.

### 6.1 Reconstruction of surface profile from selected measurements

The measured scattering data from various surfaces as discussed in Chapter 4 is used for the reconstruction. The scattered intensity scan at a particular energy is extracted from the recorded reciprocal space map. The algorithm is applied for 200 iterations starting with an initial random guess for the phase. Then 100 cycles of such 200 iterations are applied with different initial random phases for each cycle. The average of solutions of surface height profiles for 100 cycles is considered as the final solution for surface height profile. Two such final solutions for surface height profile are calculated for the selected energy for various reciprocal space map measurements.

Following is the discussion on the calculations performed to simulate measured scattered intensity for some selected measurements discussed in Chapter 4.

### 6.1.1 GaAs plain wafer $\alpha_i = 0.2^\circ$

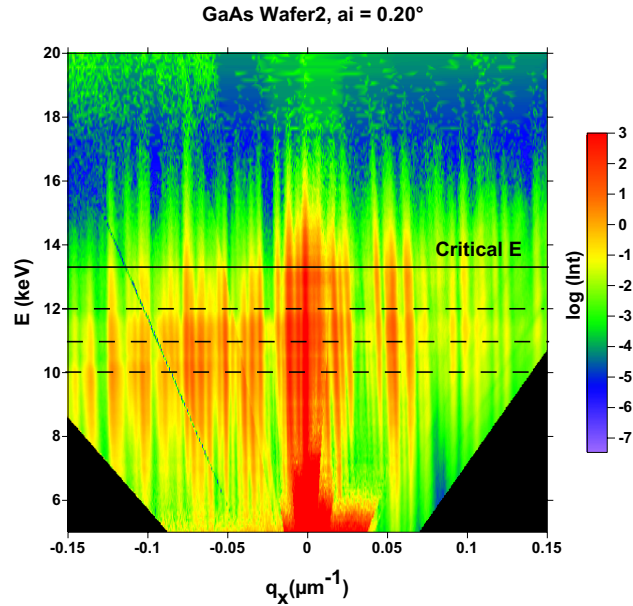


Fig. 6.1 Measured reciprocal space map in  $(q_x, E)$  space for GaAs plain wafer at  $\alpha_i = 0.2^\circ$ . The black horizontal line indicates the critical energy ( $E_c = 13.28 \text{ keV}$ ) for GaAs at  $\alpha_i = 0.2^\circ$ . The dashed black lines mark the selected energies ( $E = 10, 11$  and  $12 \text{ keV}$ ).

Fig. 6.1 shows the reciprocal space map measurement plotted in  $(q_x, E)$  space for GaAs plain wafer (Fig. 4.3-4.4). The  $q_x$  – scans over  $q_x$  range of  $q_x = \pm 0.15 \mu\text{m}^{-1}$  are extracted at  $E = 10 \text{ keV}, 11 \text{ keV}, 12 \text{ keV}$  (shown by dashed black lines in Fig. 6.1) which lie in the energy range of the maximum in the scattered intensity. All the selected energies (10, 11 and 12 keV) lie below the critical energy ( $E_c = 13.28 \text{ keV}$ ) for total external reflection for GaAs at  $\alpha_i = 0.2^\circ$ . For the energies above this energy range the measured scattering intensity is very weak and for the lower energies than this range the forbidden region for  $q_x > 0$  increases. Even at  $E = 10 \text{ keV}$ , the scattering is not accessible for  $q_x \gtrsim +0.14 \mu\text{m}^{-1}$ . The selected energy range is a tradeoff between the region with measurable intensity and the region over which the scattering is not forbidden.

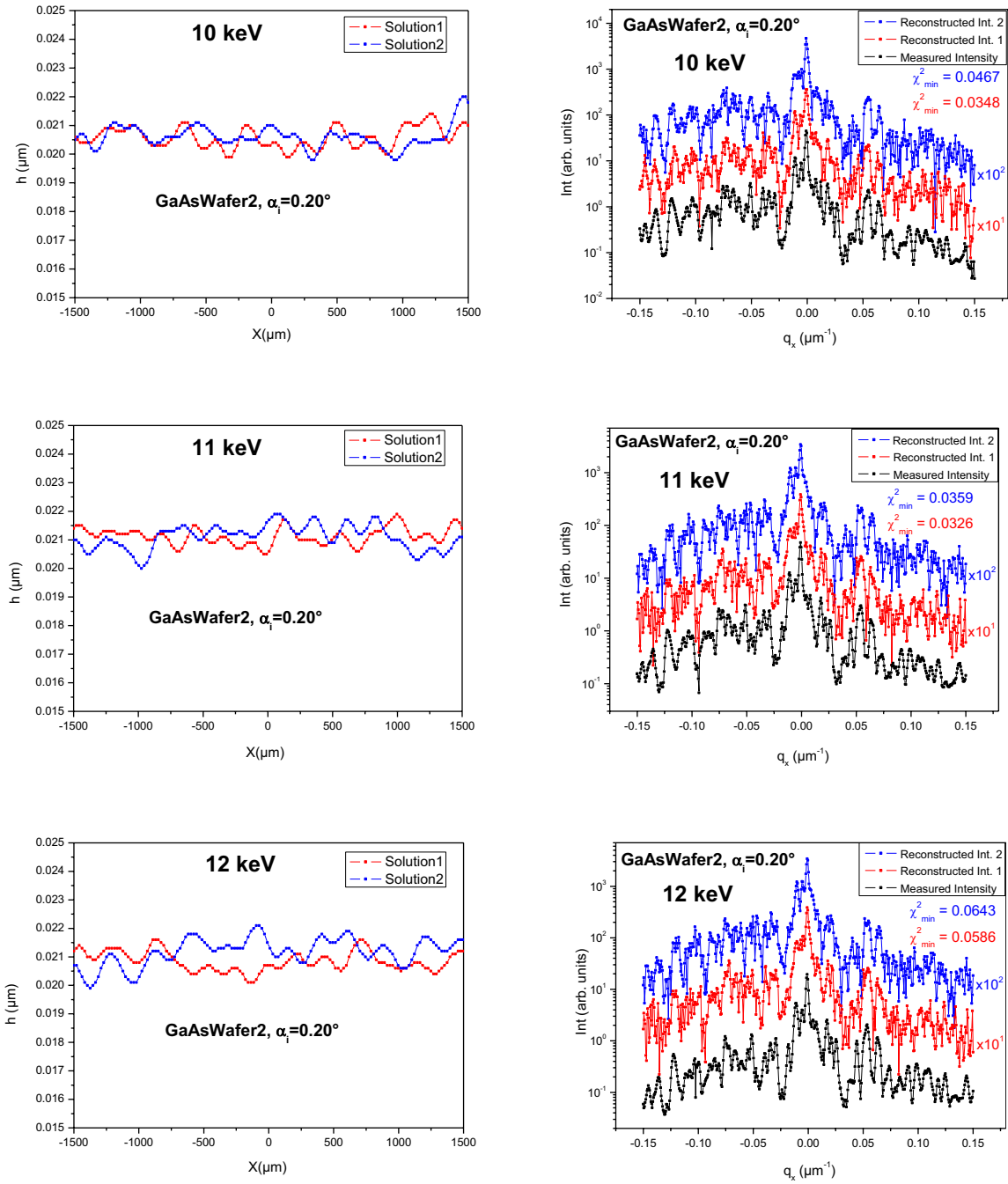


Fig. 6.2 Reconstructed surface height solutions and reconstructed intensity profiles along with measured intensity  $q_x$  scan for the reciprocal space map for GaAs plain wafer at  $E = 10, 11$  and  $12$  keV. The reconstructed intensities (red and blue) are plotted with certain vertical offset along intensity axis. The respective value of  $\chi^2_{min}$  for each fit of the reconstructed intensity to the measured one is mentioned alongside.

Fig. 6.2 (left) shows two solutions (red and blue) of reconstructed surface height profile and the respective reconstructed intensity patterns at different selected energies (10, 11 and 12 keV). The corresponding reconstructed intensity patterns (red and blue in right of Fig. 6.2)



show good fit with the measured intensity pattern over both the long and the short scales of  $q_x$ . There is not much qualitative difference in the solutions of reconstructed surface height profiles at different selected energies (10, 11 and 12 keV) as the x-rays are sensitive only to the surface of the sample for all the selected energies. The distribution of local maxima and minima for solutions for surface profile varies at different selected energies but the surface height remains in the range of  $\sim 20$  to  $22$  nm. The local maxima have average width of  $\sim 100$   $\mu\text{m}$ . The spatial resolution ( $\Delta x$ ) achieved in the reconstructed surface profile depends on the measured  $q_x$  – range

$$\Delta x = \frac{2\pi}{|q_{x,max} - q_{x,min}|} \quad (6.1)$$

For the measured  $q_x$  – range of  $\pm 0.15 \mu\text{m}^{-1}$ , the spatial resolution achieved is  $\sim 21 \mu\text{m}$ .

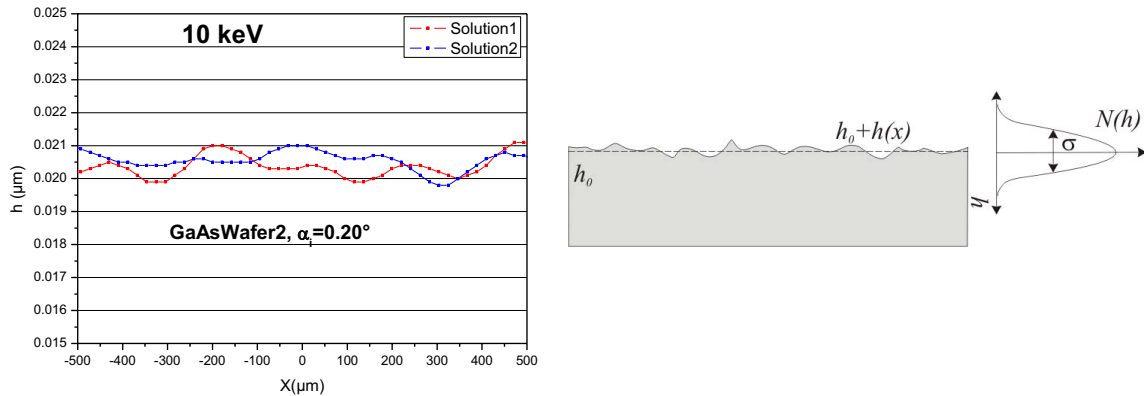


Fig. 6.3 Reconstructed surface height solutions in a selected range ( $x = -500 \mu\text{m}$  to  $+500 \mu\text{m}$ ) for GaAs plain wafer at  $E = 10 \text{ keV}$ . Schematic diagram of rough surface (right) is shown with mean arbitrary height  $h_0$  and the local height function  $h(x)$ . The surface height can be considered to follow a Gaussian distribution with half width  $\sigma$ .

The set of solutions for  $E = 10 \text{ keV}$  is discussed in detail. Fig. 6.3 (left) shows the selected part of the reconstructed surface profiles over 1 mm for 10keV. The surface height profile is the variation in the local height  $h(x)$  with the mean arbitrary surface height  $h_0$ . The distribution of local surface height can be considered to be Gaussian with half width of  $\sigma$ . The surface can be observed to be fairly flat over a typical lateral range of  $200 \mu\text{m}$ . The solution number 2 (blue) is flat with surface height of  $20.5 \text{ nm}$  over a wide range of  $300 \mu\text{m}$  between the lateral positions of  $x = -100 \mu\text{m}$  to  $-400 \mu\text{m}$ . The surface height varies by

only 0.5 nm for the lateral positions of  $x = -500 \mu\text{m}$  to  $-400 \mu\text{m}$  and  $x = -100 \mu\text{m}$  to  $+200 \mu\text{m}$ . Beyond  $x = +200 \mu\text{m}$  a minimum can be observed at  $x = +300 \mu\text{m}$  with surface height of 19.8 nm. The surface height can be observed to be gradually growing after  $x = +300 \mu\text{m}$  and reaches saturates to  $\sim 20.8$  nm. The variation in surface height is more in solution 1 (red) than in solution 2 (blue). The surface height remains constant with surface height of 20.5 nm (again) over a lateral range of  $x = -100 \mu\text{m}$  to  $+100 \mu\text{m}$  and varies by 0.5 nm till  $x = +400 \mu\text{m}$  and then varies by 1 nm till  $x = +500 \mu\text{m}$ . For lateral positions  $x = -500 \mu\text{m}$  to  $-100 \mu\text{m}$  the variation in the surface height is nearly 1 nm with a minimum at  $x = -300 \mu\text{m}$ .

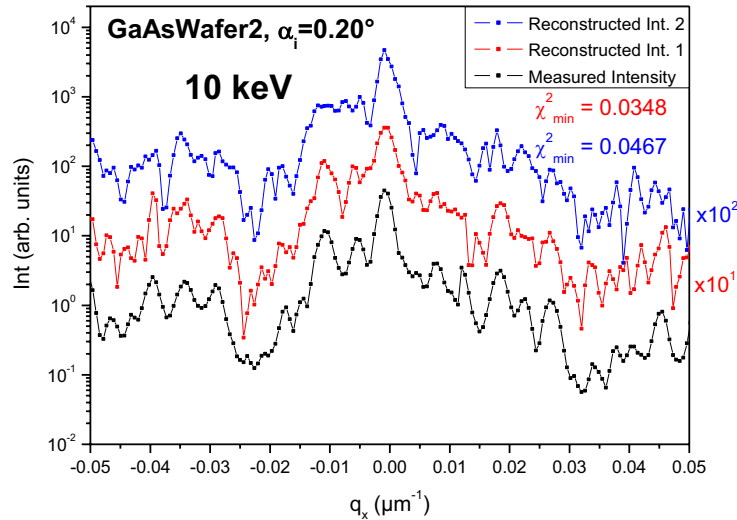


Fig. 6.4 Reconstructed surface intensity profiles along with measured intensity  $q_x$  scan for the reciprocal space map in a selected range ( $q_x = -0.05$  to  $+0.05 \mu\text{m}^{-1}$ ) for GaAs plain wafer at  $E = 10 \text{ keV}$ . The reconstructed intensities (red and blue) are plotted with certain vertical offset along intensity axis. The respective value of  $\chi_{min}^2$  for each fit of the reconstructed intensity to the measured one is mentioned alongside.

The reconstructed intensity patterns at 10keV (red and blue curves in Fig. 6.4) show good fit with the measured intensity pattern (black curve) over both the long and the short scales of  $q_x$ . The fit at the specular position ( $q_x = 0$ ) is better than the fit at other local maxima. The fit for the intensity is poor at where the variation of intensity is not sharp, for example in the range  $q_x = -0.025$  to  $-0.015 \mu\text{m}^{-1}$  and  $q_x = +0.03$  to  $+0.05 \mu\text{m}^{-1}$ . Also the reconstructed intensity patterns exhibit local minima with local intensity less the measured one, for example at  $q_x = -0.026 \mu\text{m}^{-1}$  for intensity solution 1 (red) and at  $q_x = +0.038 \mu\text{m}^{-1}$  for intensity solution 2 (blue).

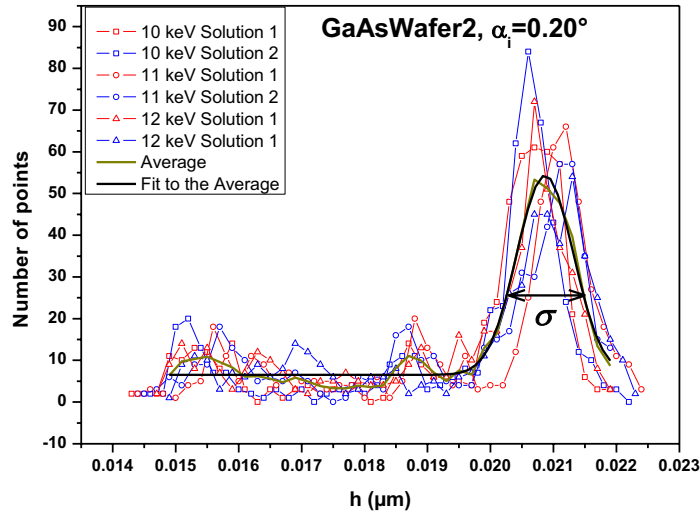


Fig. 6.5 Distribution of surface height for two different reconstructed solutions at  $E = 10, 11$  and  $12 \text{ keV}$ . The thick dark yellow line is the average of the distributions for all the solutions. The thick black line is the Gaussian fit to the average with half width  $\sigma$ .

The quality of the reconstruction is tested by calculating the distribution of local height for the reconstructed surface height solutions at different selected energies. As seen in Fig. 6.5 the distribution looks almost similar for all the solutions at different selected energies. The surface height varies from  $\sim 14.3 \text{ nm}$  to  $\sim 22.4 \text{ nm}$ . The lower surface heights below  $19 \text{ nm}$  fall beyond the footprint region with lateral positions  $x = -1500 \mu\text{m}$  to  $+1500 \mu\text{m}$ , hence not shown in the reconstructed surface profiles in Fig. 6.2 (left). These lower values of surface heights are considered to get enough statistical data for surface height distribution. The distribution of local height on the surface varies from solution to solution but the peak is observed for all the distributions for different solutions at  $\sim 21 \text{ nm}$  with average number of 60 points (except solution 2 at  $10 \text{ keV}$ ). The average of all the distributions (thick dark yellow line) for all the solutions for the selected energies is calculated and fitted with Gaussian (thick black line). The Gaussian fit has the maximum at  $20.8 \text{ nm}$  with half width of  $0.9 \text{ nm}$ . The width at half of the maximum can be considered as roughness of the surface. The average roughness of the GaAs plain wafer, from Fig. 6.5, can be said to be  $\sigma \sim 1 \text{ nm}$  at different energies. The roughness is in agreement with the roughness found in polished semiconducting surfaces (Si wafer) by other techniques like light scattering topography, x-ray reflectivity and atomic force microscopy measurements [6.1] which is reported to be  $\sim 1 \text{ nm}$ . Although the results for the roughness reported in Ref. [6.1] cannot be directly compared, the value of the roughness observed ( $\sim 1 \text{ nm}$ ) seems realistic.

### 6.1.2 GaAs Grating at $\alpha_i = 0.1^\circ$

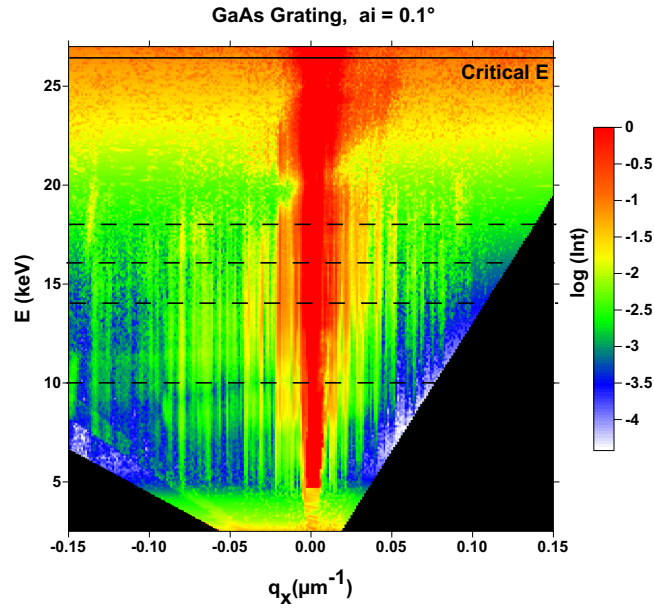


Fig. 6.6 Measured reciprocal space map in  $(q_x, E)$  space. The complete measured energy range lies below the critical energy ( $E_c = 26.62 \text{ keV}$ ) for GaAs at  $\alpha_i = 0.1^\circ$ . The dashed black lines mark the selected energies ( $E = 10, 14, 16$  and  $18 \text{ keV}$ ).

Fig. 6.6 shows the reciprocal space map measurement plotted in  $(q_x, E)$  space for GaAs grating with effective period of  $47 \mu\text{m}$  with angle of incidence of  $\alpha_i = 0.1^\circ$  (Fig. 4.8(B)). The  $q_x$  – scans over  $q_x$  range of  $q_x = \pm 0.15 \mu\text{m}^{-1}$  are extracted at  $E = 10 \text{ keV}, 14 \text{ keV}, 16 \text{ keV}$  and  $18 \text{ keV}$  which lie in the energy range of the maximum in the scattered intensity. With the critical energy of  $E_c = 26.62 \text{ keV}$  for GaAs at  $\alpha_i = 0.1^\circ$ , the complete measured energy range lies below the critical energy and the total external reflection of the x-ray beam occurs for all the measured energies. Large part of the scattering at  $E = 10 \text{ keV}$  is not accessible for  $q_x \gtrsim 0.077 \mu\text{m}^{-1}$  thus the effective range for the measured scattering reduces to  $q_x = -0.15$  to  $+0.077 \mu\text{m}^{-1}$  from the complete range of  $q_x = -0.15$  to  $+0.15 \mu\text{m}^{-1}$ . The non-accessible region reduces further for higher energies and at  $E = 18 \text{ keV}$  the scattering is not accessible for  $q_x \gtrsim 0.14 \mu\text{m}^{-1}$ .

## Surface height profile reconstruction from the measured surface speckle data

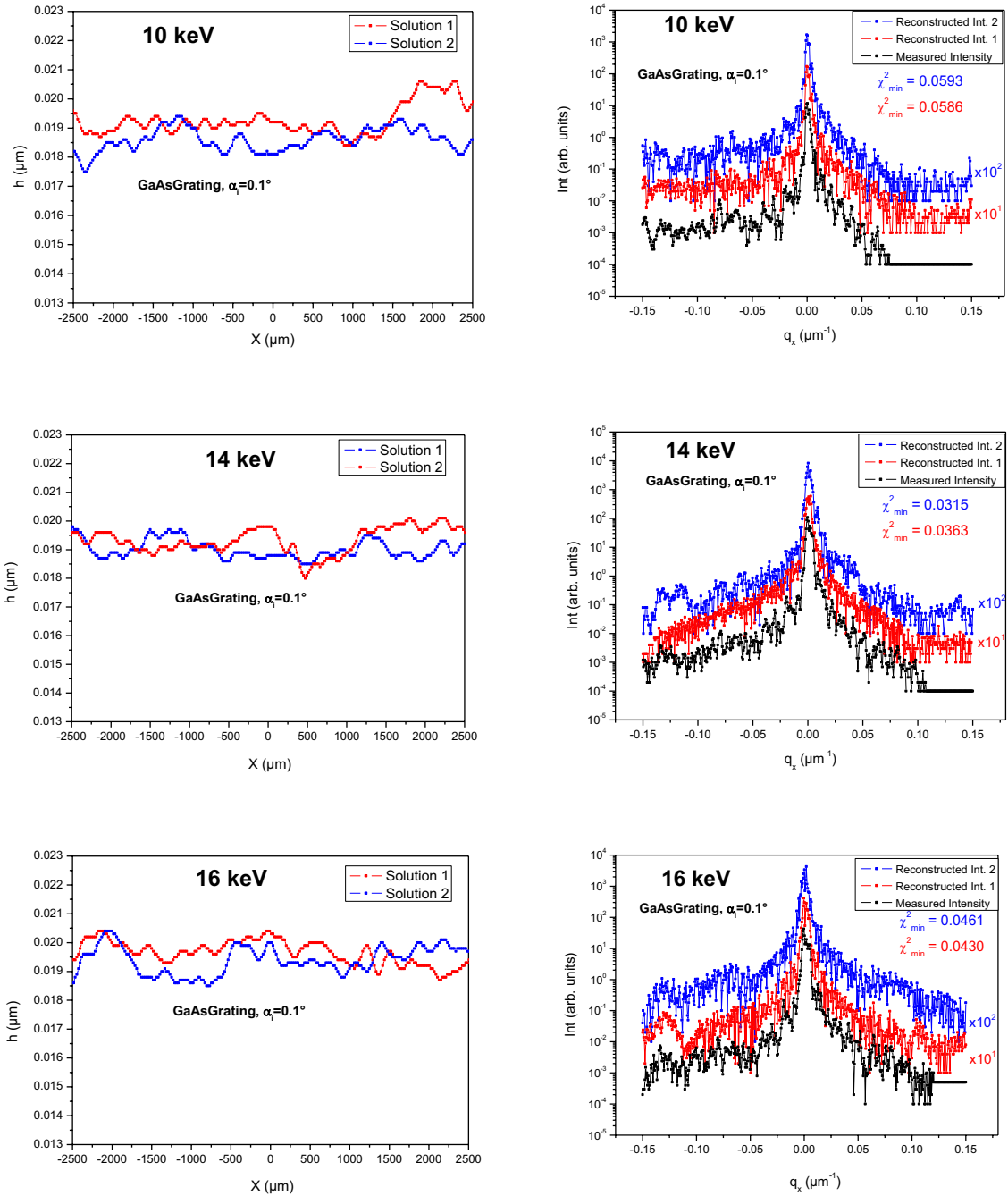


Fig. 6.7 Reconstructed surface height solutions and reconstructed intensity profiles along with measured intensity  $q_x$  scan for the reciprocal space map for GaAs grating at  $E = 10, 14$  and  $16$  keV. The reconstructed intensities (red and blue) are plotted with certain vertical offset along intensity axis. The respective value of  $\chi^2_{\min}$  for each fit of the reconstructed intensity to the measured one is mentioned alongside.

## Surface height profile reconstruction from the measured surface speckle data

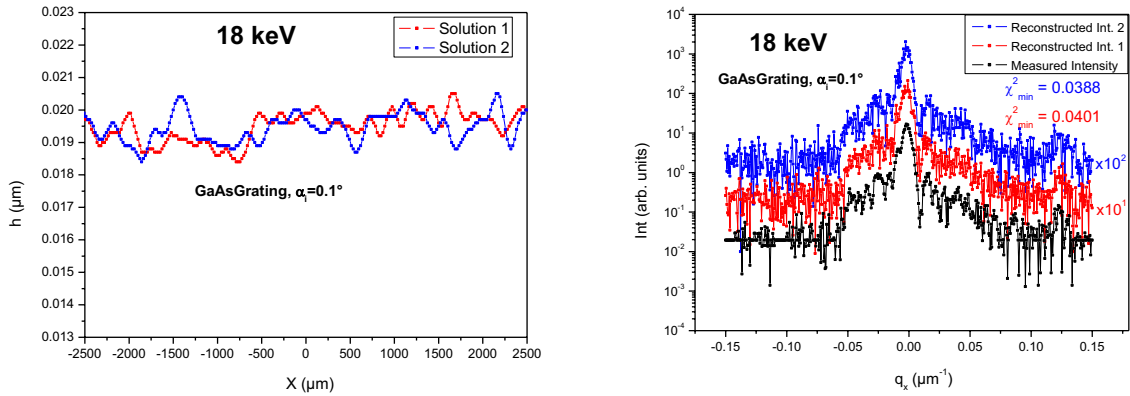


Fig. 6.8 Reconstructed surface height solutions and reconstructed intensity profiles along with measured intensity  $q_x$  scan for the reciprocal space map for GaAs grating at  $E = 18 \text{ keV}$ . The reconstructed intensities (red and blue) are plotted with certain vertical offset along intensity axis. The respective value of  $\chi_{min}^2$  for each fit of the reconstructed intensity to the measured one is mentioned alongside.

The reconstructed surface profiles (Fig. 6.7, Fig. 6.8 left) exhibit only the long range ordering or the surface roughness over the long lateral range of the sample. The reconstructed surface profile does not show any grating like pattern. The main reason is the lack of distinct grating peaks in the measurement. Also with the measured  $q_x$  – range of  $\pm 0.15 \mu\text{m}^{-1}$ , the spatial resolution (using equation 6.1) achieved is  $\sim 21 \mu\text{m}$ . With this spatial resolution it is hard to reconstruct the grating like pattern in the reconstructed surface profile as the effective grating period of  $47 \mu\text{m}$  makes only about 2 points on the reconstructed surface profile.

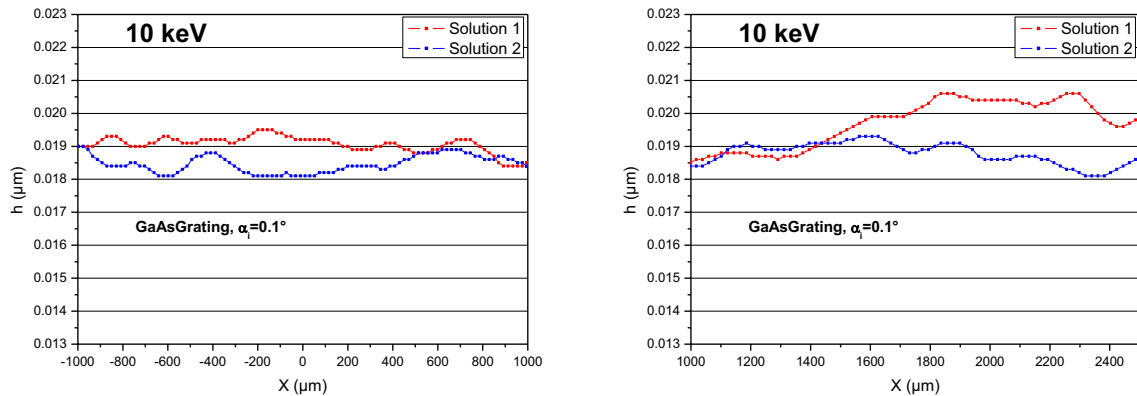


Fig. 6.9 Reconstructed surface height solutions in two selected ranges for GaAs surface grating at  $E = 10 \text{ keV}$ .

The set of solutions for  $E = 10 \text{ keV}$  is discussed in detail. Fig. 6.9 shows the reconstruction surface profile solutions at 10keV. The surface height in solution 1 (red) can be observed to be almost flat with mean surface height of 19.2 nm over wide lateral range of

$x = -1000 \mu\text{m}$  to  $+800 \mu\text{m}$  with variations of around  $0.6 \text{ nm}$ . Beyond  $x = +800 \mu\text{m}$  the surface height decreases gradually till  $+1000 \mu\text{m}$ . The surface height then increases further till  $x = +1800 \mu\text{m}$  and remains  $20.5 \text{ nm}$  and reduces again to  $19.8$  for  $x = +2400 \mu\text{m}$ . Thus the variation of about  $1.6 \text{ nm}$  is observed in solution 1 over  $5 \text{ mm}$  of the sample surface. Variation of surface height in solution 2 (blue) is from  $17.5 \text{ nm}$  to  $19 \text{ nm}$  over lateral distance of  $5 \text{ mm}$  on the sample surface.

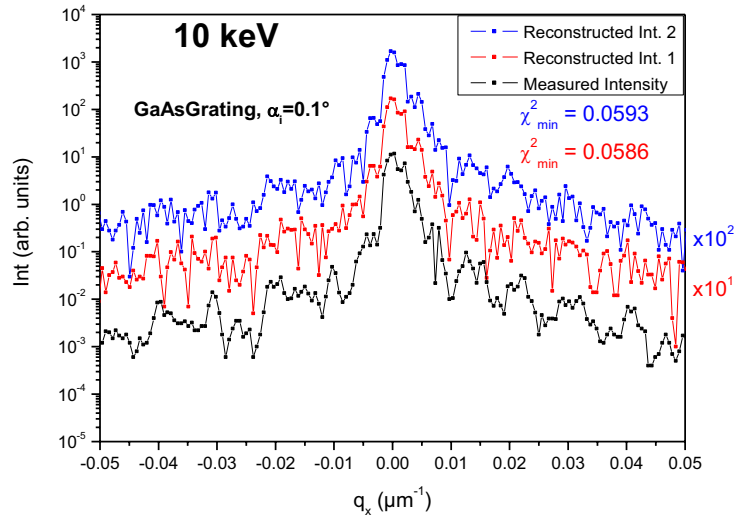


Fig. 6.10 Reconstructed intensity profiles along with measured intensity  $q_x$  scan for the reciprocal space map in a selected range for GaAs surface grating at  $E = 10 \text{ keV}$ . The reconstructed intensities (red and blue) are plotted with certain vertical offset along intensity axis. The respective value of  $\chi_{min}^2$  for each fit of the reconstructed intensity to the measured one is mentioned alongside.

Fig. 6.10 shows the selected part of the reconstructed intensity profiles (red and blue) with the measured intensity  $q_x$  scan (black) for the reciprocal space map for GaAs surface at  $E = 10 \text{ keV}$ . The reconstructed profiles fit well over the whole range at specular position ( $q_x = 0$ ) but the fit is poor at various other local maxima. There is not fit at  $q_x = -0.005 \mu\text{m}^{-1}$ , although the shape of the local maximum is correctly reconstructed. Also the algorithm cannot find the fit for intensities at some local minima, for example at  $q_x = -0.01 \mu\text{m}^{-1}, -0.028 \mu\text{m}^{-1}, +0.023 \mu\text{m}^{-1}, -0.043 \mu\text{m}^{-1}$ .

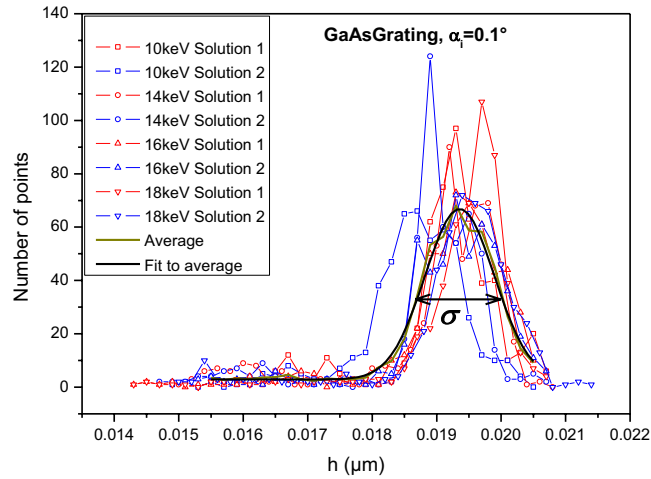


Fig. 6.11 Distribution of surface height for two different reconstructed solutions at  $E = 10, 14, 16$  and  $18$  keV. The thick dark yellow line is the average of the distributions for all the solutions. The thick black line is the Gaussian fit to the average with half width  $\sigma$ .

Fig. 6.11 shows the distribution of local height for both the solutions at different selected energies. The local height varies from  $\sim 14.2$  nm to  $\sim 21.4$  nm. The lower surface heights from  $\sim 14.2$  nm to  $\sim 18$  nm fall beyond the footprint region with lateral positions  $x = -2500 \mu\text{m}$  to  $+2500 \mu\text{m}$ , hence not shown in the reconstructed surface profiles in Fig. 6.7 (left). The average of all the distributions (thick dark yellow line) for all the solutions for the selected energies is calculated and fitted with Gaussian (thick black line). The Gaussian fit has the maximum at 19.9 nm with half width of 1.1 nm. Although the grating like features in the surface profile cannot be reconstructed from the measured data due to the lack of grating peaks, the average roughness of the grating surface can be said to be  $\sigma \sim 1$  nm from the average of the all the distributions. The distributions for few solutions like solution 2 at 10 keV, solution 2 at 14 keV and solution 1 at 18 keV show peak at different local height.



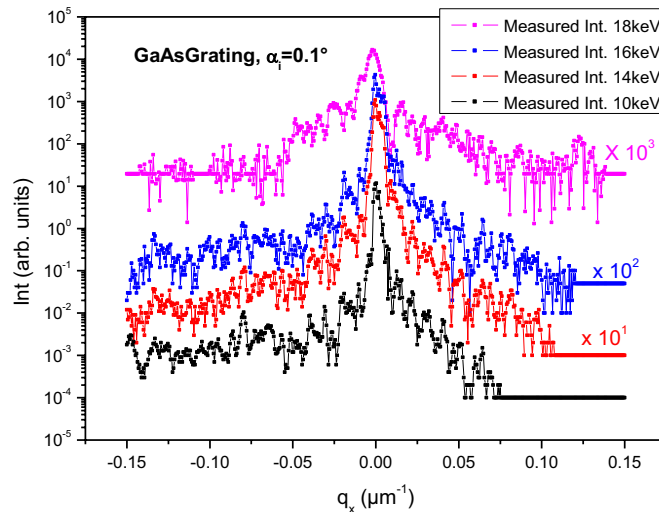


Fig. 6.12 Comparison of measured intensity  $q_x$  scans at different selected energies ( $E = 10, 14, 16, 18 \text{ keV}$ ). The intensities at different energies are plotted with certain vertical offset along intensity axis.

The main reason for this might be due to different accessible  $q_x$  ranges at different selected energies (Fig. 6.12). The maximum accessible  $q_x$  ranges from  $q_x = +0.077 \mu\text{m}^{-1}$  at  $E = 10 \text{ keV}$  to  $q_x = 0.14 \mu\text{m}^{-1}$  at  $E = 18 \text{ keV}$ . The intensity patterns for  $q_x < 0$  for different energies are nearly similar. Whereas the intensity patterns in the region for  $q_x > 0$  are much different as can be seen in Fig 6.11 or in the reciprocal space map in Fig. 6.5. The finiteness of the measured data to different extents gives rise to high spatial-frequency features in the reconstructed surface height solutions which do not correspond to the real physical nature of the surface.

### 6.1.3 GaAs Grating $\alpha_i = 0.25^\circ$

Fig. 6.13 shows the reciprocal space map measurement plotted in  $(q_x, E)$  space for GaAs grating with effective period of  $88 \mu\text{m}$  with angle of incidence of  $\alpha_i = 0.25^\circ$  (Fig. 4.8(B)). The  $q_x$  - scans over  $q_x$  range of  $q_x = \pm 0.20 \mu\text{m}^{-1}$  are extracted at  $E = 10 \text{ keV}, 12 \text{ keV}, 15 \text{ keV}$  and  $16 \text{ keV}$  which lie in the energy range of the maximum in the scattered intensity. With the critical energy of  $E_c = 10.62 \text{ keV}$  for GaAs at  $\alpha_i = 0.25^\circ$ , the only scan which for which x-rays experience total external reflection is the scan at  $E = 10 \text{ keV}$ .

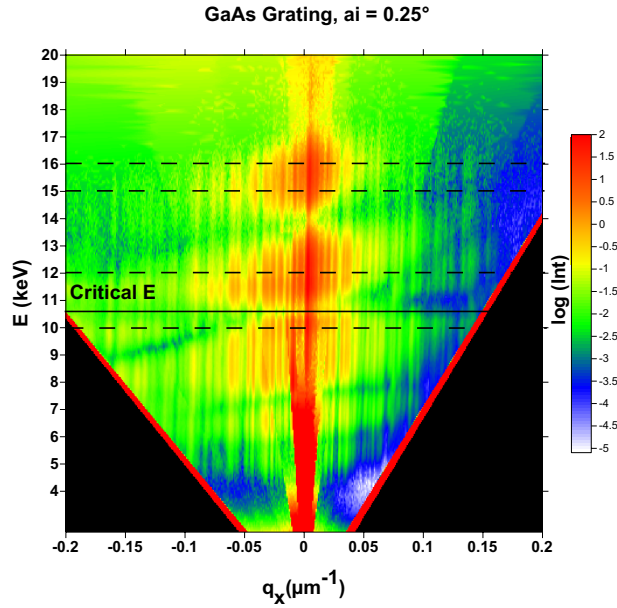


Fig. 6.13 Measured reciprocal space map in  $(q_x, E)$  space for GaAs grating at  $\alpha_i = 0.25^\circ$ . The black horizontal line indicates the critical energy ( $E_c = 10.62 \text{ keV}$ ) for GaAs at  $\alpha_i = 0.25^\circ$ . The dashed black lines mark the selected energies ( $E = 10, 12, 15$  and  $16 \text{ keV}$ ).

Large part of the scattering at  $E = 10 \text{ keV}$  is not accessible due to forbidden region for  $q_x \gtrsim 0.14 \mu\text{m}^{-1}$  thus the effective range for the measured scattering reduces to  $q_x = -0.20$  to  $+0.14 \mu\text{m}^{-1}$  from the complete range of  $q_x = -0.2$  to  $+0.2 \mu\text{m}^{-1}$ . The non-accessible region reduces further for higher energies and at  $E = 12 \text{ keV}$  the scattering is not accessible for  $q_x \gtrsim 0.16 \mu\text{m}^{-1}$ . For still higher energies  $15 \text{ keV}$  and  $16 \text{ keV}$  the complete  $q_x$  range of  $-0.2$  to  $+0.2 \mu\text{m}^{-1}$  can be observed.

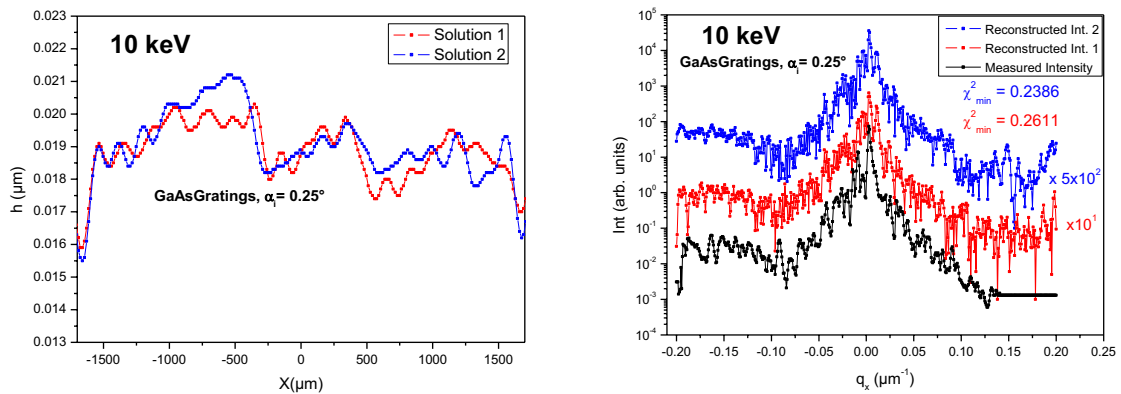


Fig. 6.14 Reconstructed surface height solutions and reconstructed intensity profiles along with measured intensity  $q_x$  scan for the reciprocal space map for GaAs grating at  $E = 10 \text{ keV}$ . The reconstructed intensities (red and blue) are plotted with certain vertical offset along intensity axis. The respective value of  $\chi_{min}^2$  for each fit of the reconstructed intensity to the measured one is mentioned alongside.

## Surface height profile reconstruction from the measured surface speckle data

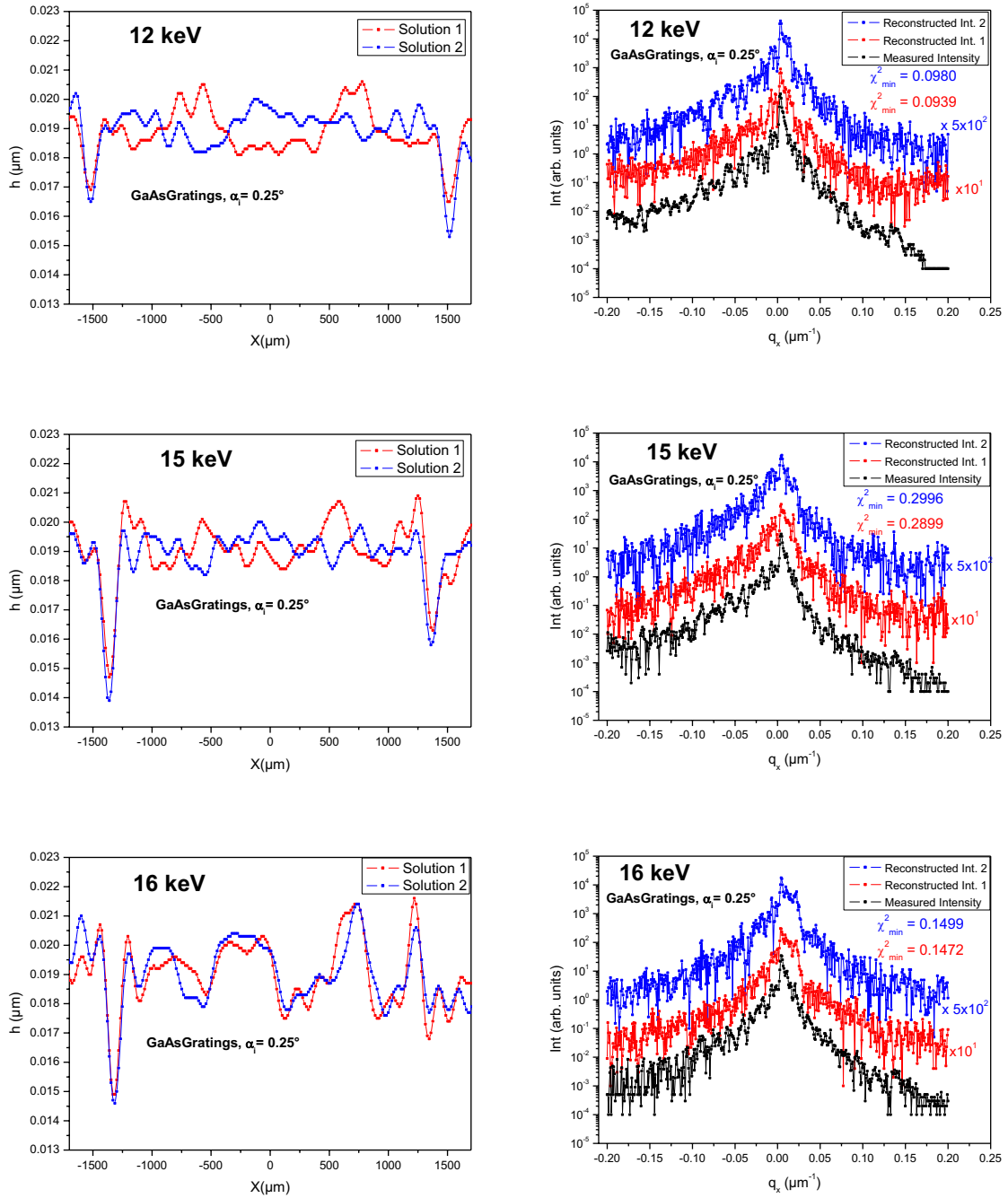


Fig. 6.15 Reconstructed surface height solutions and reconstructed intensity profiles along with measured intensity  $q_x$  scan for the reciprocal space map for GaAs grating at  $E = 12$ , 15 and 16 keV. The reconstructed intensities (red and blue) are plotted with certain vertical offset along intensity axis. The respective value of  $\chi^2_{\min}$  for each fit of the reconstructed intensity to the measured one is mentioned alongside.

The reconstructed surface profiles (Fig. 6.14, Fig. 6.15 left) again does not show any grating like pattern mainly because of the lack of distinct grating peaks. The average surface roughness in the reconstructed surface is larger than that for the reconstructed surface for the

measurement of Si wafer at  $\alpha_i = 0.1^\circ$  (Fig. 6.2, Fig. 6.5), which is  $\sim 1 \text{ nm}$ . The spatial resolution ( $\Delta x$ ) achieved with  $q_x$  – range of  $\pm 0.20 \mu\text{m}^{-1}$  is  $\sim 16 \mu\text{m}$ . Hence it is hard to resolve any grating like pattern which makes about 5 points for the effective grating period ( $88 \mu\text{m}$ ) on the reconstructed surface.

The reconstructed surface profile solutions at different selected energies do not exhibit any similarity (Fig. 6.14, Fig. 6.15 left). The surface height shows large variation from 14 nm to 21 nm.

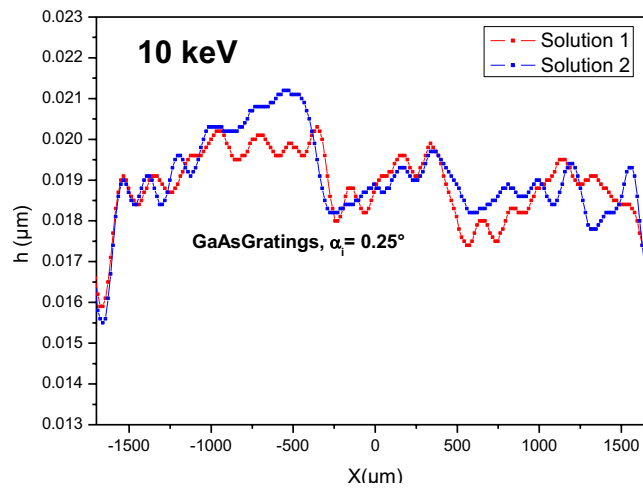


Fig. 6.16 Reconstructed surface height for GaAs grating at  $\alpha_i = 0.25^\circ$  for  $E = 10 \text{ keV}$

The set of solutions for  $E = 10 \text{ keV}$  is discussed in detail (Fig. 6.16). The solution 1 (red curve) shows a minimum in height at  $x = -1660 \mu\text{m}$  with local height of  $\sim 16 \text{ nm}$ . The surface height gradually increases thereafter with smaller local minima and maxima till a drop of 2 nm in local height from  $\sim 20 \text{ nm}$  at  $x = -350 \mu\text{m}$  to  $\sim 18 \text{ nm}$  at  $x = -240 \mu\text{m}$ . One more large step is observed from  $\sim 20 \text{ nm}$  at  $x = +340 \mu\text{m}$  to  $\sim 17.4 \text{ nm}$  at  $x = +560 \mu\text{m}$ . The solution 2 (blue curve) also shows a minimum in height at  $x = -1660 \mu\text{m}$  with local height of  $\sim 16 \text{ nm}$ . The surface height gradually increases thereafter with some local minima and maxima. A drop of 2 nm in local height is observed at several positions. The larger is from  $\sim 21 \text{ nm}$  at  $x = -460 \mu\text{m}$  to  $\sim 18 \text{ nm}$  at  $x = -260 \mu\text{m}$ . Others can be observed from  $\sim 20 \text{ nm}$  at  $x = +350 \mu\text{m}$  to  $\sim 18 \text{ nm}$  at  $x = +605 \mu\text{m}$  and from  $\sim 19 \text{ nm}$  at  $x = +1550 \mu\text{m}$  to  $\sim 16 \text{ nm}$  at  $x = +1675 \mu\text{m}$ . Thus the surface can be said to be composed of large steps of lateral width  $\sim 1 \text{ mm}$  with height variation of  $\sim 2 \text{ nm}$ .

The surface height solutions for higher energies ( $E = 15 \text{ keV}, 16 \text{ keV}$ ) look completely different (Fig. 6.13 left) from those for  $E = 10 \text{ keV}$ . A big step of lateral width 2.8 mm can be seen on the solution for the surface at  $E = 15 \text{ keV}$  with average variation in surface height  $\sim 2 \text{ nm}$ . Whereas, the solution for the surface at  $E = 16 \text{ keV}$  shows many steps of widths ranging from  $\sim 100 \mu\text{m}$  to  $\sim 400 \mu\text{m}$  with almost constant surface height, for example, the step between the lateral positions  $x = -430 \mu\text{m}$  and  $x = -10 \mu\text{m}$ .

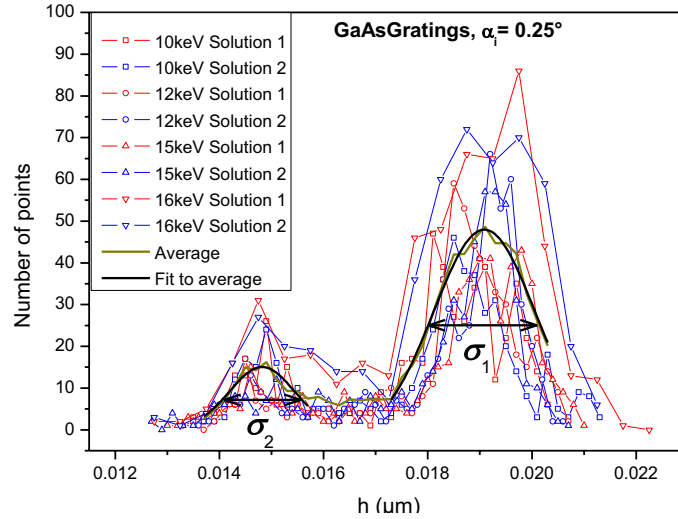


Fig. 6.17 Distribution of surface height for two different reconstructed solutions at  $E = 10, 12, 15$  and  $16 \text{ keV}$ . The thick dark yellow line is the average of the distributions for all the solutions. The thick black line is the Gaussian fit to the average with half width  $\sigma$ .

The distributions of local height (Fig. 6.17) for the reconstructed surface height solutions at different selected energies show relatively broad distribution. The average of all the distributions (thick dark yellow line) for all the solutions for the selected energies is calculated and fitted with Gaussian (thick black line). The Gaussian fit has two maxima, a smaller at 14.8 nm with half width of 1.2 nm and the larger at 19 nm with half width of 1.9 nm. Thus it can be said that the surface possesses two different mean surface heights of  $\sim 19 \text{ nm}$  and  $\sim 15 \text{ nm}$ , which is evident from the reconstructed surface height solutions in Fig. 6.14. The weak maximum in the distribution at  $\sim 15 \text{ nm}$  corresponds to the local minimum observed for many surface height solutions (Fig. 6.14, Fig. 6.15 left). The broad maximum at  $\sim 19 \text{ nm}$  corresponds to the mean local height of many steps observed for all the solutions at different selected energies.

As seen in reciprocal space map in Fig. 6.13 and also in the  $q_x$  -scans at different energies in Fig. 6.14 and Fig. 6.15 (right) (black curves), the complete  $q_x$  range of  $-0.2$  to  $+0.2 \mu\text{m}^{-1}$

cannot be accessed at  $E = 10 \text{ keV}, 12 \text{ keV}$ . This poses problems in getting converging solution as already observed in case of GaAs grating at  $\alpha_i = 0.1^\circ$ . Thus the distributions of surface height (Fig. 6.17) at different energies show different nature with maximum at different local height. For higher energies  $E = 15 \text{ keV}, 16 \text{ keV}$  the scattering measured (Fig. 6.13) only for the range  $q_x = \pm 0.1 \mu\text{m}^{-1}$  is useful. Outside this range the scattering is weak and featureless. This lack of useful data also affects the convergence of the algorithm.

#### 6.1.4 Triangular shaped Si wafer with sample width 0.8 mm

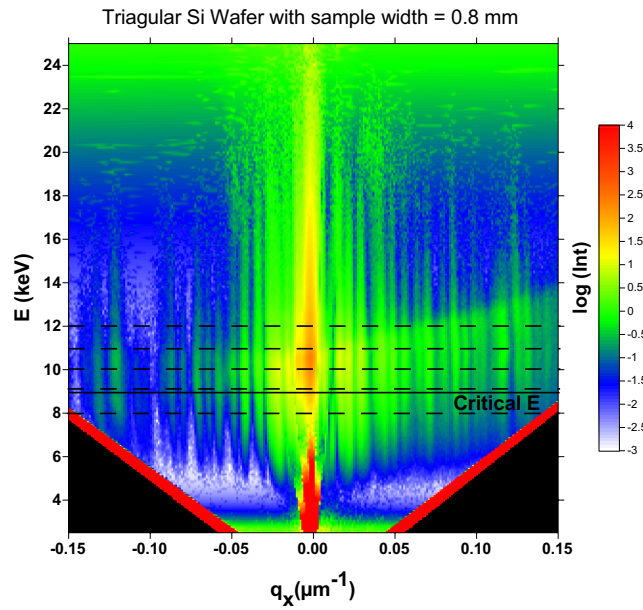


Fig. 6.18 Measured reciprocal space map in  $(q_x, E)$  space for triangular shaped Si wafer with sample width 0.8 mm at  $\alpha_i = 0.2^\circ$ . The black horizontal line indicates the critical energy ( $E_c = 8.95 \text{ keV}$ ) for Si at  $\alpha_i = 0.2^\circ$ . The dashed black lines mark the selected energies ( $E = 8, 9, 10, 11$  and  $12 \text{ keV}$ ).

Fig. 6.18 shows the reciprocal space map measurement plotted in  $(q_x, E)$  space for triangular shaped Si wafer with sample width of 0.8 mm at angle of incidence of  $\alpha_i = 0.2^\circ$  (Fig. 4.12). The  $q_x$  – scans over  $q_x$  range of  $q_x = \pm 0.15 \mu\text{m}^{-1}$  are extracted at  $E = 8 \text{ keV}, 9 \text{ keV}, 10 \text{ keV},$

$11 \text{ keV}$  and  $12 \text{ keV}$  which lie in the energy range of the maximum in the scattered intensity. With the critical energy of  $E_c = 8.95 \text{ keV}$  for Si at  $\alpha_i = 0.2^\circ$ , the only scan which for which x-rays experience total external reflection is the scan at  $E = 8 \text{ keV}$ . The complete range of  $q_x = -0.15$  to  $+0.15 \mu\text{m}^{-1}$  is accessible for all the selected energies except at  $E = 8 \text{ keV}$ .

The accessible range at  $E = 8 \text{ keV}$  is  $q_x = -0.144 \text{ to } +0.14 \mu\text{m}^{-1}$ . The scattering features are almost similar different selected energies.

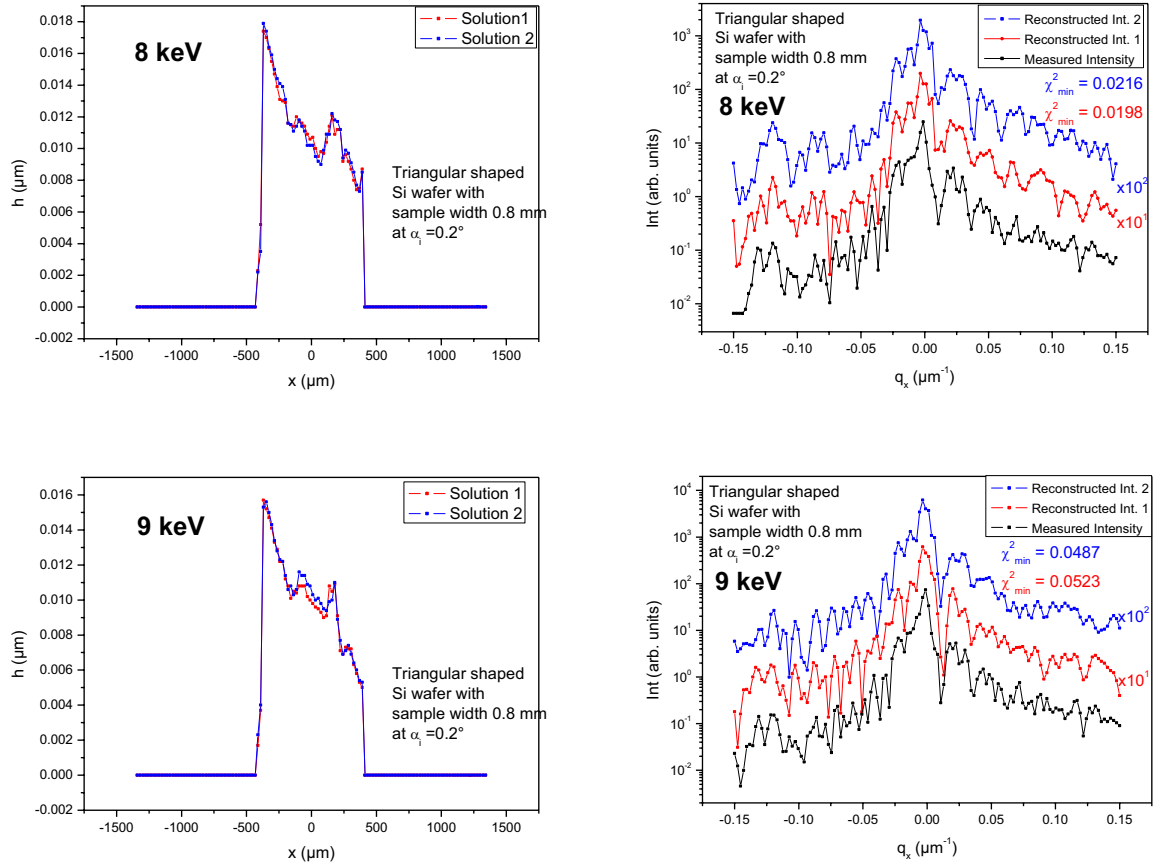


Fig. 6.19 Reconstructed surface height solutions and reconstructed intensity profiles along with measured intensity  $q_x$  scan for the reciprocal space map for triangular shaped Si wafer with sample width  $0.8 \text{ mm}$  at  $E = 8$  and  $9 \text{ keV}$ . The surface height and scattered intensity are reconstructed using the modified GS algorithm with support constraint. The reconstructed intensities (red and blue) are plotted with certain vertical offset along intensity axis. The respective value of  $\chi^2_{\min}$  for each fit of the reconstructed intensity to the measured one is mentioned alongside.

The fact that the sample is laterally confined with width of  $0.8 \text{ mm}$  makes it possible to apply a support constraint in the real space. The object density is considered zero outside the sample width of  $0.8 \text{ mm}$ . The surface profile is reconstructed (Fig. 6.19) using the modified GS algorithm (equations (5.57) to (5.63)) with this additional real space constraint.

The additional support constraint helps the algorithm to reach to almost a converging solution for the reconstructions at all the energies (Fig. 6.19 left). The reconstructed surface profiles look almost similar at different energies.

The height at the edge is  $\sim 18$  nm at lateral position  $x = -370 \mu\text{m}$  for the solution at 8 keV. The surface can be seen to be continuously decreasing till 9 nm at  $x = +73 \mu\text{m}$ . The surface height again increases to  $\sim 12$  nm and at the other edge it is  $\sim 8.5$  nm. Thus the surface can be seen to be made up of two large steps with gradually decreasing local heights of widths  $443 \mu\text{m}$  and  $240 \mu\text{m}$ .

The surface height reconstructed at 9 keV shows similar profile. It possesses two large steps from  $x = -350 \mu\text{m}$  to  $+116 \mu\text{m}$  with surface height varying from 15.5 nm to 9.5 nm and from  $x = +180 \mu\text{m}$  to  $+390 \mu\text{m}$  with surface height varying from 11 nm to 5.3 nm. The first step has additional local maxima with surface height  $\sim 11$  nm at  $x = -73 \mu\text{m}$ .

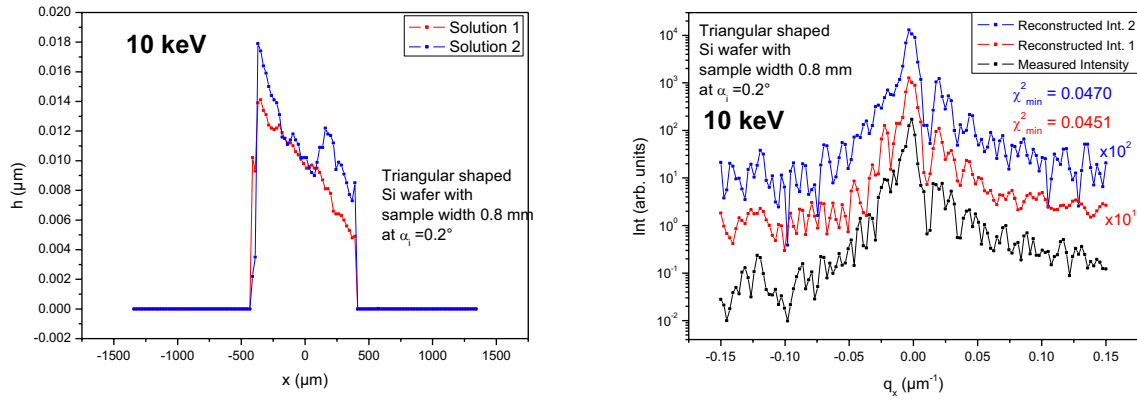


Fig. 6.20 Reconstructed surface height solutions and reconstructed intensity profiles along with measured intensity  $q_x$  scan for the reciprocal space map for triangular shaped Si wafer with sample width 0.8mm at  $E = 10\text{keV}$ . The surface height and scattered intensity are reconstructed using the modified GS algorithm with support constraint. The reconstructed intensities (red and blue) are plotted with certain vertical offset along intensity axis. The respective value of  $\chi^2_{\text{min}}$  for each fit of the reconstructed intensity to the measured one is mentioned alongside.

The two solutions for reconstructed surface height (Fig. 6.20 left) at 10 keV look different. The reconstructed intensity fits well for solution 1 (red), as seen in Fig. 6.20 right. The solution 1 (red) can be considered to describe the surface height of the sample. The surface height at the edge is 14 nm at  $x = -350 \mu\text{m}$  and gradually reduces till the other edge to 5 nm at  $x = +390 \mu\text{m}$ . It also shows some local maxima in height.



## Surface height profile reconstruction from the measured surface speckle data

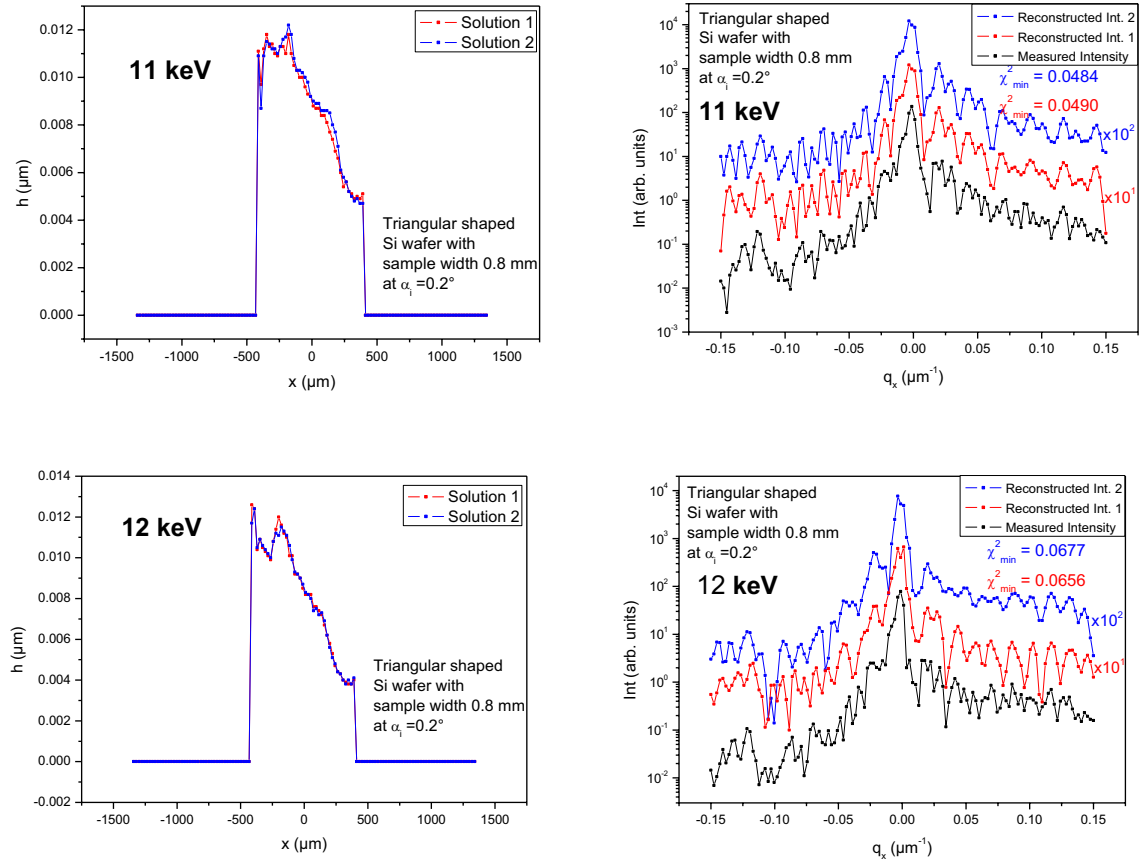


Fig. 6.21 Reconstructed surface height solutions and reconstructed intensity profiles along with measured intensity  $q_x$  scan for the reciprocal space map for triangular shaped Si wafer with sample width 0.8 mm at  $E = 11$  and  $12$  keV. The surface height and scattered intensity are reconstructed using the modified GS algorithm with support constraint. The reconstructed intensities (red and blue) are plotted with certain vertical offset along intensity axis. The respective value of  $\chi_{min}^2$  for each fit of the reconstructed intensity to the measured one is mentioned alongside.

From the solutions at 11 keV and 12 keV (Fig. 6.21 left) the surface can be seen to be made of two steps  $x = -390 \mu\text{m}$  to  $-260 \mu\text{m}$  with surface height varying from 12.5 nm to 10 nm and from  $x = -200 \mu\text{m}$  to  $+390 \mu\text{m}$  with surface height varying from 12 nm to 4 nm. The local height at the edge for the first step for the solution 1 at 11keV is slightly different from that at 12 keV. It is  $\sim 12$  nm at  $x = -350 \mu\text{m}$ .

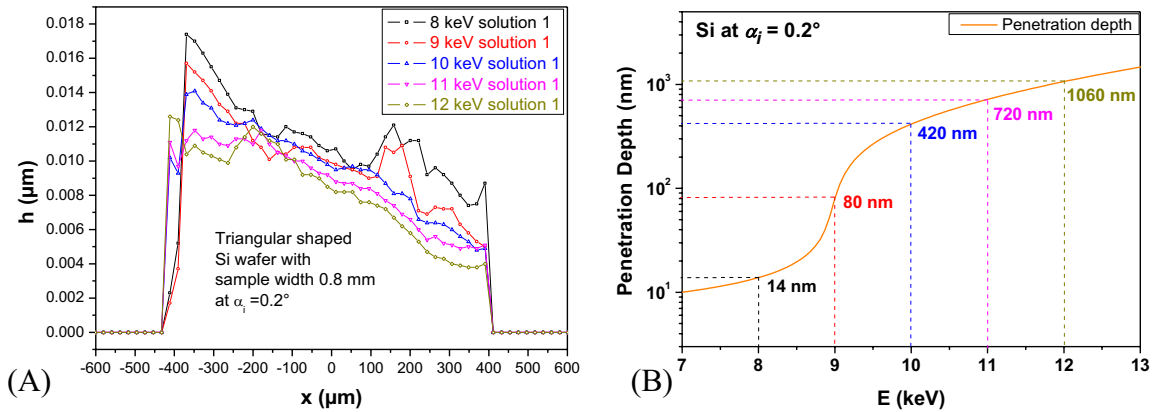


Fig. 6.22 (A) Reconstructed surface profile at all the selected energies  $E = 8, 9, 10, 11$  and  $12 \text{ keV}$ . (B) Calculated penetration depth at  $\alpha_i = 0.2^\circ$  for Si for different energies of x-rays calculated using equation (2.18).

Except 8 keV the condition for total external reflection is not fulfilled. Hence the reconstructed surface heights at different selected energies  $E = 9, 10, 11$  and  $12 \text{ keV}$  give the sub-surface profile information of the sample due to different penetration depths at different selected energies. Fig. 6.22(A) gives a two dimensional picture of the sample, spatially resolved and depth resolved. The local surface height gradually decreases as x-rays with higher energies as x-rays penetrate deeper inside the sample from  $\sim 14 \text{ nm}$  at  $8 \text{ keV}$  to  $\sim 1 \mu\text{m}$  at  $12 \text{ keV}$  of x-ray energy (Fig. 6.22(B)). The reconstructed surface profile at lower energies 8 keV and 9 keV possess more roughness. The roughness of the reconstructed surface profile decreases for the energies from 8 keV to 12 keV, especially for lateral surface positions  $x = -100 \mu\text{m}$  to  $+400 \mu\text{m}$ . At higher energies the reconstructed surface profile tends to become smoother. As one goes deep inside the bulk of the sample, the electron density becomes homogeneous and shows less and less surface roughness features which are at the interface of material of the sample and the air.

Fig. 6.23 shows the distributions of local height for the reconstructed surface height solutions at different selected energies. The first peak near zero corresponds to the zero density region outside finite sample size of 0.8 mm.

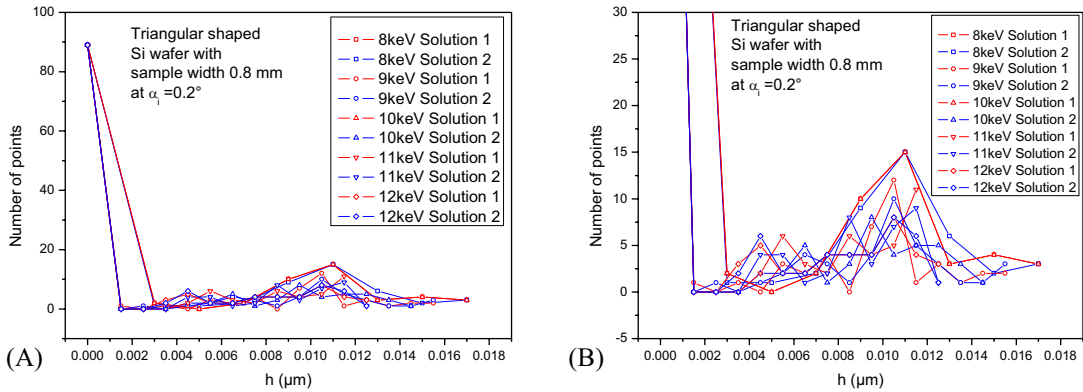


Fig. 6.23 Distribution of surface height for two different reconstructed solutions at  $E = 8, 9, 10, 11$  and  $12$  keV (A) The large vertical scale (B) Selected vertical scale

The distribution in height is relatively broad with mean surface height of  $\sim 11$  nm (Fig. 6.23(B)). It is clear from the reconstructed solutions for the surface height profiles that the surface does not possess any mean height but the surface has gradually decreasing height from  $\sim 17$  to  $\sim 11$  nm at one edge and from  $\sim 8$  to  $\sim 4$  nm corresponding to the energies from 8 keV to 12 keV (Fig. 6.22).

### 6.1.5 Triangular shaped Si wafer with sample width 2.3 mm

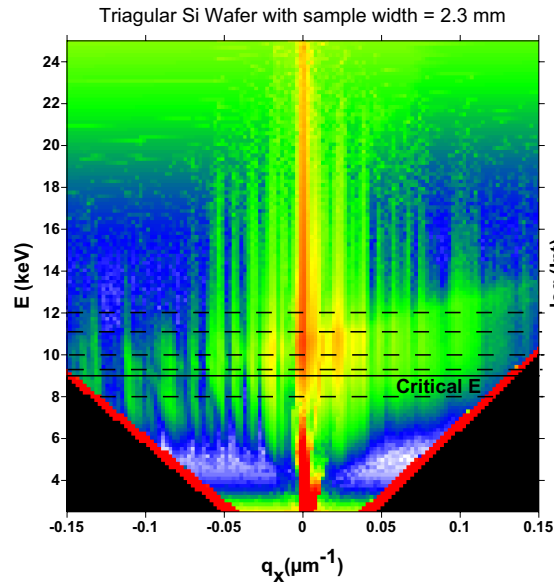


Fig. 6.24 Measured reciprocal space map in  $(q_x, E)$  space for triangular shaped Si wafer with sample width 2.3 mm at  $\alpha_i = 0.2^\circ$ . The black horizontal line indicates the critical energy ( $E_c = 8.95$  keV) for Si at  $\alpha_i = 0.2^\circ$ . The dashed black lines mark the selected energies ( $E = 8, 9, 10, 11$  and  $12$  keV).

Fig. 6.24 shows the reciprocal space map measurement plotted in  $(q_x, E)$  space for triangular shaped Si wafer with sample width of 2.3 mm at angle of incidence of  $\alpha_i = 0.2^\circ$  (Fig. 4.12). The  $q_x$  – scans over  $q_x$  range of  $q_x = \pm 0.15 \mu\text{m}^{-1}$  are extracted at  $E = 8 \text{ keV}, 9 \text{ keV}, 10 \text{ keV}, 11 \text{ keV}$  and  $12 \text{ keV}$  which lie in the energy range of the maximum in the scattered intensity. With the critical energy of  $E_c = 8.95 \text{ keV}$  for Si at  $\alpha_i = 0.2^\circ$ , the only scan for which x-rays experience total external reflection is the scan at  $E = 8 \text{ keV}$ . The complete range of  $q_x = -0.15$  to  $+0.15 \mu\text{m}^{-1}$  is accessible for all the selected energies except at  $E = 8 \text{ keV}$ . The accessible range at  $E = 8 \text{ keV}$  is  $q_x = -0.144$  to  $+0.14 \mu\text{m}^{-1}$ . The scattering features are almost similar different selected energies.

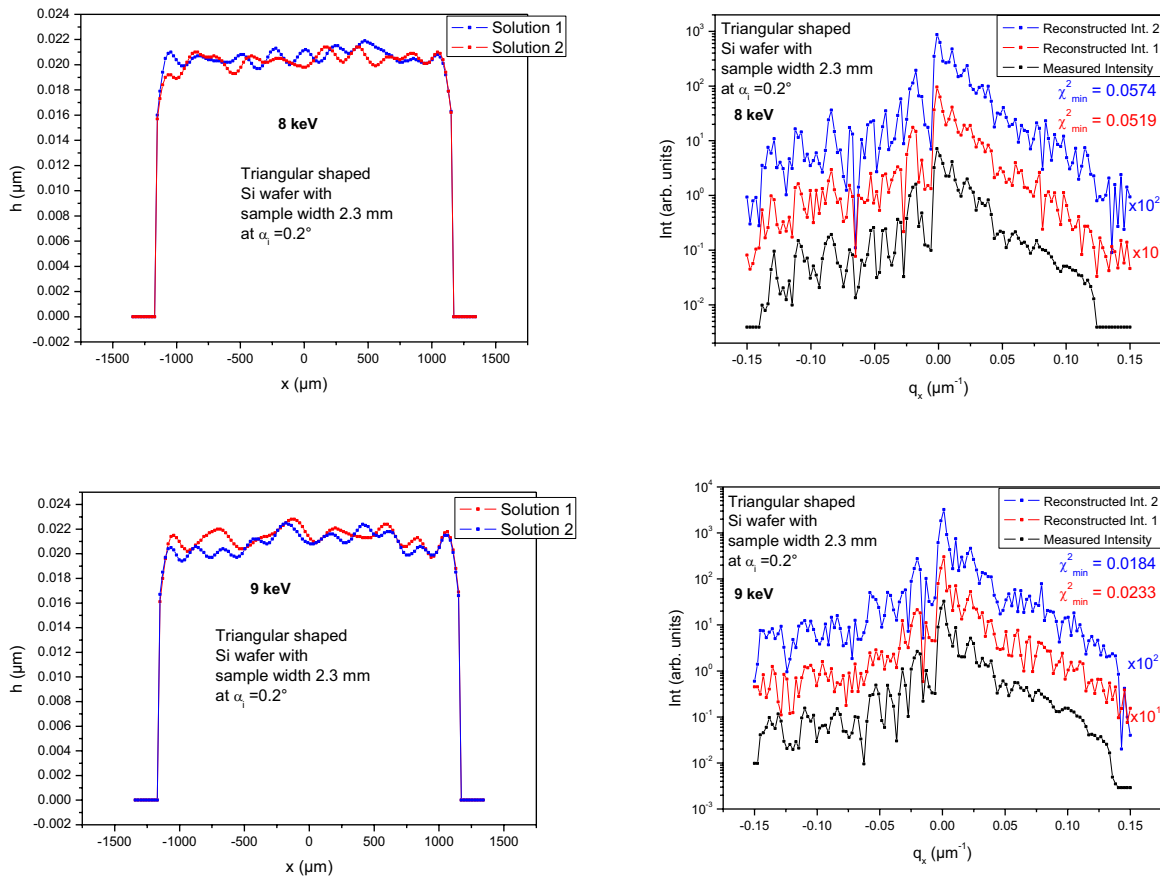


Fig. 6.25 Reconstructed surface height solutions and reconstructed intensity profiles along with measured intensity  $q_x$  scan for the reciprocal space map for triangular shaped Si wafer with sample width 2.3mm at  $E = 8$  and  $9 \text{ keV}$ . The surface height and scattered intensity are reconstructed using the modified GS algorithm with support constraint. The reconstructed intensities (red and blue) are plotted with certain vertical offset along intensity axis. The respective value of  $\chi_{min}^2$  for each fit of the reconstructed intensity to the measured one is mentioned alongside.

As in the previous reconstruction the support constraint is included in the modified GS algorithm. The size of the support or the lateral sample width (2.3mm) is much larger than

half of the illuminated area or the footprint at the sample position. Although, the simulations for the scattered intensities exhibit reasonable fit with the measured intensity pattern.

The reconstructed surface profiles at 8 keV and 9 keV (Fig. 6.25) exhibit step like features with different widths of the steps having different average height. The widths over which the height is almost constant are smaller as compared to those observed in case of GaAs plain wafer (Fig. 6.2). The average width of the steps can be observed to be  $\sim 100 \mu\text{m}$ . The average surface height varies from 19 nm to 22 nm.

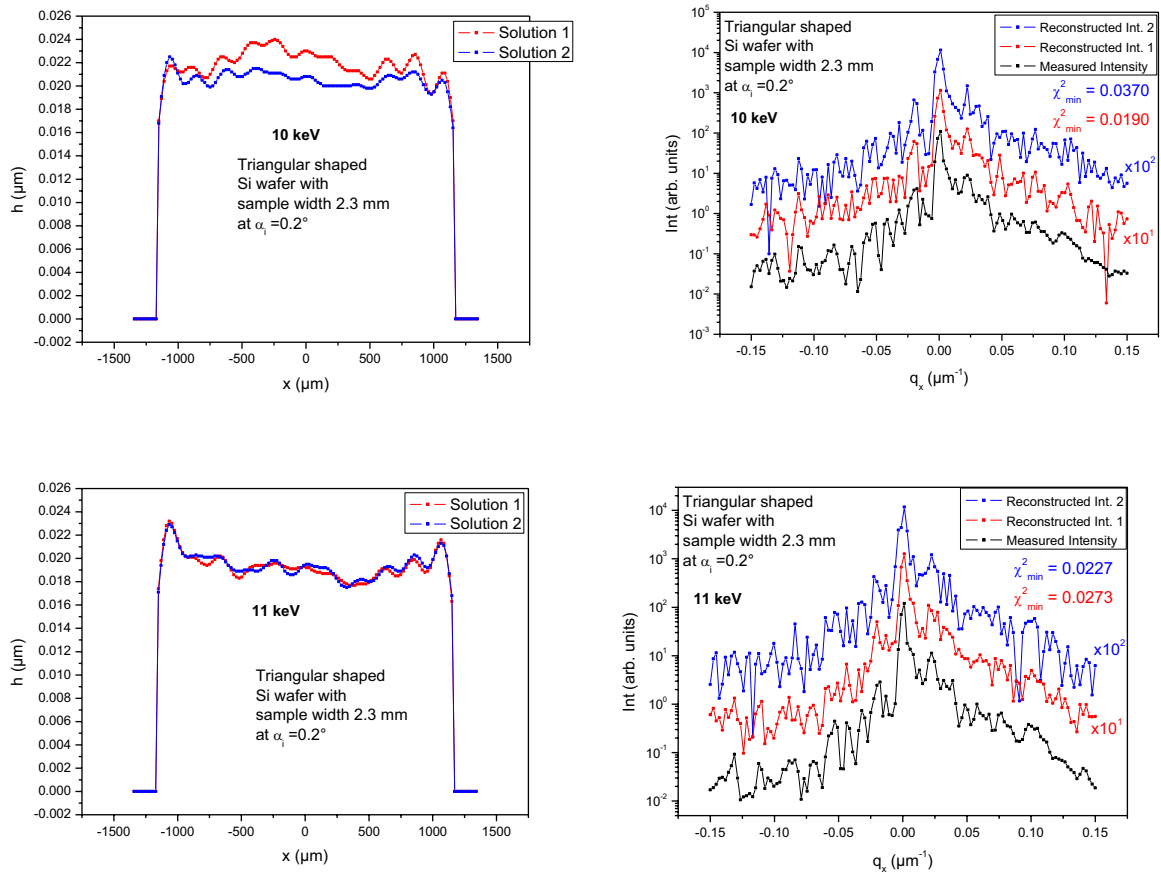


Fig. 6.26 Reconstructed surface height solutions and reconstructed intensity profiles along with measured intensity  $q_x$  scan for the reciprocal space map for triangular shaped Si wafer with sample width 2.3mm at  $E = 10$  and  $11 \text{ keV}$ . The surface height and scattered intensity are reconstructed using the modified GS algorithm with support constraint.

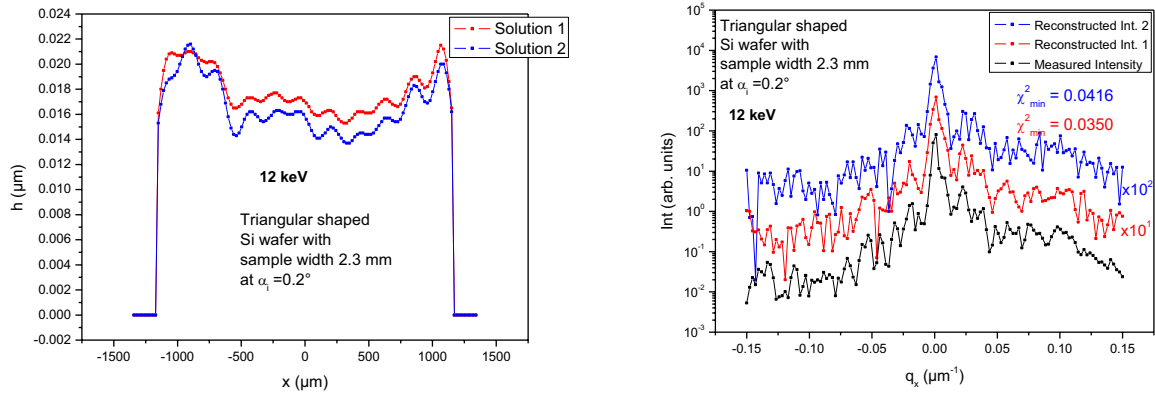


Fig. 6.27 Reconstructed surface height solutions and reconstructed intensity profiles along with measured intensity  $q_x$  scan for the reciprocal space map for triangular shaped Si wafer with sample width 2.3mm at  $E = 12 \text{ keV}$ . The surface height and scattered intensity are reconstructed using the modified GS algorithm with support constraint.

The reconstructed surface height profiles at 10 keV, 11 keV and 12 keV (Fig. 6.26, Fig. 6.27 left) exhibit large variation of surface height. The reconstructed intensity at 10 keV for solution (blue) 2 fits well with the measured intensity pattern (black). Hence solution 1 for the surface height at 10 keV can be regarded to be more correct. The average surface height shows variation of  $\sim 5 \text{ nm}$  from 19 nm to 24 nm. Number of smaller steps of width  $\sim 100 \mu\text{m}$  can be seen but between the lateral position  $x = -95 \mu\text{m}$  to  $+500 \mu\text{m}$  the surface height decreases almost gradually from 22.5 nm to 20 nm.

Considering the better fit for solution 1 for the reconstructed intensity (red) with the measured intensity profile (black) at 11keV the corresponding solution for reconstructed surface height is regarded to be more correct. The average surface height again shows the variation of  $\sim 5 \text{ nm}$  from 18 nm to 23 nm in this case also. The surface height is almost constant ( $\sim 19 \text{ nm}$ ) between  $x = -390 \mu\text{m}$  and  $x = +200 \mu\text{m}$ .

Again solution 1 can be regarded as more correct due to the better fit of reconstructed intensity (red) with the measured intensity profile (black). The surface has a plateau with average surface height  $\sim 21 \text{ nm}$  near the edge between  $x = -1065 \mu\text{m}$  and  $x = -700 \mu\text{m}$ . Then the surface height drops to 16.5 nm at  $x = -560 \mu\text{m}$  thereafter. Till the other edge the surface consists of almost 8 smaller steps of widths  $\sim 150 \mu\text{m}$  with different surface height from 16 nm to 21 nm.

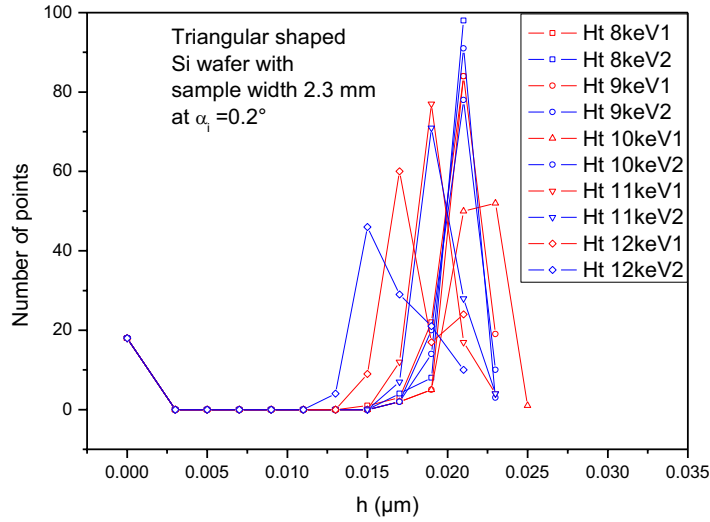


Fig. 6.28 Distribution of surface height for two different reconstructed solutions at  $E = 8, 9, 10, 11$  and  $12$  keV

The distributions of local height (Fig. 6.28) for the reconstructed surface height solutions at different selected energies show maxima at different local heights. The average surface height for solutions at different energies is not the same. There is almost a systematic shift of average surface height from higher value 21 nm to 15 nm. This is evident due to the fact that x-rays at different energies have different penetration depth. The surface profile information is reconstructed as a function of depth inside the sample (Fig. 6.25, Fig. 6.26 and Fig. 6.27).

### 6.1.6 Triangular shaped Si wafer with sample width > footprint

Fig. 6.29 shows the reciprocal space map measurement plotted in  $(q_x, E)$  space for triangular shaped Si wafer with sample width larger than the footprint at angle of incidence of  $\alpha_i = 0.2^\circ$  (Fig. 4.12). The  $q_x$  – scans over  $q_x$  range of  $q_x = \pm 0.15 \mu\text{m}^{-1}$  are extracted at  $E = 8$  keV, 9 keV, 10 keV, 11 keV and 12 keV which lie in the energy range of the maximum in the scattered intensity. With the critical energy of  $E_c = 8.95$  keV for Si at  $\alpha_i = 0.2^\circ$ , the only scan which for which x-rays experience total external reflection is the scan at  $E = 8$  keV. The complete range of  $q_x = -0.15$  to  $+0.15 \mu\text{m}^{-1}$  is accessible for all the selected energies except at  $E = 8$  keV.

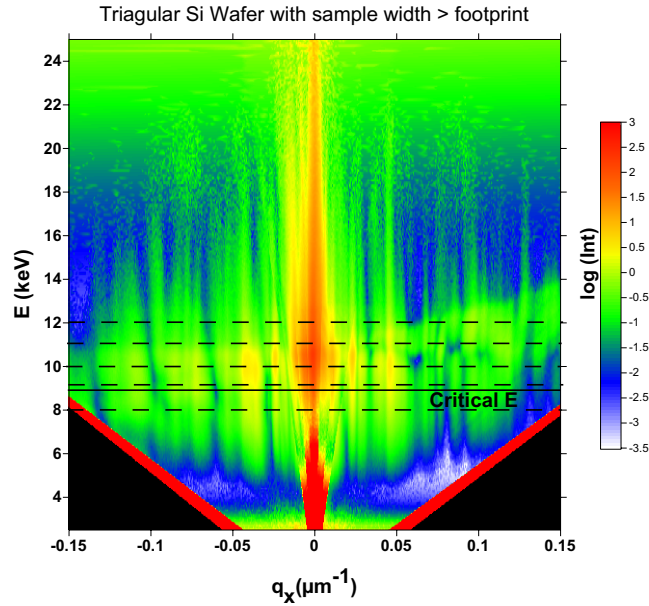


Fig. 6.29 Measured reciprocal space map in  $(q_x, E)$  space for triangular shaped Si wafer with sample width  $>$  footprint at  $\alpha_i = 0.2^\circ$ . The black horizontal line indicates the critical energy ( $E_c = 8.95 \text{ keV}$ ) for Si at  $\alpha_i = 0.2^\circ$ . The dashed black lines mark the selected energies ( $E = 8, 9, 10, 11$  and  $12 \text{ keV}$ ).

The accessible range at  $E = 8 \text{ keV}$  is  $q_x = -0.144$  to  $+0.14 \mu\text{m}^{-1}$ . The scattering features are not as distinct as in earlier two cases (Fig. 6.18 and Fig. 6.24). Also the features are not the same at different energies. It can be easily seen that the positions of various minima shifts at different energies. For example, at  $q_x = +0.06 \mu\text{m}^{-1}$  a minimum is observed for  $10 \text{ keV}$ . For  $11 \text{ keV}$  there is a weak scattering observed at this position whereas it again shows a broad minimum at  $12 \text{ keV}$ .

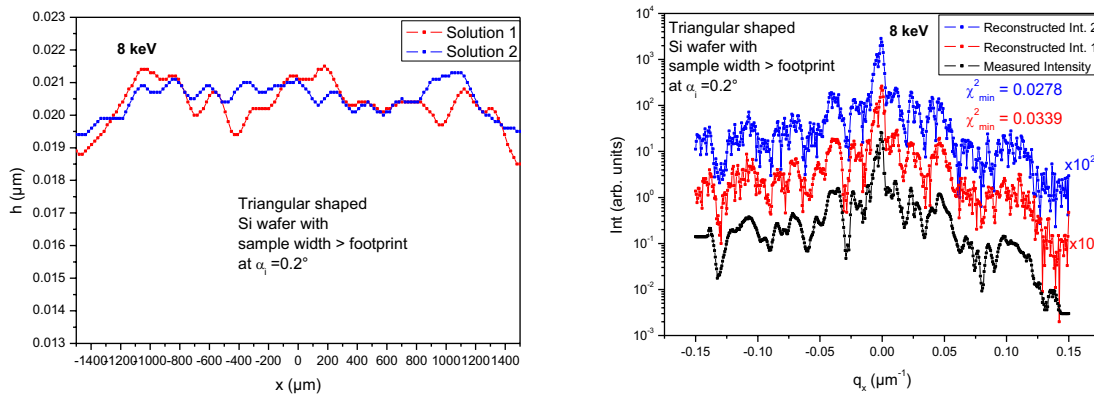


Fig. 6.30 Reconstructed surface height solutions and reconstructed intensity profiles along with measured intensity  $q_x$  scan for the reciprocal space map for triangular shaped Si wafer with sample width  $>$  footprint at  $E = 8 \text{ keV}$ . The surface height and scattered intensity are reconstructed using the modified GS algorithm. The reconstructed intensities (red and blue) are plotted with certain vertical offset along intensity axis. The respective value of  $\chi_{min}^2$  for each fit of the reconstructed intensity to the measured one is mentioned alongside.



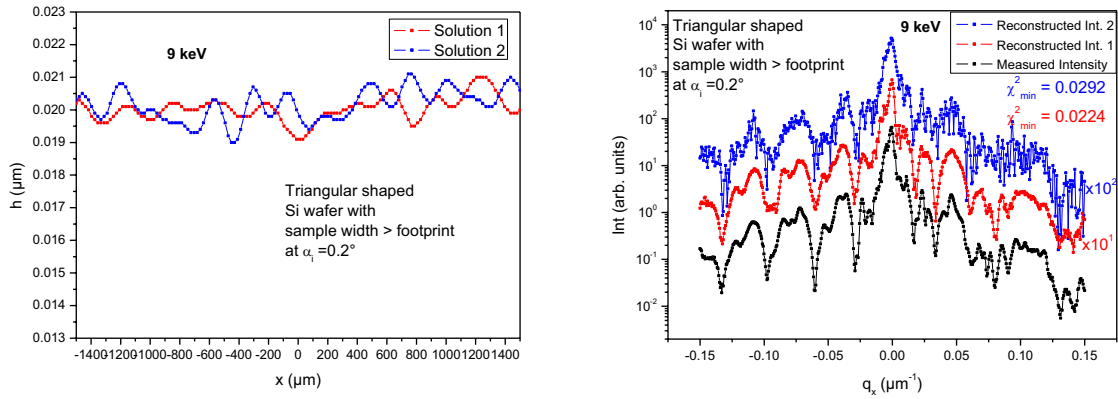


Fig. 6.31 Reconstructed surface height solutions and reconstructed intensity profiles along with measured intensity  $q_x$  scan for the reciprocal space map for triangular profiles for triangular shaped Si wafer with sample width  $>$  footprint at  $E = 9 \text{ keV}$ . The surface height and scattered intensity are reconstructed using the modified GS algorithm. The reconstructed intensities (red and blue) are plotted with certain vertical offset along intensity axis. The respective value of  $\chi_{min}^2$  for each fit of the reconstructed intensity to the measured one is mentioned alongside.

This case is similar to some previous cases for GaAs plain wafer (section 6.1.1) and GaAs surface grating (section 6.1.2 and section 6.1.3) as the surface is not laterally confined. The surface profile is reconstructed using modified GS algorithm. The reconstructed surface profiles (Fig. 6.30, Fig. 6.31 and Fig. 6.32 left) again exhibit only the long range surface roughness features.

Both the reconstructed intensity profiles for solution 1 (red) and solution 2 (blue) show reasonable fit with the measured intensity pattern (black) for 8 keV and 9 keV. The variation in surface height is  $\sim 2.5 \text{ nm}$  from  $\sim 19 \text{ nm}$  to  $\sim 21.5 \text{ nm}$ . The surface for solution 1 (red) for 8 keV shows gradual increase in local height from  $\sim 19 \text{ nm}$  to  $\sim 21.5 \text{ nm}$  for lateral positions  $x = -1500 \mu\text{m}$  to  $x = -1060 \mu\text{m}$ . Thereafter it has steps of average widths between  $100 \mu\text{m}$  and  $15 \mu\text{m}$  with varying heights  $19.5 \text{ nm}$  to  $21.5 \text{ nm}$ . The solution 2 (blue) for 8 keV also contains steps of average widths  $100 \mu\text{m}$  with varying heights  $19.5 \text{ nm}$  to  $21 \text{ nm}$  except a wide hump with maximum of  $21.5 \text{ nm}$  at  $x = +1100 \mu\text{m}$ .

The solution 1 (red) for 9 keV has steps of widths around  $100 \mu\text{m}$  with variation of local height of only  $1 \text{ nm}$  between  $19.5 \text{ nm}$  and  $20.5 \text{ nm}$  till the lateral position of  $x = -200 \mu\text{m}$ . Beyond this till the other edge the steps with widths  $100 \mu\text{m}$  to  $200 \mu\text{m}$  can be observed with height ranging from  $19 \text{ nm}$  to  $21 \text{ nm}$ . The solution 2 (blue) is relatively rough with almost 18 smaller steps of widths  $100 \mu\text{m}$  to  $150 \mu\text{m}$  with local height from  $19 \text{ nm}$  to  $21 \text{ nm}$ .

## Surface height profile reconstruction from the measured surface speckle data

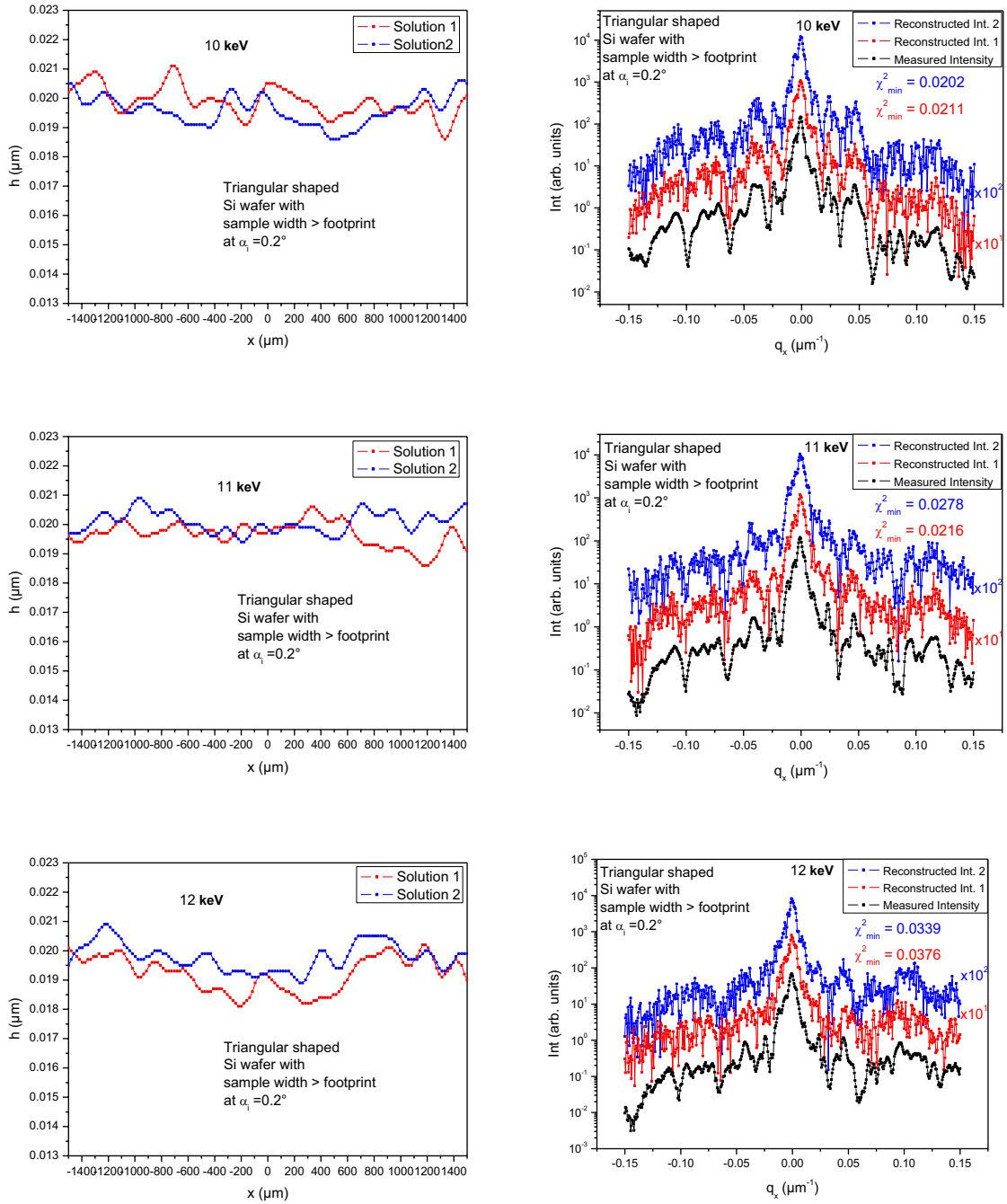


Fig. 6.32 Reconstructed surface height solutions and reconstructed intensity profiles along with measured intensity  $q_x$  scan for the reciprocal space map for triangular shaped Si wafer with sample width > footprint at  $E = 10, 11$  and  $12$  keV. The surface height and scattered intensity are reconstructed using the modified GS algorithm. The reconstructed intensities (red and blue) are plotted with certain vertical offset along intensity axis. The respective value of  $\chi^2_{min}$  for each fit of the reconstructed intensity to the measured one is mentioned alongside.

The solutions (red and blue) for surface height for 10 keV show less number of steps with relatively larger widths of almost  $200\ \mu\text{m}$ . There are few steps with even larger widths with average height around  $19.5\ \text{nm}$  or  $20\ \text{nm}$ .

The variation of local height for solution 1 (red) is more than for solution 2 (blue) for  $11\ \text{keV}$ . The local height varies more for lateral positions  $x > +600\ \mu\text{m}$  for both the solutions. The average local height for solution 1 increases whereas it decreases for solution 2 for  $x > +600\ \mu\text{m}$ .

The widths of steps for solution 1 (red) and solution 2 (blue) for  $12\ \text{keV}$  are around  $200\ \mu\text{m}$ . They also show some large plateaus of larger widths. For example, a plateau between  $x = -300\ \mu\text{m}$  and  $x = +150\ \mu\text{m}$  with average height of  $19.3\ \text{nm}$  and between  $x = +600\ \mu\text{m}$  and  $x = +900\ \mu\text{m}$  with average height  $20.5\ \text{nm}$  for solution 2 (blue).

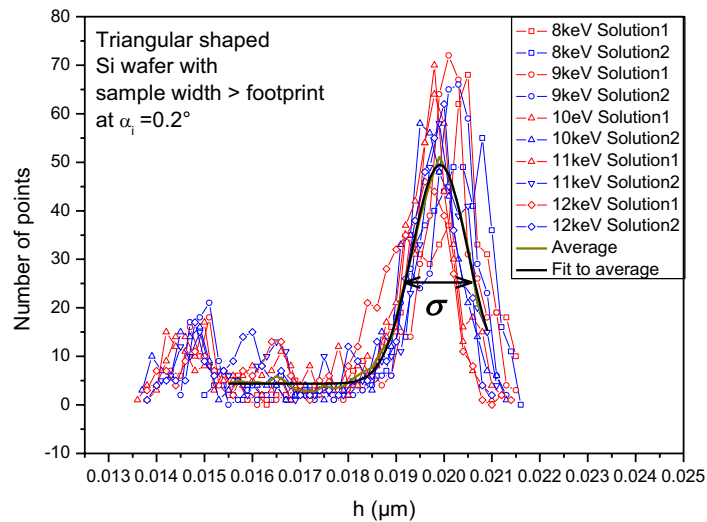


Fig. 6.33 Distribution of surface height for two different reconstructed solutions at  $E = 8, 9, 10, 11$  and  $12\ \text{keV}$ . The thick dark yellow line is the average of the distributions for all the solutions. The thick black line is the Gaussian fit to the average with half width  $\sigma$ .

The average of all the distributions (thick dark yellow line in Fig. 6.33) for all the solutions for the selected energies is calculated and fitted with Gaussian (thick black line). The Gaussian fit has the maximum at  $19.9\ \text{nm}$  with half width of  $1.1\ \text{nm}$ . Thus the mean local height of the reconstructed surface comes out to be  $\sim 20\ \text{nm}$  with roughness  $\sigma \sim 1\ \text{nm}$ , which is in agreement with the roughness found in Ref. [6.1]. But the reconstructed surfaces also show

some features with local height  $\sim 14.5$  nm and  $\sim 16.5$  nm. The distribution of the local height on the sample surface changes from solution to solution (Fig. 6.33). As compared to previous two cases in section 6.1.4 (Triangular shaped Si wafer with sample width 0.8 mm) and section 6.1.5 (Triangular shaped Si wafer with sample width 2.3 mm) the solutions at different energies do not have gradual decrease in the local height. This means the reconstructed surface height profile is not depth dependent although the scattering is measured at different x-ray energies (9, 10, 11 and 12 keV) greater than the critical energy of  $E_c = 8.95$  keV for Si at  $\alpha_i = 0.2^\circ$ . One of the reasons might be the lack of finite support region in real space. The lateral width of the sample is larger than the footprint in contrast to previous two cases (section 6.1.4 and section 6.1.5). The algorithm is not able to find a converging solution in this case. Hence it cannot find solutions for the surface height profile with correct height for different energies of x-rays.

### 6.1.7 Spatially confined GaAs grating with sample width 1.6 mm

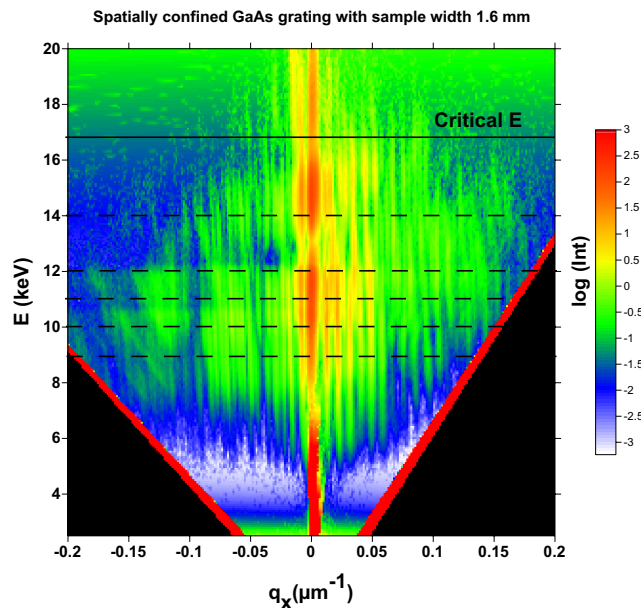


Fig. 6.34 Measured reciprocal space map in  $(q_x, E)$  space for spatially confined GaAs grating with sample width 1.6 mm at  $\alpha_i = 0.16^\circ$ . The black horizontal line indicates the critical energy ( $E_c = 16.6$  keV) for Si at  $\alpha_i = 0.16^\circ$ . The dashed black lines mark the selected energies ( $E = 9, 10, 11, 12$  and  $14$  keV).

Fig. 6.34 shows the reciprocal space map measurement plotted in  $(q_x, E)$  space for spatially confined GaAs grating with sample width of 1.6 mm (Fig. 4.14). The  $q_x$  – scans over  $q_x$

range of  $q_x = \pm 0.2 \mu\text{m}^{-1}$  are extracted at  $E = 9 \text{ keV}, 10 \text{ keV}, 11 \text{ keV}, 12 \text{ keV}$  and  $14 \text{ keV}$  which lie in the energy range of the maximum in the scattered intensity.

With the critical energy of  $E_c = 16.60 \text{ keV}$  for GaAs at  $\alpha_i = 0.16^\circ$ , all the selected energies lie below this critical energy and the total external reflection of the x-ray beam occurs for all these selected energies. The scattered intensity is very weak for the energies above  $E_c = 16.60 \text{ keV}$  to be useful for reconstructing surface profile. The scattering pattern is similar for the energies  $E = 9 \text{ keV}, 10 \text{ keV}, 11 \text{ keV}, 12 \text{ keV}$  only in the  $q_x$  -range of  $q_x = -0.04$  to  $+0.05 \mu\text{m}^{-1}$ . The scattering pattern is relatively featureless for  $q_x = -0.20$  to  $-0.08 \mu\text{m}^{-1}$ . Due to the forbidden region, the scattering is accessible only in the range  $q_x = -0.19$  to  $+0.135 \mu\text{m}^{-1}$  for  $E = 9 \text{ keV}$ . The accessible region further increases with increasing energy. For  $E = 12 \text{ keV}$  it is  $q_x = -0.20$  to  $+0.18 \mu\text{m}^{-1}$ .

Only for  $E = 14 \text{ keV}$  the complete  $q_x$  -range of  $q_x = -0.20$  to  $+0.20 \mu\text{m}^{-1}$  is accessible. But the scattering at  $14 \text{ keV}$  is very weak for  $q_x < -0.09 \mu\text{m}^{-1}$  and  $q_x > +0.13 \mu\text{m}^{-1}$ .

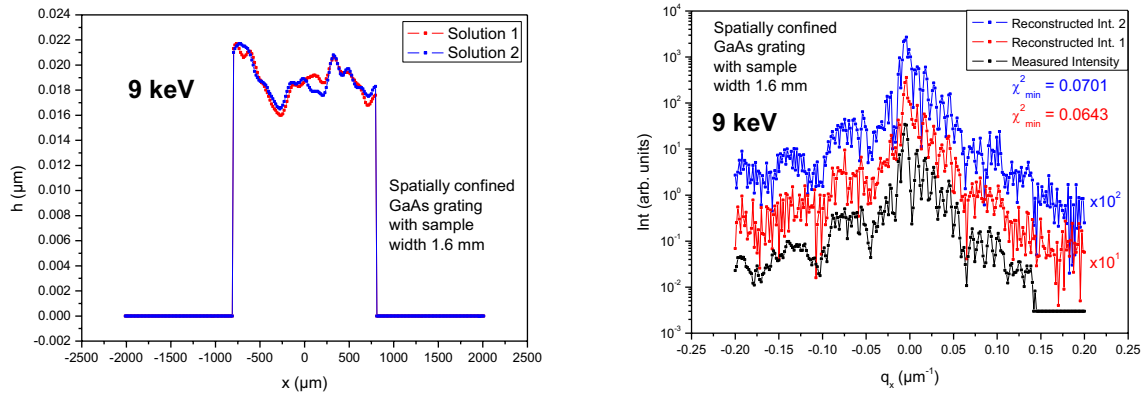


Fig. 6.35 Reconstructed surface height solutions and reconstructed intensity profiles along with measured intensity  $q_x$  scan for the reciprocal space map for spatially confined GaAs grating with sample width 1.6 mm at  $E = 9 \text{ keV}$ . The surface height and scattered intensity are reconstructed using the modified ER algorithm. The reconstructed intensities (red and blue) are plotted with certain vertical offset along intensity axis. The respective value of  $\chi^2_{\min}$  for each fit of the reconstructed intensity to the measured one is mentioned alongside.

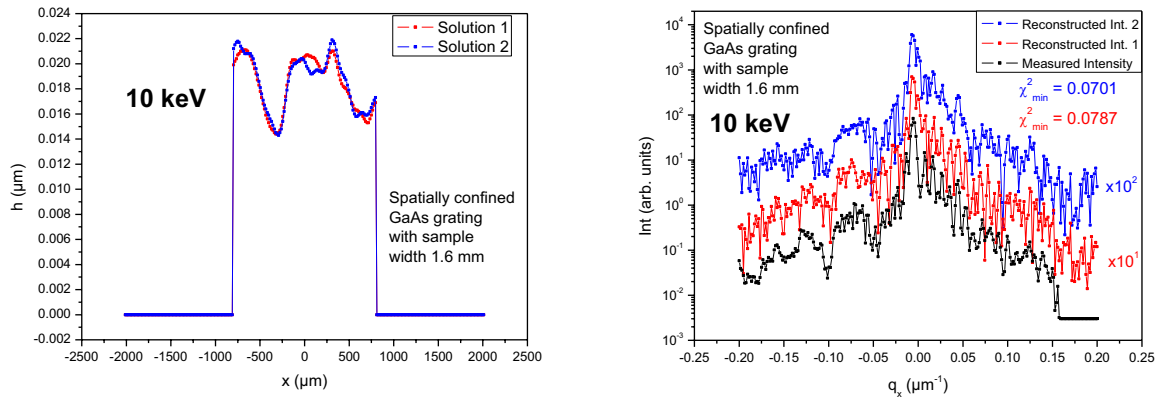


Fig. 6.36 Reconstructed surface height solutions and reconstructed intensity profiles along with measured intensity  $q_x$  scan for the reciprocal space map for spatially confined GaAs grating with sample width 1.6 mm at  $E = 10 \text{ keV}$ . The surface height and scattered intensity are reconstructed using the modified ER algorithm. The reconstructed surface height and scattered intensity (red and blue) are plotted with certain vertical offset along intensity axis. The respective value of  $\chi_{min}^2$  for each fit of the reconstructed intensity to the measured one is mentioned alongside.

The surface profile is reconstructed (Fig. 6.35, Fig. 6.36 left) using the modified GS algorithm (equations (5.57) to (5.63)) with this additional real space constraint of finite support region. The object density is suppressed to zero outside the support region of 1.6 mm, which is the lateral width of the sample.

The lack of sharp grating peaks (Fig. 6.34) prohibits the grating like features to be seen in the reconstructed surface profile (Fig. 6.35, Fig. 6.36 left). With the spatial resolution ( $\Delta x$ ) achieved with  $q_x$  – range of  $\pm 0.20 \mu\text{m}^{-1}$  is  $\sim 16 \mu\text{m}$ , it is hard to resolve any grating like pattern which makes about 6 points for the effective grating period ( $100 \mu\text{m}$ ) on the reconstructed surface. The reconstructed surface profiles (Fig. 6.35, Fig. 6.36 and Fig. 6.37 left) again exhibit only the surface roughness features over larger lateral distances of the whole sample.

The local height for 9 keV reduces from 21.5 nm at lateral position  $x = -780 \mu\text{m}$  at the edge to 16 nm at  $x = -275 \mu\text{m}$ . Till the other edge it shows steps of widths  $\sim 80 \mu\text{m}$  with local height varying from 17.5 nm to 20 nm. The local height at the edge is 18 nm.

The surface height shows similar profile for 10 keV. The local height reduces from  $\sim 21.5 \text{ nm}$  to 14.5 nm for the lateral positions  $x = -750 \mu\text{m}$  to  $x = -300 \mu\text{m}$ . There is a narrow hump

with local height of 22 nm at  $x = +300 \mu\text{m}$ . The other edge has local height of 16 nm which is lower than that for 9 keV.

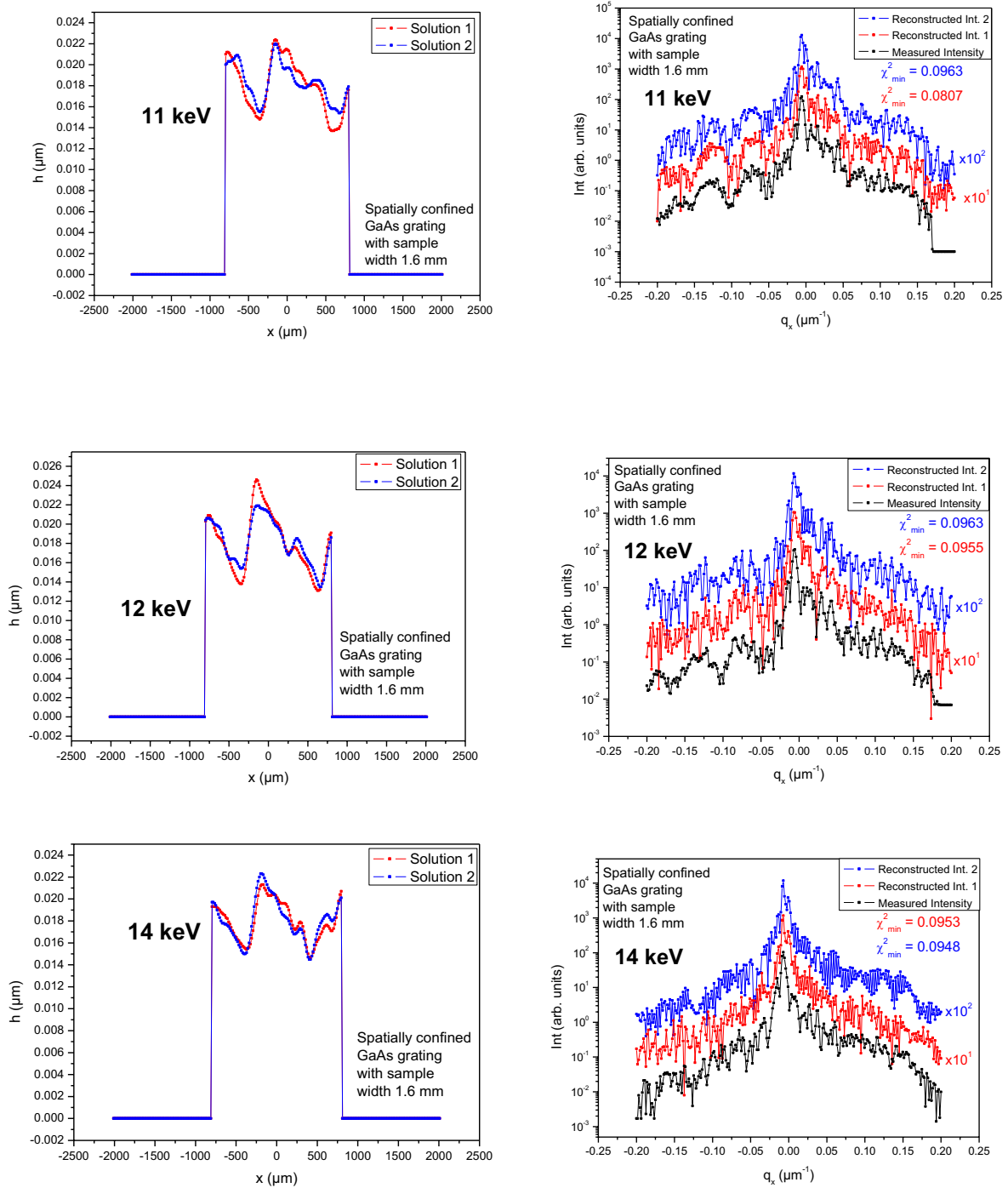


Fig. 6.37 Reconstructed surface height solutions and reconstructed intensity profiles along with measured intensity  $q_x$  scan for the reciprocal space map for spatially confined GaAs grating with sample width 1.6 mm at  $E = 11, 12$  and  $14 \text{ keV}$ . The surface height and scattered intensity are reconstructed using the modified ER algorithm. The reconstructed intensities (red and blue) are plotted with certain vertical offset along intensity axis. The respective value of  $\chi^2_{\min}$  for each fit of the reconstructed intensity to the measured one is mentioned alongside.

The feature with decreasing local surface height at the edge can also be seen for the reconstructed height solutions (Fig. 6.37 left) for 11 keV, 12 keV and 14 keV. The average height decreasing from 21 nm to 15 nm for 11 keV, from 20.5 nm to 14 nm for 12 keV and from 19 nm to 15 nm for 14 keV between lateral positions  $x = -780 \mu\text{m}$  to  $x = -340 \mu\text{m}$ .

The reconstructed surface profile for 11 keV shows smaller widths of around  $80 \mu\text{m}$  with decreasing height from 22 nm to 15 nm till the lateral position  $x = +670 \mu\text{m}$ . The local height for the other edge at  $x = +800 \mu\text{m}$  is 18 nm.

For the reconstructed surface profile for 12 keV two larger steps one with average height decreasing from 22 nm at  $x = -130 \mu\text{m}$  to 17 nm at  $x = +230 \mu\text{m}$  and second with average height decreasing from 18 nm at  $x = +350 \mu\text{m}$  to 16.5 nm at  $x = +670 \mu\text{m}$ . The local height for the other edge at  $x = +800 \mu\text{m}$  is 18.5 nm.

A large step with average height decreasing from 22 nm at  $x = -180 \mu\text{m}$  to 16.8 nm at  $x = +230 \mu\text{m}$  can be seen in the reconstructed surface profile for 14 keV. It contains two humps with average height 17.3 nm at  $x = +290 \mu\text{m}$  and 18.5 nm at  $x = +620 \mu\text{m}$ . The local height for the other edge at  $x = +800 \mu\text{m}$  is 20 nm.

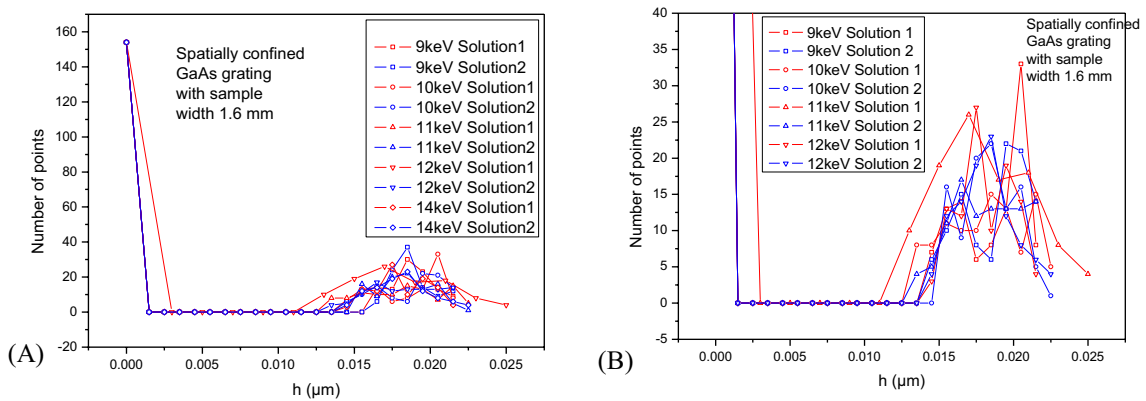


Fig. 6.38 Distribution of surface height for two different reconstructed solutions at  $E = 9, 10, 11, 12$  and  $14 \text{ keV}$  (A) The large vertical scale (B) Selected vertical scale

Fig. 6.38 shows the distributions of local height for the reconstructed surface height solutions at different selected energies. The first peak at zero corresponds to the zero density region outside finite sample size of 1.6 mm. The distributions do not show any common peak. As seen in Fig. 6.35, Fig. 6.36 and Fig. 6.37 left, the local height for the reconstructed surface



profiles at different energies does not vary with any mean value of the local height. But the surface profiles possess steps with different widths with decreasing local heights.

The critical energy for total external reflection for GaAs at  $\alpha_i = 0.16^\circ$  is  $E_c = 16.60 \text{ keV}$ . All the selected energies ( $E = 9, 10, 11, 12 \text{ and } 14 \text{ keV}$ ) lie below  $E_c = 16.60 \text{ keV}$ . The x-rays undergo total external reflection for all these selected energies. But the measured scattering patterns at different selected energies are not so similar as seen in Fig. 6.34 and Fig. 6.35, Fig. 6.36 and Fig. 6.37 (right) (black curves). Also for lower energies ( $E = 9, 10, 11 \text{ and } 12 \text{ keV}$ ) the data for some region for  $q_x > 0$  is not accessible as it is forbidden. This is the main reason that the solutions for reconstructed surface profiles at different energies resemble less similarity. Although the broad features like the step with decreasing local height between  $x = -780 \mu\text{m}$  and  $-340 \mu\text{m}$ .

## 6.2 References

- [6.1] C. Teichert, J. F. MacKay, D. E. Savage, M. G. Lagally, M. Brohl and P. Wagner, *Comparison of surface roughness of polished silicon wafers measured by light scattering topography, soft-x-ray scattering and atomic-force microscopy*, Appl. Phys. Lett. 66, 2346 (1995).

## Chapter 7

### Summary and outlook

#### 7.1 Summary

Surface profile information of various semiconducting samples at different experimental conditions (like different angle of incidence) is successfully reconstructed. The surface profile information reconstructed by this method is on technologically relevant length scales [7.1]. While preparing large semiconducting wafers it is important to have a quick tool to investigate the quality of surface over large lateral area of the wafer. The method discussed in this work can be easily applied without destructing the sample.

The method can give average spatially resolved surface profile information (Sections 6.1.1, 6.1.2, 6.1.3 and 6.1.6) when sample width is larger than the footprint of the incoming beam at the sample position. From the coherent reflectivity data for energies below the critical energy for total external reflection at a particular angle of incidence, the distribution of the reconstructed surface profiles at different selected energies is almost similar. This is evident because for the energies below the critical energy for total external reflection at a particular angle of incidence, the scattering originates only from the surface of the sample. There is no contribution from the subsurface electron density variations.

From the coherent reflectivity data for energies below the critical energy for total external reflection at a particular angle of incidence measured for a spatially confined sample (Section 6.1.4), 2 dimensional picture of the sample is reconstructed (Fig. 6.22 (A)). The reconstructions from the coherent reflectivity data at different energies give information about the profile from various depths inside the sample. This is the unique information accessed by the technique discussed in this work which is possible only with the help of “white” x-ray beam. The reconstructed profiles become smooth for the data recorded at higher energies (11 keV and 12 keV). This is because at a particular angle of incidence x-ray with higher energies can reach deeper inside the sample (Fig. 6.22 (B)) and the scattering corresponds more to the bulk of the sample and surface profile variations have less influence.

Some peculiarities of the reconstruction procedure of surface profile from the coherent reflectivity data of white x-ray beam are discussed further.

The 1D quadratic propagator term for the scattering geometry in reflection is derived (equation (5.66)) and incorporated in the phase retrieval algorithm in near field to reconstruct surface profile. The modified algorithm can reconstruct the model surface successfully (Fig. 5.19).

The application of the modified algorithm for the reconstruction of surface profile from the real measurement data faces some limitations. The main limitation is that the measured data is one dimensional. Phase retrieval algorithms have inherent limitation in reconstruction from one dimensional scattering data [7.2, 7.3]. The inclusion of propagator term and the phase of illumination function are found to improve the convergence of the algorithm (Fig. 5.19) for the model surface. The measured scattering from various surfaces is relatively weak than the calculated scattering from a model surface and thus clearly poses problems in convergence of the algorithm.

The convergence is improved if the sample is spatially confined (Section 5.6 (IV) and (VII)). The real space constraint of finite support region can be implemented which helps in finding converging solution (Fig. 6.19- Fig. 6.21 and Fig. 6.35- Fig. 6.37) for the algorithm.

In case of the coherent reflectivity measurement from a surface grating, the grating structure peaks are not distinctly visible (Fig. 4.8, Fig. 4.15). Due to the lack of the grating peaks, the grating structure is not observed in the reconstructed surface profiles (Sections 6.1.2, 6.1.3 and 6.1.7).

The spatial resolution of the reconstructed surface profile is limited by the maximum  $q_x$  – range in the measured scattering intensity. With the maximum  $q_x$  – range achieved of  $\pm 0.2 \mu m^{-1}$ , the spatial resolution achieved is only about  $16 \mu m$ . Hence the reconstructed surface profile can give the information only about the long range ordering over the sample surface. The maximum  $q_x$  – range can be increased if the measurement is performed for larger angles of incidence.

The distributions of local height for the reconstructed surface height solutions have similar behavior for most of the solutions (Fig. 6.5, Fig. 6.11, Fig. 6.17 and 6.33). These distributions for many solutions for the same measurement exhibit peak at almost the same position. This implies that the modified phase retrieval algorithm for reconstruction of surface profile is can successfully reconstruct the surface height profile with common mean surface height over a large lateral distance on the sample surface. It is rather difficult to reconstruct spatially resolved absolute local height due to some inherent limitations for reconstruction with 1D measured data.

## 7.2 Outlook

The lateral spatial resolution achieved (equation 6.1) in the reconstructed surface profile depends on the maximum lateral momentum transfer ( $q_{x,max}$ ) reached for the recorded scattered intensity. With the present experimental conditions at EDR bending magnet beamline at BESSY II, the scattered intensity is very weak for  $q_x > \pm 0.3 \mu m^{-1}$  even for a thin film with strongly scattering element like Pt ( $Z=78$ ) (Section 4.4). Also the peaks due to the grating periods cannot be clearly measured with due to weak scattering signal. To give an estimate, the scattering measured at incident angle  $\alpha_i = 0.5^\circ$  with exit angle scanned by amount  $\Delta\alpha_f = 0.3^\circ$  above and below the specular beam for 10 keV of x-rays can yield spatial resolution of  $\sim 1 \mu m$ . The EDR bending magnet beamline cannot provide sufficient incoming flux for these experimental parameters for the scattering from commonly used semiconducting materials like Si or GaAs. The exact quantity of the incoming flux required to get the scattering signal with sufficient statistics depends on various parameters like size of the aperture (pinhole) of the incoming beam, incident angle, exit angle, aperture to sample distance, sample to detector distance and the material of the sample.

Similar experiments can be performed at synchrotron source with higher incoming flux like 7 T Wiggler at BESSY II or at ESRF at higher angle of incidence and the maximum value of lateral momentum transfer reached would be higher. Hence spatially resolved information of the sample with better spatial resolution can be reconstructed using the phase retrieval algorithm discussed in this work.

The real measurements at EDR beamline are performed with white x-rays with useful energy range of 5-25 keV. The reciprocal space map (for example Fig. 4.4 (A)) contains irregularly spaced maximum lines in specific  $q_z$  – range. In this  $q_z$  – range the features in the scattering amplitude are almost similar at different values of  $q_z$  which are accessed at different x-ray energies. This abundant information about the scattering amplitude originating from the same illuminate area on the sample is useful, in principle, for getting a unique reconstruction of the surface profile. The real potential of the scattering of the “white” x-ray beam will be reached if the phase information at a particular energy can be given as a feedback for the reconstruction at the next energy. This additional phase information is expected to guide the algorithm to a unique solution of the surface morphology.

The quality of reconstruction depends of different parameters. The main parameter which affects the reconstruction is the correct knowledge of the illumination function at the sample position. This in turn depends on the correct measurement of experimental parameters like incident angle  $\alpha_i$ , pinhole diameter, pinhole to sample distance, sample to detector distance and the exit angle  $\alpha_f$ . It is important to study the correct measurement of these parameters and the influence of them on the final reconstruction of the surface profile.

### 7.3 References

- [7.1] Evaluating Surface Roughness of Si Following Selected Lapping and Polishing Processes, 86<sup>th</sup> Applications Laboratory Report, South Bay Technologies, Inc. (2007).
- [7.2] H.A. Ferwerda, *Inverse Source Problems in Optics*, edited by H.P. Baltes, Topics in Current Physics Vol. 9, Springer-Verlag, Berlin (1978)
- [7.3] Y.M. Bruck and L.G. Sodin, *On the ambiguity of image reconstruction problem*, Optics Commun. 30, 304 (1979)



## Appendix A

The length of position vector  $r$  (Fig. 5.15) from  $P_0$  to  $P_1$  is given by,

$$r = [X_1^2 + Y_1^2 + Z_1^2 + 2X_1(x - X) + 2Y_1(y - Y) + 2Z_1(z - Z) + (x - X)^2 + (y - Y)^2 + (z - Z)^2]^{1/2} \quad (\text{A.1})$$

$$r = L_2 \left[ 1 + 2 \frac{X_1}{L_2} \frac{(x - X)}{L_2} + 2 \frac{Y_1}{L_2} \frac{(y - Y)}{L_2} + 2 \frac{Z_1}{L_2} \frac{(z - Z)}{L_2} + \frac{(x - X)^2}{L_2^2} + \frac{(y - Y)^2}{L_2^2} + \frac{(z - Z)^2}{L_2^2} \right]^{1/2} \quad (\text{A.2})$$

where the length of the vector from  $O_0$  to  $O_1$ ,  $L_2 = \sqrt{X_1^2 + Y_1^2 + Z_1^2}$ .

In terms of direction cosines  $l = \frac{X_1}{L_2}$ ,  $m = \frac{Y_1}{L_2}$ ,  $n = \frac{Z_1}{L_2}$  and with the transformed coordinates

$$\bar{x} = \frac{x}{L_2}, \bar{y} = \frac{y}{L_2}, \bar{z} = \frac{z}{L_2} \text{ and } \bar{X} = \frac{X}{L_2}, \bar{Y} = \frac{Y}{L_2}, \bar{Z} = \frac{Z}{L_2} \quad (\text{A.3})$$

the equation (A.2) can be written as

$$r = L_2 [1 + 2l(\bar{x} - \bar{X}) + 2m(\bar{y} - \bar{Y}) + 2n(\bar{z} - \bar{Z}) + (\bar{x} - \bar{X})^2 + (\bar{y} - \bar{Y})^2 + (\bar{z} - \bar{Z})^2]^{1/2} \quad (\text{A.4})$$

By Taylor expanding the square root term,

$$r \cong L_2 \left[ 1 + l(\bar{x} - \bar{X}) + m(\bar{y} - \bar{Y}) + n(\bar{z} - \bar{Z}) + \frac{1}{2} \{ (\bar{x} - \bar{X})^2 + (\bar{y} - \bar{Y})^2 + (\bar{z} - \bar{Z})^2 - [l(\bar{x} - \bar{X}) + m(\bar{y} - \bar{Y}) + n(\bar{z} - \bar{Z})]^2 \} \right]^{1/2} \quad (\text{A.5})$$

By expanding the terms in the expression further and substituting in equation (5.39), the diffracted amplitude can be written as

$$\begin{aligned}
 A(x, y) = C \iint \rho(X, Y) \exp \left\{ -ikL_2 \left( \frac{1-l^2}{2} \bar{X}^2 + \frac{1-m^2}{2} \bar{Y}^2 \right. \right. \\
 \left. \left. - n\bar{X}\bar{Y} \right) \right\} \exp \left\{ -ikL_2 \left[ \bar{X}(l + (1-l^2)\bar{x} - l\bar{m}\bar{y} + l\bar{m}\bar{Z} - n\bar{l}\bar{z}) \right. \right. \\
 \left. \left. + \bar{Y}(n + (1-n^2)\bar{z} - n\bar{l}\bar{x} - m\bar{n}\bar{y} - m\bar{n}\bar{z} + m\bar{n}\bar{Z}) \right] \right\} dX dY \quad (A.6)
 \end{aligned}$$

where  $C$  is a constant given by

$$\begin{aligned}
 C = \frac{iZ_1}{\lambda L_2} \exp \left\{ -ikL_2 \left[ 1 + l\bar{x} + m\bar{y} + n\bar{z} - m\bar{Z} + \frac{1-l^2}{2} \bar{x}^2 + \frac{1-m^2}{2} \bar{y}^2 \right. \right. \\
 \left. \left. + \frac{1-n^2}{2} \bar{z}^2 - (1-m^2)y\bar{z} - lm\bar{x}\bar{y} + lm\bar{x}\bar{Z} + n\bar{l}\bar{x}\bar{z} - m\bar{n}\bar{y}\bar{z} \right. \right. \\
 \left. \left. + m\bar{n}\bar{z}\bar{Z} \right] \right\} \quad (A.7)
 \end{aligned}$$

Writing the equation (A.6) in terms of  $x, y, z$  and  $X, Y, Z$

$$\begin{aligned}
 A(x, y) = C \iint \rho(X, Y) \exp \left\{ -\frac{ik}{L_2} \left( \frac{1-l^2}{2} X^2 + \frac{1-m^2}{2} Y^2 \right. \right. \\
 \left. \left. - n\bar{l}XY \right) \right\} \exp \left\{ -\frac{ik}{L_2} \left[ X(lL_2 + (1-l^2)x - lmy + lmZ - nlz) \right. \right. \\
 \left. \left. + Y(nL_2 + (1-n^2)z - nlx - mny - mnz + mnZ) \right] \right\} dX dY \quad (A.8)
 \end{aligned}$$

With spatial frequencies defined as

$$f_X = \frac{1}{\lambda L_2} (lL_2 + (1-l^2)x - lmy + lmZ - nlz) \quad (A.9)$$

$$f_Y = \frac{1}{\lambda L_2} (nL_2 + (1-n^2)z - nlx - mny - mnz + mnZ) \quad (A.10)$$



The diffraction amplitude can be written as

$$A(x, y) = C \iint \rho(X, Y) \exp \left\{ -\frac{ik}{L_2} \left( \frac{1-l^2}{2} X^2 + \frac{1-m^2}{2} Y^2 - nlXY \right) \right\} \exp \{ -i(f_X X + f_Y Y) \} dXdY \quad (\text{A.11})$$

This can be recognized as a Fourier transform of product of density function  $\rho(X, Y)$  and a quadratic phase term as follows

$$A(x, y) = C \times \mathcal{F} \left( \rho(X, Y) \exp \left\{ -\frac{ik}{L_2} \left( \frac{1-l^2}{2} X^2 + \frac{1-m^2}{2} Y^2 - nlXY \right) \right\} \right) \quad (\text{A.12})$$



## Acknowledgements

I would like to thank all the people who helped and supported me throughout the entire process of my doctoral work.

Firstly I would like to express my gratitude to Prof. Dr. Ullrich Pietsch under whose direction I have been fortunate to pursue the research described in this thesis. His deep understanding of x-ray diffraction physics and his expertise with synchrotron x-ray experiments have benefitted me. I am thankful to him for his constant support and continuous guidance throughout the course of this work.

I would like to acknowledge Dr. Tobias Panzner for the detailed discussions on the problem and his support throughout my doctoral work. I am thankful to him also for his useful suggestions during the writing of this thesis.

For the technical support at the EDR beamline at BESSY II I would like to thank Dr. W. Leitenberger.

I am thankful to Dr. U. Zeimer of FBH, Berlin for providing semiconducting samples.

I would like to thank Dr. C. Gutt for providing the code of the basic phase retrieval program for image reconstruction.

I am also thankful to Prof. Dr. M. Tolan for spending time in valuable discussions from his busy schedule.

I would like to thank all the former and present members of Solid State Physics at University of Siegen for providing a friendly environment in the group.

I acknowledge BESSY II for providing the synchrotron facility at the EDR beamline.

For financial support I am thankful to Bundesministerium für Bildung und Forschung (BMBF).

For providing useful infrastructure I am thankful to University of Siegen.

Finally I would like to thank my parents and my wife, Anagha for their support and encouragement throughout my doctoral work.



## **Eidesstattliche erklärung**

Ich versichere hiermit an Eides statt, dass ich die vorliegende Arbeit ohne fremde Hilfe und ohne Benutzung anderer als der angegebenen Hilfsmittel angefertigt habe. Alle Ausführungen, die wörtlich oder sinngemäß aus fremden Quellen übernommen wurden sind als solche gekennzeichnet. Die Arbeit wurde bisher in gleicher oder ähnlicher Form noch keiner anderen Jury vorgelegt und wird noch nicht kommerziell genutzt.

Ich bin bewusst dass eine falsche Erklärung den Ausschluss aus dem Wettbewerb zur Folge haben wird.

Siegen, 27.04.2009

Ort, Datum

Unterschrift